MODELING AND ANALYSIS OF A PEM FUEL CELL SYSTEM

FOR A QUADRUPED ROBOT

Except where reference is made to the work of others, the work described in this thesis is my own or was done in collaboration with my advisory committee. This thesis does not include proprietary or classified information.

_____

Heon Joong Lee

Certificate of Approval:

| | |
|---|---|
| _____ | _____ |
| Jay Khodadadi<br>Professor<br>Mechanical Engineering | Song-Yul Choe, Chair<br>Associate Professor<br>Mechanical Engineering |
| _____ | _____ |
| Sushil Bhavnani<br>Professor<br>Mechanical Engineering | George Flowers<br>Dean of the Graduate School<br>Graduate School |

# MODELING AND ANALYSIS OF A PEM FUEL CELL SYSTEM FOR A QUADRUPED ROBOT

Heon Joong Lee

A Thesis

Submitted to

the Graduate Faculty of

Auburn University

in Partial Fulfillment of the

Requirements for the

Degree of

Master of Science

Auburn, Alabama

August 10, 2009

MODELING AND ANALYSIS OF A PEM FUEL CELL SYSTEM

FOR A QUADRUPED ROBOT

Heon Joong Lee

Permission is granted to Auburn University to make copies of this thesis at its discretion, upon the request of individuals or institutions and at their expense.
The author reserves all publication rights.

_____

Signature of Author

_____

Date of Graduation

# VITA

Heon Joong Lee, son of Dae Kyu Lee and Kyung Ae You, was born on Jan 10th, 1981 in Seoul, Korea. He earned a Bachelor of Science degree in the Department of Mechanical Engineering at Sogang University in Feb, 2007. He has studied at Auburn University pursuing a Master of Science degree in the Department of Mechanical Engineering since May 2007.

THESIS ABSTRACT

MODELING AND ANALYSIS OF A PEM FUEL CELL SYSTEM

FOR A QUADRUPED ROBOT

Heon Joong Lee

Master of Science, August 10, 2009
(B.S., Sogang University, 2007)

135 Typed Pages

Directed by Song-Yul Choe

The polymer electrolyte membrane fuel cell is a prospective alternative energy conversion device that has environment-friendly characteristics. It has not only electrochemical reaction but also coupled thermal fluid characteristics. Chemical reaction of the reactants, mass transport of products, heat generation and heat transfer from catalyst layer to the end plate occur during operation of the fuel cell. In particular, water management and heat management play an important role in safe and successful operation of the Polymer Electrolyte Membrane (PEM) fuel cell system. Therefore, the understanding of the dynamic characteristics of the PEM fuel cell stack is crucial to ensure accurate analysis and effective design of the PEM fuel cell system.

Generally, computational methodology is an essential tool for investigating interrelated physical parameters and dynamic behavior. The dynamic model for the PEM

fuel cell system was developed considering temperature and two-phase effects in the Advanced Propulsion Research Laboratory at Auburn University. The model developed and compared with experimental results. Moreover, the two cell stack model is used to analyze static and dynamic behaviors under different operating conditions that include operating temperature, relative humidity of air, stoichiometric ratio, partial pressure of reactants in addition to various geometric parameters that include thickness and porosity of the gas diffusion layer (GDL) and the thickness of the membrane under the ramp and step current loads.

The analysis of the 20-cell stack is also performed to investigate the temperature effect between cells within the stack before a multi cell stack is constructed. The analysis consists of static and dynamic behavior for understanding temperature distribution and voltage difference due to the temperature effect. Finally, the 100-cell stack is constructed and its characteristics are analyzed. However, stack model alone has a limitation for estimating real net power from the fuel cell system without consideration of auxiliary components such as an air processing system and a thermal circuit. Therefore, each component is modeled for the 100-cell PEM fuel cell system.

Various comparative studies showed that proper operating conditions are critical for improved performance and two phase effects which both affect concentration of reactants, thus should be considered for the design and optimization of the stack. Moreover, appropriate design and sizing of the air supply system and thermal circuit components could reduce parasitic power and increased efficiency of the fuel cell system. In the multi cell stack model, the temperature distribution affected not only concentration

of the reactant but also proton conductivity of the membrane. Consequently, it caused the change in concentration overpotential, ohmic overpotential and cell voltage.

ACKNOWLEDGEMENTS

I would like to express special gratitude to the advisor and chair of the committee, Professor Song-Yul Choe, for his guidance during my time here at Auburn University.

I would also like to thank the other committee members, Professor Jay Khodadadi and Professor Sushil Bhavnani for their valuable advice. Special thanks are extended to all of my colleagues, Jinglin He, Kevin Siniard, Alan Dunlavy, Xiao Meng, Ruijian Fu and Jong-Woo Ahn on the Advanced Propulsion Laboratorty of Auburn University for constructive discussions during research work.

Lastly, I would like to thank my parents and wife, Dae-Kyu Lee, Kyung-Ae Ryu and Sunja Kim. Without their strong motivation and support, I would not be where I am today.

Computer software used: Microsoft word 2007

Matlab/Simulink 7.0.4

Origin 7.5

TABLE OF CONTENTS

LIST OF FIGURES ..... xiii

LIST OF TABLES ..... xvii

NOMENCLATURE ..... xviii

1 INTRODUCTION ..... 1

1.1 THE FUEL CELL ..... 1

1.2 PRINCIPLES OF A FUEL CELL OPERATION ..... 3

1.3 TYPES OF A FUEL CELL ..... 5

1.4 ADVANTAGES OF THE PEM FUEL CELL ..... 6

1.5 BALANCE OF PLANT ..... 8

1.6 APPLICATION TO A QUADRUPED ROBOT ..... 9

2 BACKGROUND ..... 10

3 PEM FUEL CELL STACK ..... 12

3.1 PRINCIPLES ..... 14

3.2 GOVERNING EQUATIONS ..... 15

3.2.1 I-V CHARACTERISTIC ..... 15

3.2.2 ENERGY BALANCE ..... 17

3.2.3 WATER BALANCE ..... 17

3.2.4 GDL WITH 2 PHASE EFFECT ..... 20

3.3 MODEL DIAGRAM ..... 23

4 BALANCE OF PLANT ..... 24

4.1 AIR PROCESSING SYSTEM ..... 25
4.1.1 SYSTEM CONFIGURATION AND COMPONENTS ..... 25
4.1.2 BLOWER ..... 25
4.2 THERMAL CIRCUIT ..... 29
4.2.1 COOLANT PUMP ..... 32
4.2.2 RADIATOR ..... 33
4.2.3 WATER RESERVOIR ..... 35
5 ANALYSIS OF A TWO-CELL STACK ..... 36
6 STACK DESIGN ..... 57
6.1 QUADRUPED ROBOT SPECIFICATION ..... 57
6.2 STACK SIZING ..... 58
6.3 20-CELL STACK ANALYSIS FOR CELL EXTENSION ..... 62
6.3.1 STACK BEHAVIOR ..... 63
6.3.2 DYNAMIC BEHAVIOR ..... 66
6.4 100-CELL STACK ..... 71
6.4.1 MODEL DESCRIPTION ..... 71
6.5 DESIGN OF THE AIR PROCESSING SYSTEM ..... 74
6.5.1 SPECIFICATION OF THE AIR PROCESSING SYSTEM ..... 74
6.5.2 DESIGN OF THE BLOWER ..... 76
6.5.3 PARAMETRIC STUDY ..... 81
6.6 DESIGN OF HEAT EXCHANGER ..... 83
7 100-CELL PEM FUEL CELL SYSTEM ..... 90
7.1.1 STATIC BEHAVIOR ..... 91

7.1.2 DYNAMIC BEHAVIOR ..... 93
7.1.3 DYNAMIC BEHAVIOR DURING OPERATION MODE ..... 105
7.1.4 DESIGN PROGRESS ..... 108
8 CONCLUSIONS ..... 110
REFERENCES ..... 113

# LIST OF FIGURES

Figure 1 Average energy efficiencies of the principal energy conversion systems [1]. ..... 2

Figure 2 Schematic representation of a PEM fuel cell ..... 4

Figure 3 A schematic diagram of a PEM fuel cell system [3] ..... 8

Figure 4 Quadruped robot ..... 9

Figure 5 A schematic diagram of a PEM fuel cell stack ..... 13

Figure 6 Mocroscale GDL model ..... 21

Figure 7 Fuel cell stack model schematic block diagram ..... 23

Figures 8 A schematic diagram of balance-of-plant for PEM fuel cell system [3] ..... 24

Figure 9 A schematic diagram of air processing system ..... 25

Figure 10 A block diagram of blower model ..... 26

Figure 11 Estimation of blower characteristics and simulation of blower model ..... 29

Figure 12 A schematic diagram of thermal circuit ..... 30

Figure 13 Thermal circuit block diagram ..... 32

Figure 14 Comparison of the simulated and experimental two-cell stack and individual cell voltages ..... 37

Figure 15 I-V curve and temperature of a two cell stack under the ramp input of current density. ..... 40

Figure 16 I-V characteristic, power and overpotential for different operating temperature ..... 43

Figure 17 I-V characteristic, power and overpotential for different stoichiometric ratio. 45

Figure 18 I-V characteristic, power and overpotential for different relative humidity .... 47
Figure 19 I-V characteristic, power and overpotential for different reactant gas pressure49
Figure 20 I-V characteristic for 9 different cell operating conditions ..... 50
Figure 21 Cell power for 9 different cell operating conditions..... 50
Figure 22 Response of a fuel cell to a multi-step current density at different cathode GDL thicknesses. (a) Cell voltage, (b) Activation and ohmic overpotential and (c) Membrane water content and oxygen concentration near the cathode catalyst layer. ..... 52
Figure 23 Dynamic responses of the fuel cells to step changes in current density at different cathode GDL porosities. (a) Cell voltage, (b) Activation and ohmic overpotential and (c) Membrane water content and oxygen concentration near by the cathode catalyst layer. ..... 53
Figure 24 Dynamic responses of the fuel cells during a step change in current density at different membrane thicknesses. (a) Cell voltage, (b) Activation and ohmic overpotential and (c) Membrane water content and oxygen concentration near the cathode catalyst layer. ..... 55
Figure 25 I-V characteristic for 4 different geometry parameters ..... 56
Figure 26 Cell power for 4 different geometry parameters ..... 56
Figure 27 Stack size and operating voltage ..... 61
Figure 28 Cell efficiency dependent upon nominal cell potential ..... 61
Figure 29 Single cell power, efficiency and current density with selected cell voltage ... 62
Figure 30 I-V polarization curve of the 20 cell stack ..... 63
Figure 31 Voltage distribution under the constant current density, 0.6 (A $cm^{-2}$) at 2sec . 64
Figure 32 Temperature distribution under the constant current density 0.6 (A $cm^{-2}$) ..... 65

Figure 33 Temperature changes during operation with constant current density ..... 66
Figure 34 Temperature changes during the start-up ..... 67
Figure 35 Temperature distribution during the start-up ..... 69
Figure 36 Voltage changes during the start-up ..... 70
Figure 37 Temperature difference ..... 71
Figure 38 A schematic diagram of the 100 cell stack ..... 72
Figure 39 100-cell stack block diagram ..... 73
Figure 40 A schematic diagram of blower ..... 77
Figure 41 Brake horse power for a different wheel diameter ..... 82
Figure 42 Head loss for a different wheel diameter ..... 82
Figure 43 Head loss for a same mass flow rate with different hub-tip ratio ..... 83
Figure 44 The relationship between coolant temperature difference, flow rate and radiator frontal area ..... 88
Figure 45 Schematic diagram of PEM fuel cell system ..... 90
Figure 46 I-V polarization characteristic curve of each cell ..... 92
Figure 47 Stack power and voltage ..... 92
Figure 48 Temperature changes during the start-up ..... 94
Figure 49 Comparison of temperature distribution during the start-up ..... 95
Figure 50 Temperature distribution during the start-up ..... 96
Figure 51 Voltage changes during the start-up ..... 97
Figure 52 Current density applied ..... 98
Figure 53 Transient responses of temperature in the middle cells ..... 99
Figure 54 Dynamic response of oxygen concentration to the step input ..... 100

Figure 55 Dynamic response of vapor concentration to the step input..... 101
Figure 56 Transient response of liquid water saturation and water content of membranes in the middle cells ..... 102
Figure 57 Transient responses of activation and ohmic overpotential in the middle cells ..... 104
Figure 58 Transient responses of PEM fuel cell stack voltage ..... 104
Figure 59 Current load under the operation mode ..... 105
Figure 60 Net power and stack power during the operation mode ..... 106
Figure 61 Parasitic power of air supply system and thermal circuit during operation ... 107
Figure 62 Temperature changes during the operation ..... 108
Figure 63 Schematic diagram and design progress of the PEM fuel cell system ..... 109

# LIST OF TABLES

Table 1 Classification of the fuel cell ..... 6

Table 2 Three-level orthogonal arrays for 9 different cell operating conditions ..... 49

Table 3 Two-level orthogonal arrays for 4 different geometry parameters ..... 56

Table 4 Operating mode of the quadruped robot ..... 58

Table 5 Geometric parameters and materials for the design ..... 72

Table 6 Design parameter for the blower ..... 81

Table 7 Operating condition for the heat exchanger ..... 83

Table 8 Parameters for heat exchanger ..... 84

Table 9 Design progress of the PEM fuel cell system ..... 109

# NOMENCLATURE

| | |
|---|---|
| $a$ | Water activity |
| $A$ | Area ($m^2$) |
| $A_c$ | Cross area ($m^2$) |
| $b$ | Parametric coefficient (V) |
| $c$ | Concentration of species (mol $cm^{-3}$) or safety factor |
| $C$ | Mass concentration (kg $m^{-3}$) |
| $CFM$ | Cubic feet per minute ($ft^3$ $min^{-1}$) |
| $Cp$ | Specific heat capacity (J $kg^{-1}$ $K^{-1}$) |
| $d$ | Diameter (m) |
| $D$ | Diameter (m) |
| $D_h$ | Hydraulic diameter (m) |
| $D_m$ | Diffusion coefficient ($m^2$ $s^{-1}$) |
| $<D_m>$ | Effective diffusivity ($m^2$ $s^{-1}$) |
| $E$ | Open circuit voltage (V) |
| $E_{electric}$ | Electrical energy (J) |
| $g$ | Gravitational acceleration (m $s^{-2}$) |
| $G$ | Mass flux (kg $m^{-2}$ $s^{-1}$) |
| $h$ | Convective heat transfer coefficient (W $m^{-2}$ $K^{-1}$) |
| $i$ | Current density (A $m^{-2}$) |
| $I$ | Current (A) |
| $j_h$ | Colburn factor |
| $J$ | Rotational inertia (kg $m^2$) |
| $k$ | Conductive heat transfer coefficient (W $m^{-1}$ $K^{-1}$) |
| $K$ | Gas permeability ($m^2$) |
| $L$ | Length (m) |
| $L_a$ | Air brake power (W) |
| $L_s$ | Shaft horse power |
| $m$ | Mass (kg) |
| $M$ | Molecular mass (kg $mol^{-1}$) |
| $n$ | Number of electrons (2 or 4) |
| $n_d$ | Electro-osmotic drag coefficient |
| $N$ | Speed (rpm) or molar flux (mol $s^{-1}$ $m^{-3}$) or number of pipe |
| $N_s$ | Specific speed (rpm) |
| $N_u$ | Nusselt number |
| $p$ | Pressure (atm) |
| $P$ | Power (W) |
| $Q$ | Heat (J) |
| $\dot{Q}$ | Heat transfer rate (W) |
| $R$ | Universal gas constant (J $mol^{-1}$ $K^{-1}$) |

| | |
|---|---|
| $Re$ | Reynolds number |
| $R_{ele}$ | Electrical resistance (Ω) |
| $R_{evap}$ | Evaporation rate (mol $m^{-3}$ $s^{-1}$) |
| $s$ | Liquid water saturation ratio |
| $\Delta S$ | Change in entropy (J $mol^{-1}K^{-1}$) |
| $t$ | Thickness (cm or m) or time (sec) |
| $T$ | Temperature (K) |
| $U$ | Overall heat transfer coefficient(W $m^{-2}$ $K^{-1}$) |
| $v$ | Velocity (m $s^{-1}$) |
| $V$ | Volume ($m^3$) or Voltage (V) |
| $W$ | Work (J) |
| $x$ | Molar ratio |
| $z$ | Number of blades |

*Subscript*

| | |
|---|---|
| *act* | Activation |
| *amb* | Ambient air |
| *an* | Anode |
| *bl* | Blower |
| *c* | Capillary |
| *ca* | Cathode |
| *conc* | Concentration |
| *cool* | Coolant |
| *d* | Dynamic |
| *diff* | Diffusion effect |
| *ele* | Electro osmotic effect |
| *i* | Cell number |
| *in* | Inlet |
| *j* | Layer |
| *k* | Reactant or product gases |
| *l* | Anode or cathode or liquid |
| *m* | Motor |
| *mass* | Mass concentration |
| *mem* | Membrane |
| *mid* | Middle point |
| *ohm* | Ohmic |
| *pl* | Pole |
| *rad* | Radiation |
| *rct* | Reactant |
| *res* | Reservoir |
| *rl* | Relative |
| *s* | Stator or static |
| *sat* | Saturation |
| *sou* | Source |
| *st* | Stack |
| *v* | Vapor |

*Greek symbols*

| | |
|---|---|
| $\varepsilon$ | Porosity |
| $\lambda$ | Water content |
| $\rho$ | Mass density (kg $m^{-3}$) |
| $\mu$ | Viscosity (kg $m^{-1}$ $s^{-1}$) |
| $\eta$ | Overpotential (V) or efficiency |
| $\xi$ | Constant parametric coefficient (V) |
| $\sigma$ | Stress (Pa) |
| $\sigma_{mem}$ | Membrane conductivity ($\Omega^{-1}$ $cm^{-1}$) |
| $\gamma$ | Specific mass of gas or volumetric condensation rate ($s^{-1}$) |
| $\theta$ | Contact angle ($^{o}$) |
| $\Phi$ | Flux linkage (V s $rad^{-1}$) |
| $\omega$ | Angular velocity (rad $s^{-1}$) |

# 1 INTRODUCTION

## 1.1 THE FUEL CELL

Currently, research about renewable alternative energy is energetically pursued to solve economical issues from highly priced gas to environmental issues like global warming. In other words, research about renewable alternative energy is not only for economic benefit, but also for the preservation of human beings' very existence. Conventional fossil fuels which meet 80% of the energy demands have two major disadvantages. The first problem is that the amount of fossil fuels is limited. Secondly, fossil fuels cause severe pollution which lead to global warming, weather changes, the Antarctic icecap melting, an increasing sea level, acid rain and destruction of soil and forests. Therefore, recently, many industries and governments have concentrated on researching and developing renewable alternative energy.

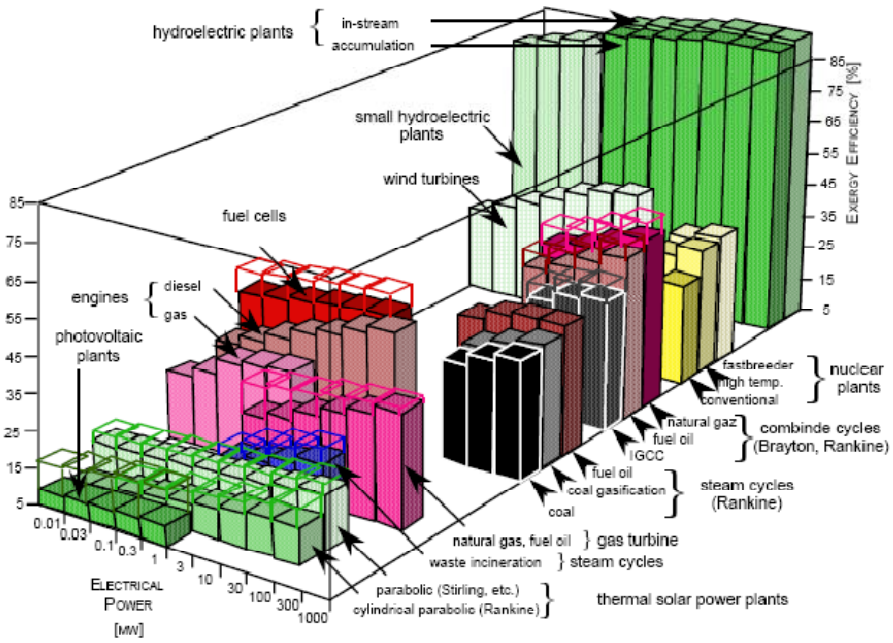


Figure 1 Average energy efficiencies of the principal energy conversion systems [1].

There are many technologies being developed to replace conventional energy sources. Specifically, hydrogen is one of the most promising energy fuels of the future. A hydrogen energy system was actually proposed in early 1970's. However, its research has been drastically increased over the last 10 years by many universities and research institutes. Hydrogen has a lot of advantages over other contenders. It is the most lightweight fuel as well as the most efficient and clean energy source [2].

A fuel cell is an electrochemical energy conversion device which converts the chemical energy of fuel such as hydrogen into electrical energy like DC electricity. One of the advantages of a fuel cell is that it can efficiently convert hydrogen into electricity by electrochemical processes. This conversion efficiency is much higher than other traditional energy conversion devices such as steam engines to turn generators. Several

steps were required to make electrical energy in the past. For example, heat, produced through burning fuel, is used for making a working fluid like water vapor. The vapor is used to rotate a turbine to make mechanical energy which is converted to electrical energy by use of an electric generator. However, a fuel cell is able to minimize this process of making electricity without the use of any mechanical device, and this is the reason why the efficiency of fuel cell is usually higher than that of traditional internal combustion engines. Moreover, it guarantees a fuel cell a longer life than other mechanical energy conversion devices in terms of mechanical endurance because it has no moving parts like pistons, shafts, or bearings.

Fuel cells also have big advantages in environmental issues. An impurity like sulfur causes performance and endurance of fuel cells to decrease largely. Therefore, impurities are clearly removed before it is delivered and used in a fuel. Consequently, it makes clean exhaust gas without any $SO_x$. Moreover, pure water from the chemical reaction between hydrogen and oxygen is a pivotal factor in making the fuel cell environmentally friendly. Thus, fuel cells are highly efficient, environmentally friendly energy conversion devices that can potentially replace conventional internal combustion engine.

## 1.2 PRINCIPLES OF A FUEL CELL OPERATION

A fuel cell has an oxidizing agent on the catalyst layer where a chemical reaction occurs with fuel and oxygen. Hydrogen is usually used as a fuel because its electrochemical reaction speed is the fastest among the fuel cell fuels. Oxygen is used as an oxidant, which abundantly exist in the air and can be used to supply oxygen. When

hydrogen is used as a fuel and oxygen is used as an oxidant, fuel cells are one of the cleanest energy conversion devices, only producing pure water and heat as the byproducts.

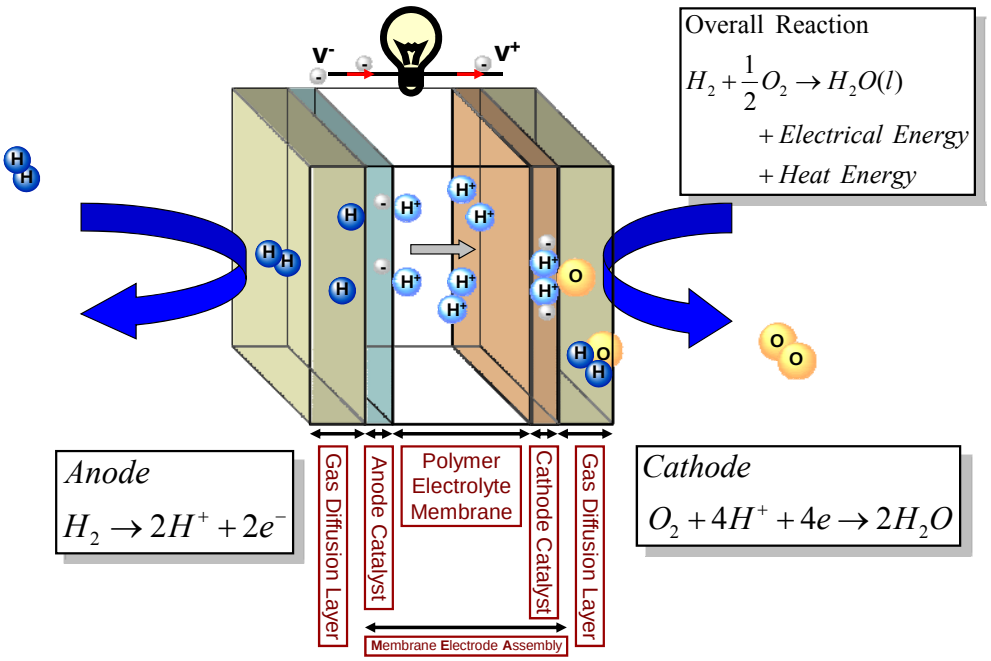


Figure 2 Schematic representation of a PEM fuel cell

A fuel cell causes an electrochemical reaction to occur between both faces of a permeable membrane which transmit no gas but only specific ion selectively. On one side, reaction occurs, which produces specific ions, but on the other side, a reaction occurs, which consumes specific ions.

For example, as shown in the figure above, electrons generating reaction occurs as the hydrogen being supplied is converted into hydrogen ions. The hydrogen ions

produced are transported through a membrane to the cathode catalysts in the fuel cell, while the electrons produced move to the opposite side through the outer transport circuit, reacting with oxygen supplied and then produces water. In sum, each oxidation reaction of hydrogen and reduction reaction of oxygen occurs on both sides of the membrane as water and electricity are produced.

Fuel cells use platinum as a catalyst that exists on both sides of the membrane and allows for electrochemical reactions. A catalyst layer that separates electrons from the oxidation reaction of the fuel is called the anode. The other catalyst layer which consumes electrons from the reduction reaction with the oxygen supplied is called the cathode. Therefore, about 50% of energy in fuel is converted into electricity, not by combustion, but by an electrochemical reaction between the fuel and air. The remainder is converted to heat.

## 1.3 TYPES OF A FUEL CELL

Fuel cells can be categorized by the operating temperature and fuel delivery methods, but can be more specifically classified by the type of electrolyte used. Polymer electrolyte membrane fuel cells (PEMFC) have some specific advantages over other fuel cells. They can reduce thermal loss by operating at lower temperatures, and their smaller size is more appropriate for automobiles and portable devices. This is the reason why most automotive companies research polymer electrolyte membrane fuel cells and why almost all the fuel cells used in automobiles are polymer electrolyte membrane fuel cells.

| Classification criterion | | | | |
|---|---|---|---|---|
| Operating temperature (°C) | | Electrolyte | Power density (kW $m^{-2}$) | Electrical efficiency of stack (%) |
| Low temperature | 60-100 | AFC (Alkaline fuel cell) | 0.7-8.1 | 45-60 |
| | 50-100 | PEMFC (Polymer electrolyte membrane fuel cell) | 3.8-6.5 | 40-55 |
| | 50-200 | DMFC (Direct methanol fuel cell) | - | 40 |
| | 160-210 | PAFC (Phosphoric acid fuel cell) | 0.8-1.9 | 40-50 |
| High temperature | 650-800 | MCFC (Molten carbonate fuel cell) | 0.1-1.5 | 50-60 (system) |
| | 800-1000 | SOFC (Solid oxide fuel cell) | 1.5-2.6 | 50-65 |

Table 1 Classification of the fuel cell

## 1.4 ADVANTAGES OF THE PEM FUEL CELL

As mentioned before, fuel cells have a higher efficiency than traditional internal combustion engines, so they are very suitable for automobile propulsion system. For instance, the electrical efficiency of polymer electrolyte membrane fuel cells is higher

than that of a comparably sized internal combustion engine (about 55% optimistically compared to 37.6% at full load [1]. Moreover, fuel cells which use hydrogen as a fuel exhaust harmless gases like air and water vapor. They are also very resistant to corrosion because the reaction product is not a liquid electrolyte, but only water.

Polymer electrolyte membrane fuel cells operates at a low temperature, that is, about 80°C, which make polymer electrolyte fuel cell systems stable and suitable for use in automobiles and portable devices because of a smaller possibility of accidents than conventional internal combustion engines. The low operating temperature allows polymer electrolyte membrane fuel cells to reduce start-up time much more than other types of fuel cells. These are the main advantages of the polymer electrolyte membrane fuel cell over traditional energy conversion devices. Furthermore, it can be modularized so that the amount of power generation is increased easily by attaching additional fuel cell stacks to meet demands. This feature enables us not only to gradually increase the size of energy conversion devices but also to minimize initial cost for energy conversion devices. Having no moving parts also allows a fuel cell to increase its life span. Currently, the life span of a fuel cell is about 4,000 hours which should be further increased to 40,000 for use in power plant stations. Its silent operation is another advantage for application in portable devices and military devices. However, polymer electrolyte membrane fuel cells should be hydrated properly with a supply of humidified air to maintain appropriate hydrogen ion conductivity. Despite some disadvantages, polymer electrolyte membrane fuel cells are the best potential energy conversion device for automobiles.

## 1.5 BALANCE OF PLANT

Auxiliary components such as the air supply system, fuel delivery system, and thermal system including a coolant pump, radiator, and fan are essential for the successful operation of a fuel cell system. The air supply system and fuel delivery system supply reactant gas, oxygen and hydrogen to the stack. A humidifier in the air supply system is another important part because a well hydrated membrane can transport positive ions with less ohmic loss. Therefore, the reactants of both the anode and cathode should be humidified appropriately. A thermal system manages heat produced from the cell stack and maintains the desired operating temperature which is pivotal for the performance and durability of a fuel cell.

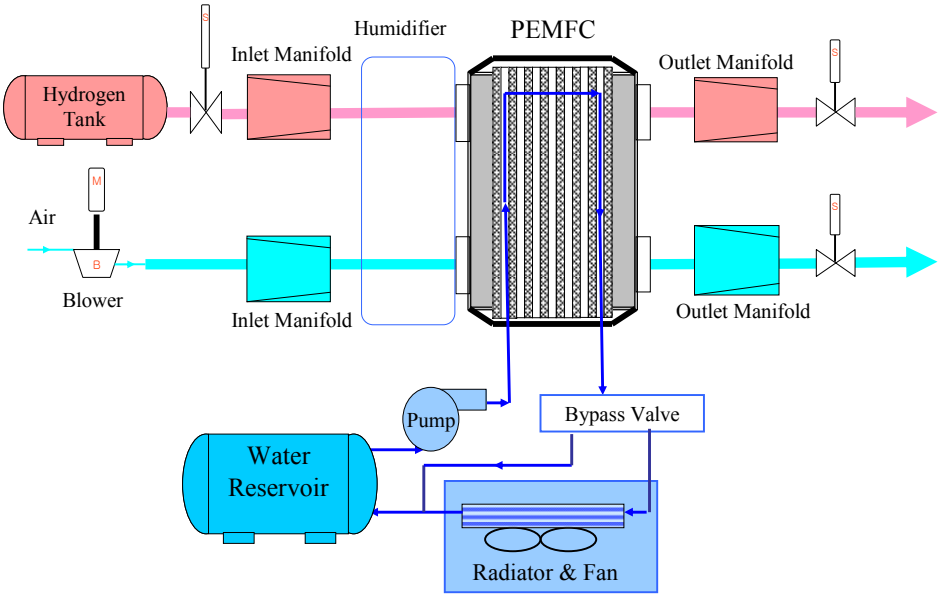


Figure 3 A schematic diagram of a PEM fuel cell system [3]

These auxiliary components constitute the balance of plant (B.O.P). They work dependently of each other because they are connected and influence each other thermodynamically and materially in order to accomplish optimum thermal efficiency. Therefore, each system is made to be able to engage with other components during operation. This balance of plant costs about 70% of the entire fuel cell system. Consequently, the development of the balance of plant, as well as the fuel cell stacks, which needs to satisfy technical specification, safety and economical demand are most important.

## 1.6 APPLICATION TO A QUADRUPED ROBOT

Figure 4 Quadruped robot

One of the main motivations for developing fuel cell based propulsion system for a multi-legged type robot is the possibility of the quietness and compact size of the purely electric propulsion systems, namely high energy and power density. Fuel cell propulsion systems can also profit from various possibilities for improving the fuel economy with respect to ICE-based propulsion systems [2].

# 2 BACKGROUND

PEM fuel cell is an electrochemical energy conversion device whose durability and performance is easily affected by operating condition [2]. Moreover, heat and water is byproduct during an operation of the PEM fuel cell and its appropriate management plays an important role in maintaining and improving the performance of the fuel cell. Therefore, PEM fuel cell system should be operated with careful water and heat management for the performance and durability.

In addition, PEM fuel cell is stacked with many components in the cell such as end plate, gas channel, coolant channel, gas diffusion layer and membrane. Each physical properties like pressure, humidity and temperature is hardly measured for the analysis because it is sealed fully in the enclosure of the fuel cell. Therefore, modeling fuel cell can offer better information and knowledge about physical characteristic of the fuel cell stack.

There are ways to model PEM fuel cell. One is modeling using high order equation for two dimensional or three dimensional model using CFD techniques. C.Y. Wang proposed PEM fuel cell model to describe water generation and liquid water phase in the GDL [4]. It provides information about physical phenomena which occur in the stack. However, it has a limitation to explain behavior in the multi-cell stack due to the slow computational time and over abundance of the parameter and variables used in computer simulation. Other way is using empirical model as low order. J.C. Amphlett proposed lumped thermal model which can describe heat generation and

voltage characteristics [5]. The model can be simple but ignore many physical phenomena such as the coupling of fluid and thermo dynamics. Therefore, there is need for combination of each advantage and minimization of disadvantage. Shan [6] has proposed model which consider effects of a varying load n dynamics of temperature. It is more predictive than empirical model and less complicated than analytical model using medium order equation. However, the model which is mentioned above is developed with single cell or small number of cells in which the temperature effect can be neglected. In the real application such as mobile devices and automobiles, the PEM fuel cell stack is developed as a multi cell stack by connecting a lot of cells about 400 in series. Therefore, the model with large number of cell is needed to be developed to explain the interaction of temperature effect and dynamic behavior of physical properties at varying loads. Based on analysis including comparisons a various operating condition and geometry factor in the model, the model's operating condition is optimized and the 100-cell stack is developed based on 20-cell stack analysis. The operation of a 100-cell stack under varying conditions, and the transient behavior of a step load are analyzed. Temperature distribution and the change of overpotentials along with the associated cell voltages were the major parameters investigated.

# 3 PEM FUEL CELL STACK

In a fuel cell stack, there are complex correlated behaviors between thermodynamics and fluid mechanics. These complex phenomena have been explored either by empirical methods using curve fitted equations or numerical methods exploiting advanced two- or three- dimensional computational fluid dynamics (CFD) techniques. The empirical method is good due to less calculating time and less memory consumed, but is usually valid for a specific steady state. Therefore, empirical methods were not used in analysis of dynamic behavior.

While the CFD techniques can explain dynamic behavior in more detail, the techniques have been limited to analyzing a single cell because of the enormous computational time required for a higher number of cells due to a lot of grid points and the corresponding parameters that need to be determined for simulations. Consequently, a dynamic model for the PEM fuel cell stack is proposed considering temperature distribution and a two-phase effect using empirical equations. The model was used to analyze the dynamic behavior of cell stack.

A fuel cell is an electrochemical energy conversion device. A PEM fuel cell is composed of various layers including bipolar plates, gas diffusion layers, membrane electrode assembly (MEA), and catalyst layers. The model is constructed using two cells connected to each other.

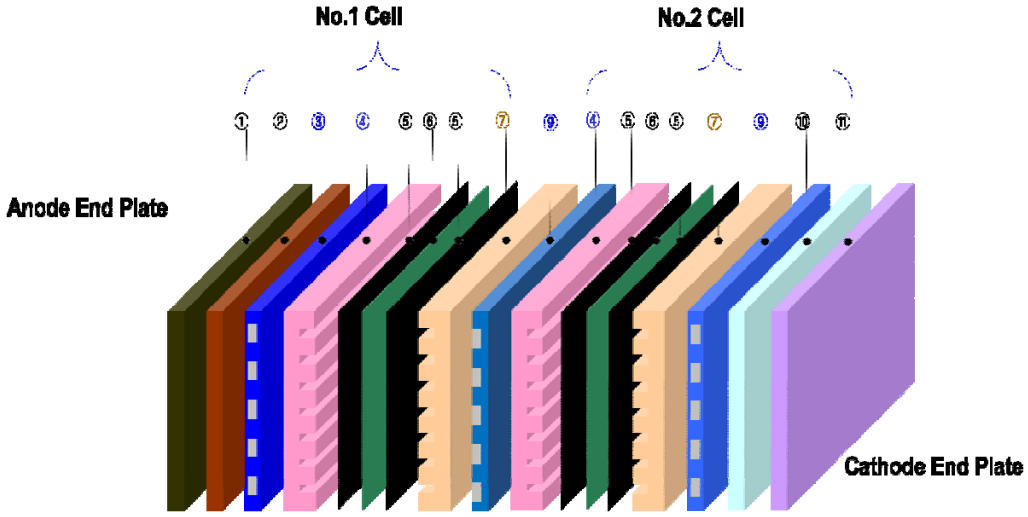


| | | | |
|---|---|---|---|
| 1 | Anode end plate | 6 | Anode catalyst, MEA, Cathode catalyst |
| 2 | Anode bus plate (Current collector) | 7 | Cathode gas channel plate |
| 3 | Anode cooling plate | 8 | Cathode cooling plate |
| 4 | Anode gas channel plate | 9 | Cathode bus plate (Current collector) |
| 5 | Gas diffusion layer | 10 | Cathode end plate |

Figure 5 A schematic diagram of a PEM fuel cell stack

Some assumptions for the modeling are made. All gases in the model obey the ideal gas law. There is no pressure gradient between the anode and cathode side which means no convection, only diffusion when gas transport is considered. There is no gas pressure drop from the inlet to the outlet of the gas channel. The temperature gradient is linear across the layers in a fuel cell. The thermal conductivity for the materials in a fuel cell is constant. Anodic overpotential is negligible. There is no current density gradient across the cathode catalyst layer which means that the reactants completely reacted as

soon as they reach the cathode catalyst layer surface. And finally, latent heat during a phase change is not considered.

Based on these assumptions, the model is developed which is described in the following sections. Static behaviors of a cell model are based on voltage equations and the effects of temperature distribution in a cell, water balance in the membrane, and gas dynamics in the cathode gas diffusion layer with a two-phase phenomenon.

## 3.1 PRINCIPLES

In the system, there are electrochemical reactions at both the anode and cathode side.

Anode: $H_2 \rightarrow 2H^+ + 2e^-$ (3- 1)

Cathode: $\frac{1}{2}O_2 + 2H^+ + 2e^- \rightarrow H_2O$ (3- 2)

To be specific, these reactions occur at the interface between a conductive electrolyte and a conductive electrode. The catalyst usually has a porous structure because the gas reactants should be able to reach the reaction location. The product from this reaction is water that should be ejected properly. The reaction between hydrogen and oxygen usually produces not only water, but also electricity and reaction heat.

$$H_2 + \frac{1}{2}O_2 \rightarrow H_2O + Q + E_{electric} \quad (3- 3)$$

## 3.2 GOVERNING EQUATIONS

The stack model is developed as a single cell at first using some empirical equations. A single cell consists of layers such as the bipolar plate, membrane, catalyst and gas diffusion layer.

### 3.2.1 I-V CHARACTERISTIC

A voltage is calculated by subtracting activation overpotential, ohmic overpotential through membrane and concentration overpotential at cathode catalyst layer from open circuit voltage $E_i$.

$$V_i = E_i - \eta_{i,act} - \eta_{i,ohm} - \eta_{i,con} \tag{3- 4}$$

Open circuit voltage is calculated by considering the relationship between chemical and electrical potential energy [7].

$$E_i = 1.229 - 0.85 \cdot 10^{-3}(T_i - 298.15) + 4.3085 \cdot 10^{-5} \cdot T_i \left[ \ln\left(p_{i,H_2}\right) + \frac{1}{2}\ln\left(p_{i,O_2}\right) \right] \tag{3- 5}$$

As shown in the Butler-Volmer equation, there should be a difference between electrode potential and equilibrium potential in order to accomplish the electrochemical reaction and produce current. This is activation polarization which is related to the slow reaction speed. Therefore, activation polarization loss becomes less as current density increases. The reduction reaction of oxygen usually needs more activation overpotential than the oxidation reaction of hydrogen, which means that reduction reaction is much slower than oxidation reaction [7].

$$\eta_{i,act} = \xi_1 + \xi_2 \cdot T_i + \xi_3 \cdot T_i \cdot \ln(c_{i,O_2}) + \xi_4 \cdot T_i \cdot \ln(I) \tag{3- 6}$$

$$c_{i,O_2} = \frac{p_{i,O_2}}{5.08 \cdot 10^6 \exp(-498/T)} \tag{3- 7}$$

where $\xi_i$ is constant parametric coefficients, $I$ is current (A), $c_{O_2}$ is oxygen concentration.

A resistance loss occurs due to the resistance caused by ion transport at interfaces such as electrolyte membranes and electron transport near the electro-conductive components like electrode surfaces in fuel cells. These losses can be explained by considering Ohm's law [8].

$$\eta_{i,ohm} = i \cdot R_{i,ohm} = \frac{i \cdot t_{mem}}{\sigma_{i,mem}} \tag{3- 8}$$

where $\eta_{ohm}$ is ohmic overpotential, $R_{ohm}$ is the ohmic resistance, $t_{mem}$ and $\sigma_{mem}$ are the membrane thickness and conductivity. The membrane conductivity is dependent upon temperature and water content [8][9].

$$\sigma_{i,mem} = \sigma_i \cdot \exp\left[1268\left(\frac{1}{303} - \frac{1}{T_i}\right)\right]$$
$$\sigma_i = 0.005139 \cdot \lambda_{i,mem} - 0.00326 \tag{3- 9}$$

where $\lambda_{mem}$ is membrane water content.

There is a concentration gradient near an electrode due to the electrochemical reaction as mentioned earlier. The concentration gradient is the cause of concentration overpotential [10].

$$\eta_{i,con} = \frac{RT}{nF} \ln\left(\frac{i_{\max}}{i_{\max} - 1}\right) = -b \cdot \ln\left(1 - \frac{i}{i_{\max}}\right) \tag{3- 10}$$

where $\eta_{con}$ is concentration overpotential, $b$ is parametric coefficient (V), $I$ is actual current density (A $cm^{-2}$), $I_{max}$ is maximum current density (A $cm^{-2}$). The voltage of the stack is the sum of the voltage of each single cell in the stack.

$$V_{stack} = \sum_i V_i \tag{3- 11}$$

Where, $V_{stack}$ is the voltage of the stack and $V_{cell}$ is the voltage of a single cell.

### 3.2.2 ENERGY BALANCE

Energy flow inside of the stack consists of thermal conduction between layers, mass flow into each volume, and convection from reactant flow and coolant under the assumptions that physical properties are independent of temperature and are isotropic. In other words, the energy exchange at the interface of the control volume and the internal heat source constitutes the energy balance. This energy flow can be explained by examining first law of thermodynamics [11].

$$\sum_j m_j \cdot Cp_j \cdot \frac{dT_j}{dt} = \underbrace{\sum \dot{m}_k \cdot Cp_k \left(T_{in} - T_j\right)}_{mass\ flow} + \dot{Q}_{convection} + \dot{Q}_{conduction} + \dot{Q}_{sou} \tag{3- 12}$$

Where, the first term presents mass flow, the second and third terms are convection, the fourth term is conduction heat transfer, and last term is the heat source term.

Entropy change, activation overpotential and ohmic overpotential cause heat generation during the reaction [12].

$$\dot{Q}_{sou} = i \cdot A\left(-\frac{T_i \cdot \Delta S}{n \cdot F} + \eta_i + i \cdot R_{ele}\right) \tag{3- 13}$$

### 3.2.3 WATER BALANCE

A membrane should offer high conductivity appropriately and be chemically and mechanically stable under the fuel cell's operating conditions. The water balance in the

membrane is managed by the electro-osmotic driving force caused by the difference in electrochemical potential at both the anode and cathode, while the diffusion caused by the difference in concentration results in a concentration gradient.

Conductivity of a polymer electrolyte membrane is mainly dependent on the type of structure and water content in a membrane. The maximum water content of a membrane can be determined by the phase of water in the membrane. Usually, the forming of liquid water increases water content in the membrane.

The water content in the membrane is calculated with consideration of mass flow at the boundaries within the membrane [11].

$$\lambda_{i,mem} = \frac{C_{i,H_2O,mass} / M_{H_2O}}{\frac{\rho_{dry,mem}}{M_{mem}} - 0.0126 \cdot C_{i,H_2O,mass} / M_{H_2O}}$$
$$\dot{m}_{i,mem} = \frac{d\left(C_{i,H_2O,mass} \cdot A \cdot t_{mem}\right)}{dt} = \dot{m}_{i,ele,mem,an} - \dot{m}_{i,ele,mem,ca} + \dot{m}_{i,diff,mem,an} + \dot{m}_{i,diff,mem,ca} \quad (3\text{-}14)$$

where $C$ is mass concentration (kg $m^{-3}$), $M$ is mole mass (kg $mol^{-1}$), $\rho$ is membrane dry density and $A_{cell}$ is fuel cell area ($m^2$).

As mentioned earlier, there are different ways to transport the water. The electro-osmotic driving force is one of the causes that induce water mass flow across the membrane layer. The water is produced from the electrochemical reaction while the rate of water production is a function of load [8].

$$N_{H_2O,generation} = \frac{i}{2F} \quad (3\text{-}15)$$

where $N_{H2O,generation}$ is the rate of water generation (mol $cm^{-2}$ $s^{-1}$).

Water is carried by the electro-osmotic drag force with the protons which move from anode to cathode. The electro-osmotic drag coefficient is a function of water content [8].

$$\dot{m}_{i,ele,mem,l} = M_{water} \cdot A \cdot n_{d,i,l} \cdot \frac{i}{F} \tag{3- 16}$$

$$n_{d,i,l} = 0.0029 \cdot \lambda_{i,l}^2 + 0.05 \cdot \lambda_{i,l} - 3.4 \cdot 10^{-19} \tag{3- 17}$$

The concentration gradient at the boundaries of the membrane layer increases due to water generation and water transport caused by the electro-osmotic drag force. Diffusion, $W_{diff,mem}$, is caused by this concentration gradient. In some cases, the concentration gradient is capable of reverse diffusion, from cathode to anode, during operation [8].

$$\dot{m}_{i,diff,mem,l} = M_{water} \cdot A \cdot D_{water,i,l} \frac{\left(C_{i,l} - C_{i,mid}\right)}{t_{mem}} \tag{3- 18}$$

$$C_{i,l} = \frac{\rho_{dry,mem}}{M_{mem}} \cdot \lambda_{i,l} \ , \ C_{i,mid} = \frac{\rho_{dry,mem}}{M_{mem}} \cdot \lambda_{i,mem} \tag{3- 19}$$

The diffusion coefficient is proposed in the form of an empirical equation [8].

$$D_{water,i,l} = D_{\lambda,i,l} \cdot \exp\left(2416\left(\frac{1}{303} - \frac{1}{T_{mem,i}}\right)\right) \tag{3- 20}$$

$$D_{\lambda,i,l} = \begin{cases} 10^{-6} & 2 > \lambda_{i,l} \\ 10^{-6} \cdot \left(1 + 2\left(\lambda_{i,l} - 3\right)\right) & 3 \geq \lambda_{i,l} \geq 2 \\ 10^{-6}\left(3 - 1.67\left(\lambda_{i,l} - 3\right)\right) & 4.5 > \lambda_{i,l} > 3 \\ 1.25 \cdot 10^{-6} & \lambda_{i,l} \geq 4.5 \end{cases} \tag{3- 21}$$

The water content is also calculated as a function of water activity [8].

$$\lambda_{i,l} = \begin{cases} 0.043 + 17.81 \cdot a_{i,l} - 39.85 \cdot a_{i,l}^2 + 36 \cdot a_{i,l}^3 & 1 \geq a_{i,l} > 0 \\ 14 + 1.4\left(a_{i,l} - 1\right) & 3 \geq a_{i,l} > 1 \\ 16.8 & a_{i,l} \geq 3 \end{cases} \tag{3- 22}$$

The water activity is a relationship between water vapor partial pressure and saturation pressure [8].

$$a_{i,l} = \frac{P_{v,i,l}}{P_{sat,i,l}} \tag{3- 23}$$

### 3.2.4 GDL WITH 2 PHASE EFFECT

Water in the form of a liquid plays a pivotal role in improving performance by increasing proton conductivity or decreasing performance by impeding the transport of gas reactants. Not only the gas phase, but also the liquid phase - which has not been previously considered - are taken into account, diffusivity should be modified to effective diffusivity which represents the diffusion characteristic of liquid water and water vapor in a capillary in order to show the dynamic behavior of the water. It is a function of the diffusion coefficient, porosity of diffusion layer, and liquid water saturation ratio [13].

$$\begin{aligned} &\langle D_m(k) \rangle = D_m \varepsilon \left( \frac{\varepsilon - 0.11}{1 - 0.11} \right)^{0.785} \left(1 - s(k)\right)^2 \\ &\varepsilon = \frac{V_{pore}}{V_{GDL}}, \quad s(k) = \frac{V_{liquid}(k)}{V_{pore}} \\ &m = O_2, vapor \end{aligned} \tag{3- 24}$$

where $<D_j>$ is effective diffusivity ($m^2 s^{-1}$), $D_j$ is diffusion coefficient ($m^2 s^{-1}$) at a single phase, $\varepsilon$ is porosity of diffusion layer (-), $s$ is liquid water saturation ratio (-), $V_p$ is pore volume of the GDL ($m^3$), $V$ is total volume of GDL($m^3$), and $V_l$ is volume of liquid water ($m^3$).

Effective diffusivity of gas diffusion layer is developed by using fiber screen model [13]. Real fiber structure is shown as Figure 6 (c). Its randomly overlapped structure is hard to be modeled with pore space. Moreover, the GDL used in PEM fuel cell is stacked fibrous structure. Therefore, it is hard to define and measure pore portion inside the GDL. The microscale model for GDL is developed based on the assumption that the pore spaces is made by four interwoven fiber as a square shape. This makes modeling GDL much easier and its porosity can be calculated as a volumetric ratio. However, its height is assumed to be a same size. Consequently, porosity of the GDL can be derived as below [13].

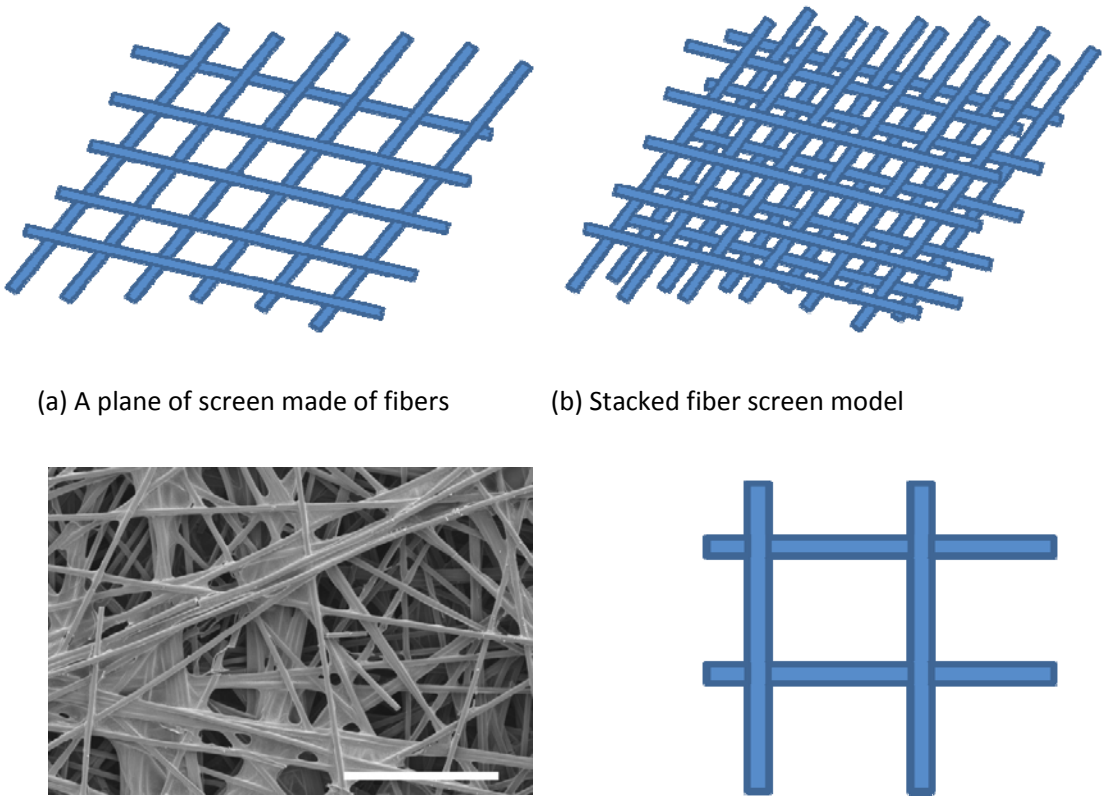

(a) A plane of screen made of fibers (b) Stacked fiber screen model

(c) Random fiber structure (d) Unit square pore space

Figure 6 Mocroscale GDL model

$$\varepsilon = \frac{d_p^{\,2}}{(d_p + d_f)^2} \tag{3- 25}$$

where $d_p$ is pore size and $d_f$ is the representative fiber diameter (m).

The mass conservation is in the control volume, that is, each section in the gas diffusion layer is considered in order to describe the volume of liquid water. There are two types of behavior in the control volume, liquid water flow by concentration gradient and evaporation [13].

$$\rho_l \frac{dV_l}{dt} = \dot{m}_{l,in} - \dot{m}_{l,out} - \frac{R_{evap} V_p M_v}{\varepsilon} \tag{3- 26}$$

where $\rho_l$ is density of liquid water (kg $m^{-3}$), $\dot{m}_l$ is mass flow rate of liquid water (kg $s^{-1}$), $R_{evap}$ is molar evaporation rate (mol $sec^{-1}$ $m^{-3}$), $M_v$ is molecular weight of vapor (kg $mol^{-1}$) and $\varepsilon$ is porosity of the diffusion layer (-).

Evaporation rate, which is related to the volume of liquid water, is mainly dependent on the difference between the saturation pressure and water vapor pressure [13].

$$R_{evap}(k) = \gamma \frac{p_{v,sat}(T) - p_v(k)}{RT},\ p_v = c_v RT \tag{3- 27}$$

where $\gamma$ is volumetric condensation coefficient ($s^{-1}$), $P_{v,sat}$ is saturation pressure (Pa), $P_v$ is partial pressure of vapor (Pa) in each region, $c_v$ is molar concentration of vapor (mol $m^{-3}$), $R$ is ideal gas constant (J $kg^{-1}$ $K^{-1}$) and $T$ is absolute temperature (K).

## 3.3 MODEL DIAGRAM

The structure of the model is developed by the SIMULINK, which has a graphical interface and block diagram. The program allows us to analyze dynamic behavior arranging theses icons into a block diagram representation of a dynamic process.

As explained above, each layer is connected with consideration of heat and mass transfer. The layers are developed using continuity equation and heat transfer equation at the end plate, coolant channel and gas channel. Specifically, catalyst layer uses electrochemical equation such as open circuit voltage, activation overpotential and concentration overpotential equation. Membrane uses important equation which decides proton conductivity, membrane water content and ohmic overpotential. Finally, GDL of cathode is developed using a two-phase effect for the explanation of flooding phenomena. Like this, anode and cathode part are developed and composed.

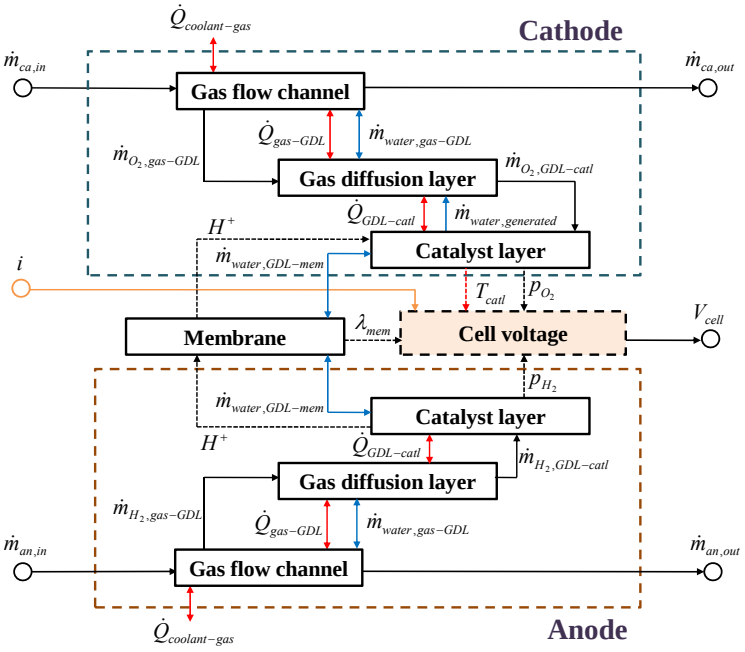


Figure 7 Fuel cell stack model schematic block diagram

# 4 BALANCE OF PLANT

The fuel cell system is composed of many subsystems such as an air processing system, a fuel processing system, thermal management and water management as well as the fuel cell stack system. There are also many components to these subsystems such as a blower, hydrogen tank, humidifier, water reservoir, purge valve, and a deionized water pack. Proper operation of each subsystem and its components makes a successful fuel cell system work. Fuel cell system is organized like the following.

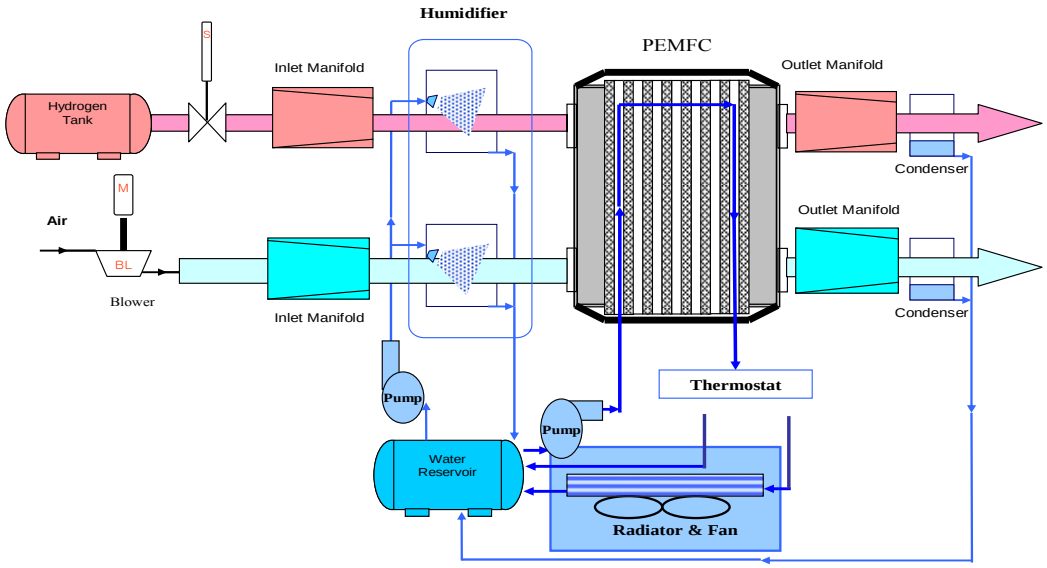


Figures 8 A schematic diagram of balance-of-plant for PEM fuel cell system [3]

## 4.1 AIR PROCESSING SYSTEM

### 4.1.1 SYSTEM CONFIGURATION AND COMPONENTS

Air is one of the important reactants needed in order to produce electricity in a fuel cell. Considering the stoichiometric ratio, the proper amounts of fuel and air should be supplied. For this, the air supply system is composed of a blower driven by a motor humidifier, manifold and others.

The blower serves to provide the specific amount of air required. Moreover, a specially designed blower, such as a high pressure blower, is preferred for a fuel cell system. A brushless motor is usually used in fuel cell systems to prevent leaking fuel from being ignited and exploded.

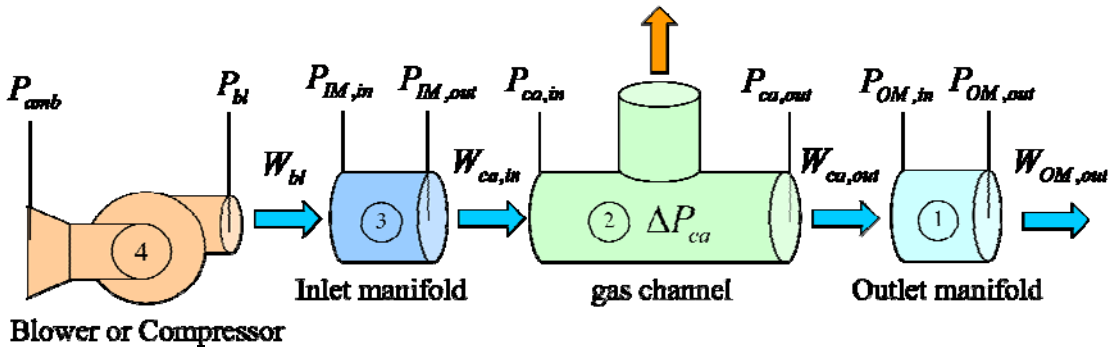


Figure 9 A schematic diagram of air processing system

### 4.1.2 BLOWER

The current blower model was originated from a characteristic curve which was composed of the efficiency and flow rate curves depending on head loss parameters.

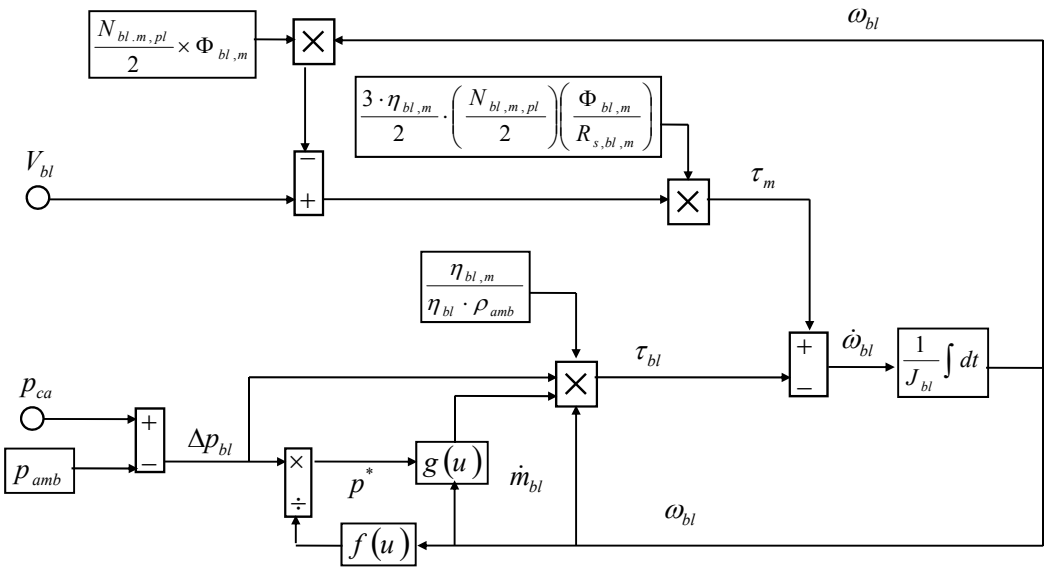


Figure 10 A block diagram of blower model

The blower is operated by a DC brushless motor, but its electrical characteristics are not considered. The output of the blower model is significantly affected by the inertia of the rotor, the required torque and the applied torque.

#### 4.1.2.1 MOTOR-INPUT VOLTAGE

#### 4.1.2.1.1 BLOWER SPEED

The dynamic behavior of the blower speed is described by the moment of the inertia. The blower torque is the difference between the motor toque applied and the blower's load torque.

$$J_{bl}\dot{\omega}_{bl} = \tau_m - \tau_{bl} \tag{4- 1}$$

Where $\tau_m$ is motor torque (N m) and $\tau_{bl}$ is blower torque (N m).

The motor torque is a function of the power input and motor speed. The required blower torque is also a function of power and speed but some additional losses occur due to the blower's loading torque. Thus the equations for torque are

$$\tau_m = \frac{P_m}{\omega}$$
$$\tau_{bl} = \frac{P_{bl}}{\omega} \tag{4- 2}$$

where the required power of the blower, $P_{bl}$ (W), is calculated by the thermodynamic power equation.

The motor torque is calculated and linearized under the three phase balanced operation representation [5].

$$\frac{d\omega_{bl}}{dt} = \frac{1}{J_s}\left(\tau_{bl,m} - \frac{\dot{W}_{bl}\eta_{bl,m}}{\omega_{bl}}\right) \tag{4- 3}$$

$$\dot{W}_{bl} = \frac{\dot{m}_{bl}\Delta p_{bl}}{\eta_{bl}\rho_{amb}} \tag{4- 4}$$

$$\tau_{bls,m} = \eta_{bl,m}\frac{3}{2}\left(\frac{N_{bl,m,pl}}{2}\right)\left(\frac{\Phi_{bl,m}}{R_{s,bl,m}}\right)\left[V_{rqs,bl,m} - \left(\frac{N_{bl,m,pl}}{2}\right)\Phi_{bl,m}\omega_{bl}\right] \tag{4- 5}$$

where $\tau_{bl,m}$ is a torque produced by the motor (J), $W_{bl}$ is blower work (J), $R_{s,bl,m}$ is a function of the stator resistance(Ohm), $\Phi_{bl,m}$ is flux linkage (V s $^{-1}$ rad$^{-1}$) and $n_{bl,m,pl}$ is the number of the poles with the stator voltage, $V_{bl,m}$ (V).

### 4.1.2.2 AIR FLOW RATE

The total mass flow rate is calculated as a function of the angular velocity and pressure, and the efficiency given as a function of the flow rate and the angular velocity [16]. The blower map is used to determine the air flow rate through the blower [14].

$$\begin{aligned}
&\dot{m}_{bl} = \omega_{bl}\cdot\left(-10.29\cdot\left(p^*\right)^2 - 0.72\cdot10^{-3}\cdot p^* + 2.07\cdot10^{-5}\right),\ p^* \le 9\cdot10^{-4}\ Pa\cdot s^2/rad^2 \\
&\dot{m}_{bl} = \omega_{bl}\cdot\left(-0.9\cdot p^* + 0.82\cdot10^{-3}\right),\ p^* \ge 9\cdot10^{-4}\ Pa\cdot s^2/rad^2
\end{aligned} \tag{4- 6}$$

Where $p^*$ is $\left(\frac{p_{ca} - p_{amb}}{\omega_{bl}^2}\right)$.

The parameters of the blower were extracted from desired specifications and characteristic data delivered by PADT (Phoenix Analysis & Design Technologies) [15].

In a low pressure system,

$$\left(\frac{p_{manifold}}{p_{atm}}\right) \approx 1,\ T_{manifold} \approx T_{bl} \approx T_{atm} \tag{4- 7}$$

The air flow characteristics are air mass flow, temperature, pressure, relative humidity, and the oxygen mole fraction. But in a low pressure system, temperature, pressure, and relative humidity are the same as atmospheric ones while the oxygen mole fraction is 0.21.

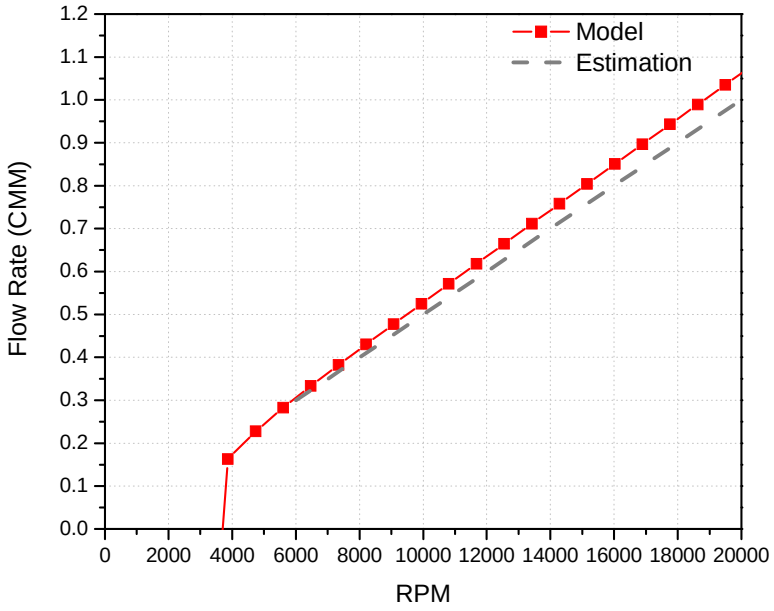


Figure 11 Estimation of blower characteristics and simulation of blower model

## 4.2 THERMAL CIRCUIT

Products from the chemical reaction in a PEM fuel cell include not only electricity and water but also heat. Excessive heat is able to raise the temperature of a PEM fuel cell abnormally causing damage to the stack. An appropriate temperature is

critical in order to increase the performance of a PEM fuel cell, such as conductivity in the membrane which is directly related to the water content in the membrane. Therefore, an appropriate thermal management system plays an important role in the successful operation of fuel cell stacks.

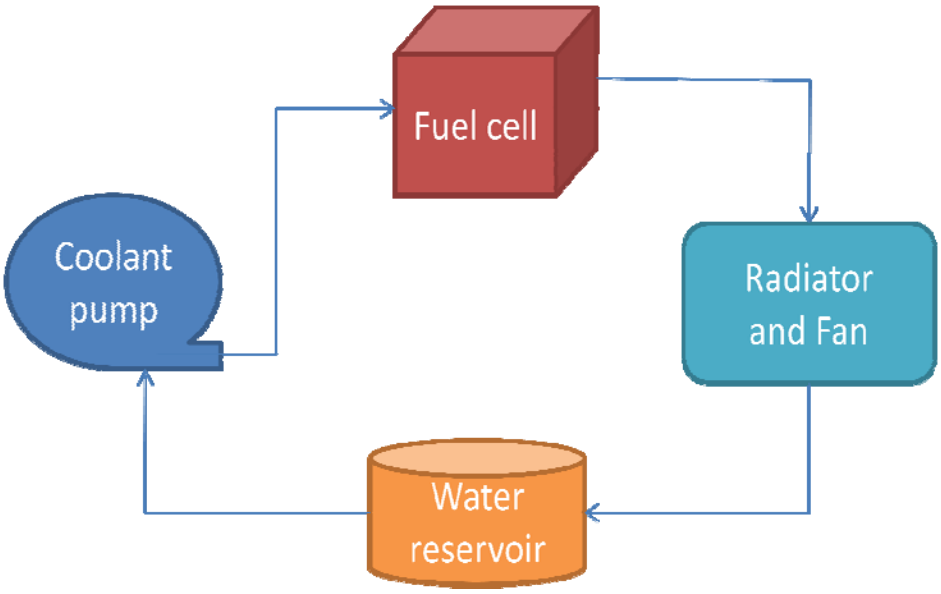


Figure 12 A schematic diagram of thermal circuit

The thermal circuit is composed of a radiator, fan, coolant pump and water reservoir. The selection of the proper size of a pump and a radiator is necessary because the thermal system should be able to reject the excessive heat generated in the PEM fuel cell. An approximation of the heat produced can be calculated as a function of current, entropy, overpotential and ohmic overpotential [12].

$$\dot{Q}_{sou} = i \cdot A\left( -\frac{T_i \cdot \Delta S}{n \cdot F} + \eta_i + i \cdot R_{ele} \right) \quad (4\text{- }8)$$

The cell stack generates approximately 20 kW of heat during maximum output. Heat produced can be assumed to be the activation and ohmic voltage loss which varies depending on load current density.

$$V = E - \Delta V_{ohm} - \Delta V_{act} - \Delta V_{conc}(V) \quad (4\text{- }9)$$

Therefore, the capacity of a coolant pump and a radiator should be decided based on the operating conditions and required specifications. The maximum possible heat produced will occur at maximum current density within range of operation, and the thermal components should satisfy all of the cooling demands.

Heat rejected by the thermal system from the stack to coolant is determined by the coolant flow rate and the intended temperature difference between the stack inlet and outlet.

$$\dot{Q}_{coolant} = \dot{Q}_{generated} \cdot \eta_{transfer} = \dot{m}_{coolant} \cdot C_{p,coolant} \cdot \Delta T_{coolant}(\dot{m}) \quad (4\text{- }10)$$

After the heat produced and the required temperature difference is calculated, the necessary coolant flow rate can be calculated. Heat is needed to reject about 20 kW from the calculation using equation above for heat generation rate during operation of the PEM fuel cell at maximum power.

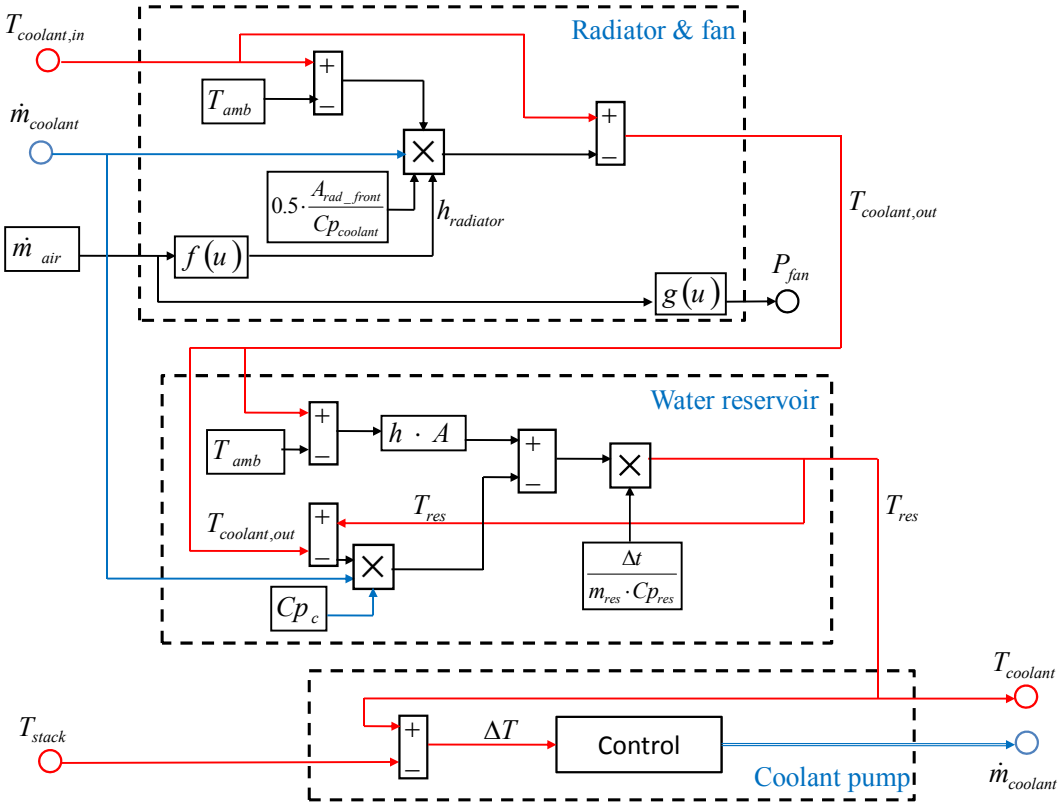


Figure 13 Thermal circuit block diagram

### 4.2.1 COOLANT PUMP

The coolant pump plays a pivotal role in circulating the coolant in the circuit from the heat source to the heat exchanger. Under the assumption that heat produced during the operation is rejected fully by the coolant, the required mass flow rate is calculated using the calculated heat generation, type of coolant, i.e. heat capacity of coolant, and temperature difference between inlet and outlet.

$$\dot{m}_{cool} = \frac{\dot{Q}_{stack_gen}}{Cp_{cool} \cdot \Delta T} \tag{4- 11}$$

There are some different ways to calculate the heat balance. Generally, the chemical energy of the fuel is converted into electricity while the rest of the chemical energy is changed into heat. Under the assumption that the only product is water vapor, the low heat value can be used which is used for calculating the heat generated.

### 4.2.2 RADIATOR

The radiator plays an important role in rejecting excessive heat to its ambient while it makes the PEM fuel cell operate at its desired constant working temperature for any load. The capacity of the radiator should be determined considering the amount of heat which is carried by the coolant.

$$\dot{Q}_{coolant} = \dot{Q}_{radiator} \tag{4- 12}$$

Moreover, the required temperature difference, coolant flow rate, and heat transfer coefficient of the radiator should be utilized to determine the frontal area of the heat exchanger [16].

$$A_{radiator} = \frac{\dot{m}_{coolant} \cdot C_{p,coolant} \cdot \Delta T_{coolant}}{\left(T_{coolant,stack} - T_{ambient}\right) \cdot h_{radiator}} \quad [m^2] \tag{4- 13}$$

The heat transfer coefficient is determined by an empirical value proposed by D.G Kroger [16]. It is dependent upon the mass flow rate which is a function of the fan speed.

$$h_{radiator} = f(\omega_{fan}) = f(\dot{m}_{air})\left(\mathrm{W\,m^{-2}K^{-1}}\right) = -1.4495\dot{m}_{air}^2 + 5.9045\dot{m}_{air} - 0.1157 \quad (4\text{-}14)$$

where $P_r$ is pressure drop (kPa) and $h_{rad}$ is heat transfer coefficient (W $m^{-2}$ $K^{-1}$).

The capacity of the heat exchanger is dependent on the amount of heat which should be rejected by the coolant. The characteristic of the heat exchanger are determined by the heat transfer area, the temperature difference between inlet, or ambient, and outlet temperatures, and the heat coefficient which is controlled by the fan speed. Once the mass flow rate is determined, the temperature difference of the coolant can be calculated. The temperature difference is a typical design parameter which is usually less than 5°C, but not over 10°C. As the coolant mass flow rate is increased, the temperature difference decreases. However, this increases the parasitic loss of the system due to the coolant pump [17].

$$T_{coolant_out} = T_{coolant_in} - \left( \frac{A_{rad_front}(T_{st_out} - T_{amb})h_{rad}}{\dot{m}_{coolant} C_{p,coolant}} \right) \quad (4\text{-}15)$$

where $A_{rad_front}$ denotes the frontal area ($m^2$) of the radiator and $T_{st,out}$ is the stack outlet coolant temperature which is the same as the radiator inlet coolant temperature.

The fan is able to increase the mass flow rate of the air which increases the heat transfer coefficient which improves the thermal circuit's cooling characteristics. However, the fan also consumes electric power as it spins and blows air. Moreover, the pressure drop across the radiator increases as the mass flow rate increases because the friction from the surface of the radiator increases [17].

$$P_r = (326.12\dot{m}_{air} - 75.396) + 101.325 \quad (4\text{-}16)$$

where $P_r$ is pressure drop (kPa).

The required power for the fan is calculated as follows using the thermodynamic power equation under the assumption that compression is an isotropic process [17].

$$P_{fan} = \frac{1}{\eta_{elec}\eta_{fan}}\left(\dot{m}_{air} Cp_{air} T_{amb}\left(P_r^{\left(\frac{k-1}{k}\right)} - 1\right)\right) \quad (4\text{-}17)$$

where $P_{fan}$ denotes the electric power (W) of the fan.

### 4.2.3 WATER RESERVOIR

Water used as the coolant needs to be stored in a reservoir for safe circulation and minimizing additional heat transfer after cooling down through the heat exchanger. There are three major kinds of heat transfer in the reservoir system. One is the heat carried in by the coolant, another is transfer between coolant and reservoir surface through conduction and the other is transfer between reservoir surface and the ambient air through convection [17].

$$T_{res} = T_{res}^{p} - \frac{\Delta t}{m_{res} \cdot Cp_{res}}\left[\dot{m}_c \cdot Cp_c\left(T_{res}^{p} - T_{r,i}\right) + h \cdot A\left(T_{r,i} - T_{amb}\right)\right] \quad (4\text{-}18)$$

where $T_{res}$ is the reservoir outlet coolant temperature at the end of time step (K), $T_{res}^{p}$ is temperature of the reservoir at the beginning of time step (K), $\Delta t$ is time interval (sec), $m_{res}$ is equivalent mass of the coolant in the reservoir (kg), $Cp_{res}$ is specific heat (J $kg^{-1}$ $K^{-1}$), $h$ is heat transfer coefficient of the reservoir, and $T_{r,i}$ is temperature of coolant into reservoir (K).

# 5 ANALYSIS OF A TWO-CELL STACK

The characteristic of the stack should be analyzed for better operating condition and geometry parameter before the stack is designed and operated. Therefore, the two-stack is analyzed under the varying operating condition and various geometry parameter.

### 5.1.1.1 COMPARISON BETWEEN SIMULATIONS AND EXPERIMENTS FOR A TWO-CELL STACK

Using the model, a two-cell stack was simulated to analyze static and dynamic behaviors. The I-V characteristics calculated for the stack and the individual cells were compared with the experimental data collected [6] at a test station installed at Auburn University. Operating temperature was 333.15 K. Stoichiometric ratio was 1.2 and 3 for each anode and cathode side. Cathode side is humidified as 100% while anode is supplied with dry hydrogen gas.

Figure 14 shows comparison between the simulated and experimental results [6] of the voltage across the stack. The simulated and experimental stack voltages matched well, but the deviation of the two cell voltages in the experimental results was larger than that of the simulated results. Differences in the two cells could be caused by non-uniform characteristics of the individual cells such as reactant distributions and the properties of the GDL and the membrane. Details describing the effects of various factors on the cell voltages are described in Park, SK and Choe, SY [6][16][27].

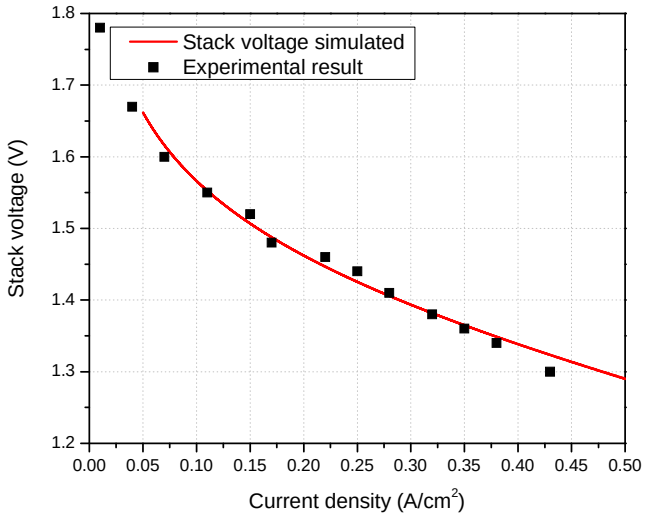


Figure 14 Comparison of the simulated and experimental two-cell stack and individual cell voltages

### 5.1.1.2 COMPARISON BETWEEN A SINGLE PHASE AND A TWO PHASE MODEL FOR A TWO CELL STACK

The structure of the two-cell stack was the same as that depicted in the Fig. 4 except that a separator between the two coolant channels was used to minimize the coupled cooling effects of adjunct cells on performance. Operating conditions were as follows: the stoichiometric ratio for the anode was 1.2 and that for the cathode was 2.0. The gas pressure, supply gas temperature, and relative humidity on both sides were 1.0 bar, 333.15 K and 100%, respectively. The average temperature of coolants at the exit of cell 1 and 2 for the single-phase model was maintained at 333.15 K by controlling the

coolant inlet temperature, and the coolant flow rate was constant at 0.003 (kg $s^{-1}$). The two-phase model used the same coolant temperature and flow rate.

I-V characteristics and temperature distribution of a two-cell stack are illustrated in Figure 15. The voltages between cell 1 and cell 2 are larger which can be seen in Figure 15(a) when current load is increased. The difference in the cell voltages between a single-phase and two-phase is affected by liquid water that is often neglected in previous single-phase modeling. When the density of the load current is higher than 0.4 (A $cm^{-2}$), the influence of liquid water reduces the performance of the cells and the voltage difference between the cells becomes larger. As a result, the voltage drop of the two-phase model is larger than that of the single-phase model. However, it should be noted that the liquid water did not significantly limit the current density in comparison to the results of other analyses because the gradient of water concentration, the pressure and temperature drop along the flow channel have not been fully considered in this modeling [18].

Figure 15 (b) shows the temperature distributions in the stack at the given profile of current density. When liquid water was considered, the overpotential in the cells was higher than when in single phase, and subsequently the associated heat produced was more than that observed in a single-phase model. As a result, the working temperature in the cells became higher. In addition, the geometrical distribution of the heat sources in the stack was asymmetrical. Accordingly, heat transfer rate from the heat sources to the coolants was not identical, which caused an asymmetrical temperature profile in that the temperature in cell 1 was higher than that in cell 2. The ohmic overpotential was affected by the temperature and water content in the membrane. The temperature in the membrane

of cell 2 was higher than that of cell 1. In addition, the cathode gas channel temperature of cell 2 was lower than that of cell 1. The saturation vapor pressure was also lower which augments the RH in cell 2 and water content. Consequently, the ohmic overpotential in cell 2 became lower than that in cell 1 and determined the deviation of the amplitude of the two cell voltages.

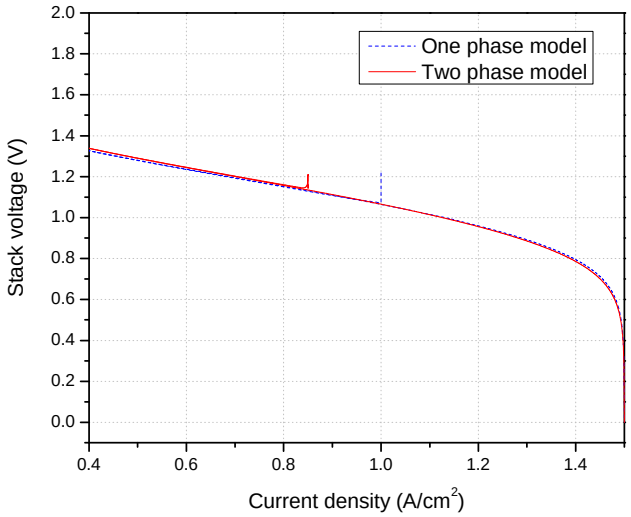


(a) Calculated polarization curves of single-phase and two-phase models for a 2-cell stack.

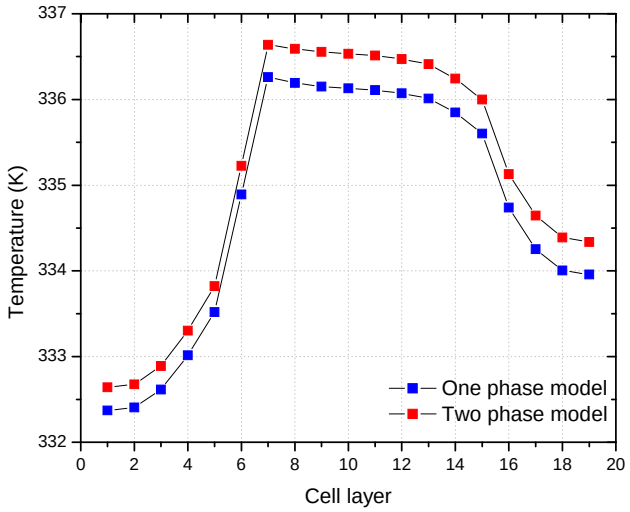


(b) Temperature distribution in a two-cell stack

Figure 15 I-V curve and temperature of a two cell stack under the ramp input of current density.

### 5.1.1.3 PARAMETRIC STUDY FOR OPERATING CONDITION

#### 5.1.1.3.1 TEMPERATURE

Temperature is a parameter that can be set prior to operation of a PEM fuel cell. Generally, higher temperatures can make higher cell voltages. However, each optimized temperature could be different and should meet each different PEM fuel cell's system conditions.

The inner temperatures of a PEM fuel cell are different across each of the layers which constitute the fuel cell stack. Therefore, a temperature measurement is dependent

on the particular location where the measurement is taken. For example, the temperatures of the inside and outside are different. The temperatures of the anode catalyst layer and cathode catalyst layer are also different. There are some different ways to estimate the operating temperature of the fuel cell system. The first method is by measuring the temperature of the surface of the PEM fuel cell. The next method is by measuring the temperature of the air outlet. The last one is by measuring the temperature of the stack's coolant outlet. All of these methods are an estimation of the fuel cell temperature but are not exactly same because the temperature differences means that there is heat transfer inward or outward in the PEM fuel cell system. Consequently, determining the appropriate spot for measuring temperature should be done so by considering the material's heat conductivity, reactant gas mass flow rate, and coolant mass flow rate.

Figure 16 shows the temperature dependent I-V, power and overpotentials' characteristic curves which are constituted of cell voltages at different operating temperatures of 60, 70 and 80 $^{o}$C. When the air temperature increased, the cell voltages tended to increase because of predominantly decreased ohmic overpotential.

An increase in temperature cause lower open circuit voltage (Eq.3-5). Activation overpotential and ohmic overpotential also decrease with increase in temperature according to increasing in temperature (Eq. 3-6 and 8). The water vapor pressure in the GDL increased at an elevated air temperature, and there is more water vapor because of the assumption that there is always saturated vapor. Subsequently, the membrane water content increased, and the ohmic overpotential decreased.

However, the rate of the decreasing activation overpotential and ohmic overpotential compensate that of the decreasing open circuit voltage. Consequently, the cell voltage and power in the simulation results increase.

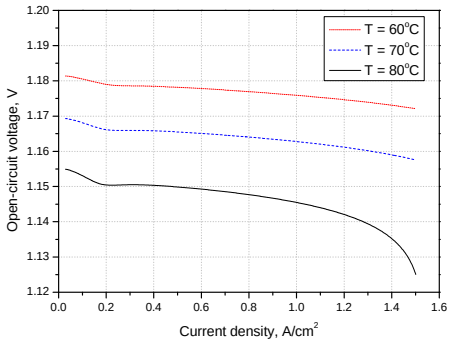


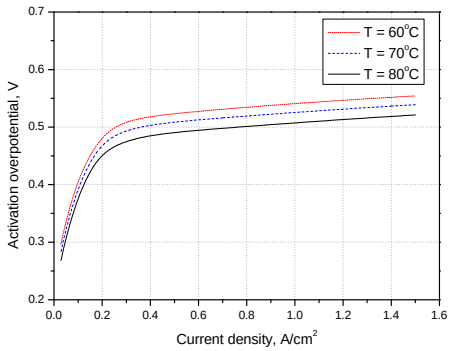


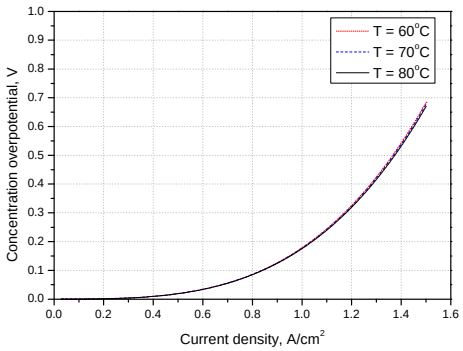


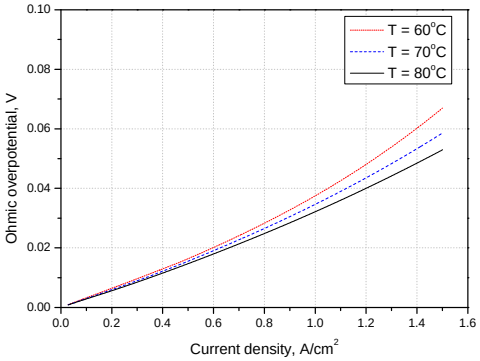

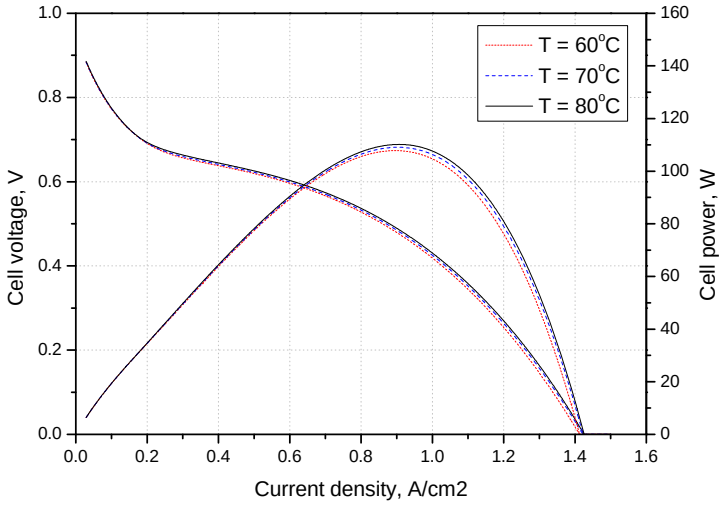


Figure 16 I-V characteristic, power and overpotential for different operating temperature

### 5.1.1.3.2 STOICHIOMETRIC RATIO

The reactant gas supplied should be greater than or equal to the amount of reactant gas required in order to perform desirably. Usually, the required reactant gas, air, and hydrogen can be calculated using Faraday's Law.

$$\dot{m}_{H_2} = \frac{I}{2F} M_{H_2}$$
$$\dot{m}_{O_2} = \frac{I}{4F} M_{O_2} \qquad (5\text{-}1)$$

where $I$ is current (A), and $F$ is Faraday constant(C $mol^{-1}$).

Figure 17 shows the stoichiometric ratio dependent I-V, power, and overpotentials' characteristic curves with different stoichiometric ratio of 2, 3 and 4. When the air stoichiometric flow ratio increased, the water was easily removed and the water content in the membrane decreased. As a result, the ohmic overpotential increased. At the same

time, the oxygen concentration near the catalyst increased and as a result, the activation overpotential decreased. However, the rate of the decreasing activation overpotential and concentration overpotential is higher than that of the increasing ohmic overpotential, and subsequently, the cell voltages increased.

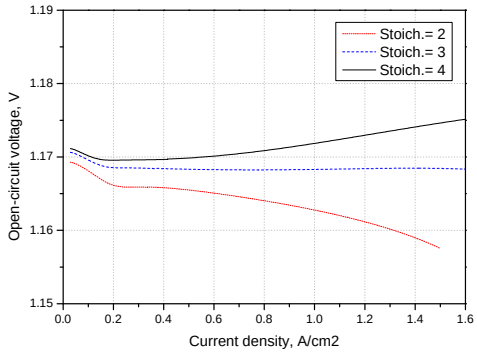


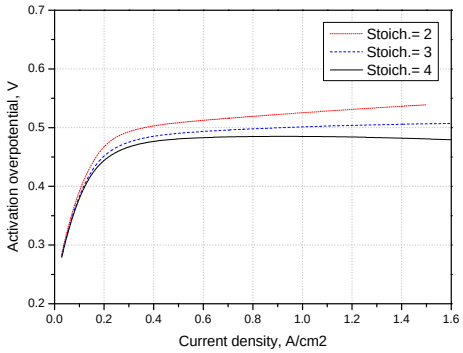


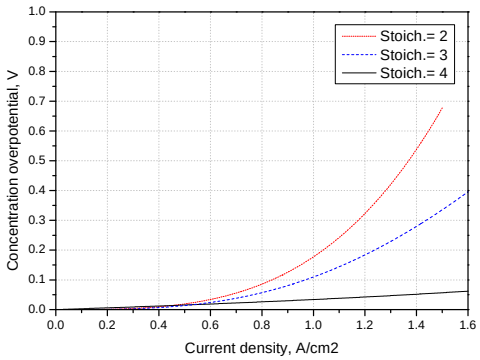


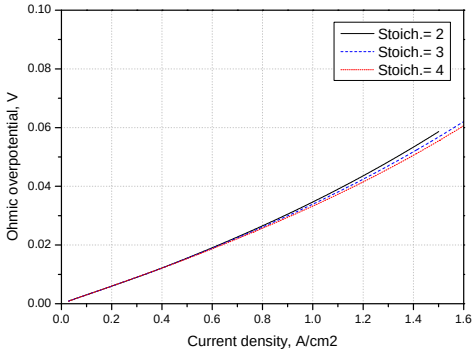

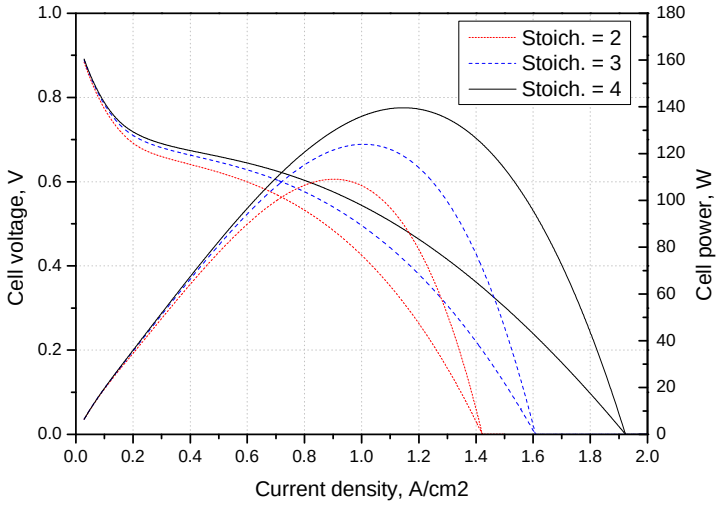


Figure 17 I-V characteristic, power and overpotential for different stoichiometric ratio

### 5.1.1.3.3 RELATIVE HUMIDITY

PEM fuel cells have the good characteristics that allow for operation at lower temperatures. Thus, water management is one of the most important issues. Maintaining high proton conductivity at the electrolyte membrane through appropriate water management plays an important role in producing higher cell voltages and increasing performance.

Figure 18 shows the relative humidity dependent I-V, power, and overpotentials' characteristic curves from the simulation's results at different relative humidity.

When the relative humidity increased, the cell voltages tended to decrease due to the liquid water saturation. The relative humidity of the air inlet affected the concentration of oxygen in the gas flow channel as well as water removal. At a fixed air pressure composed of the oxygen, nitrogen and vapor, the increase in relative humidity

led to a high pressure of vapor and a low pressure of oxygen. Therefore, the oxygen concentration at the GDL/CL interface decreased, and as a result, the activation overpotential increased.

As the relative humidity at the inlet increased, the water content in the membrane tended to increase rapidly, and subsequently, the ohmic overpotential decreased. Although the activation overpotential increased, the magnitude of the decrease in ohmic overpotential was much higher than that of the increase in the activation overpotential. Consequently, the cell voltages decreased.

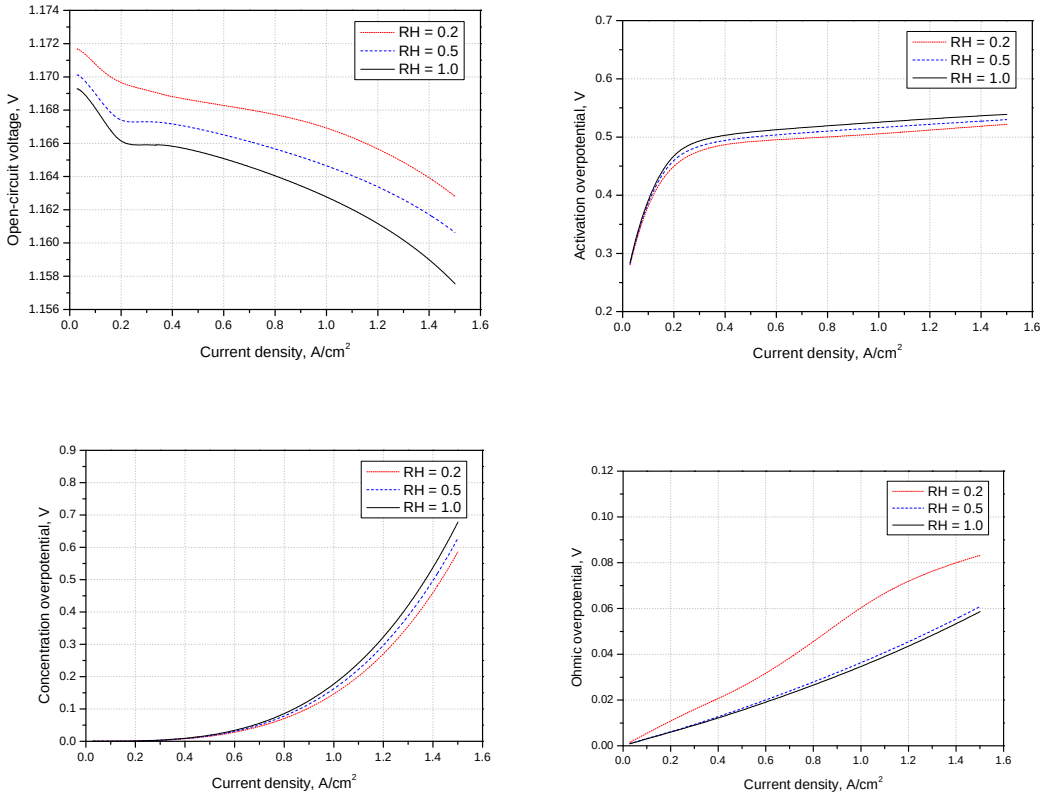

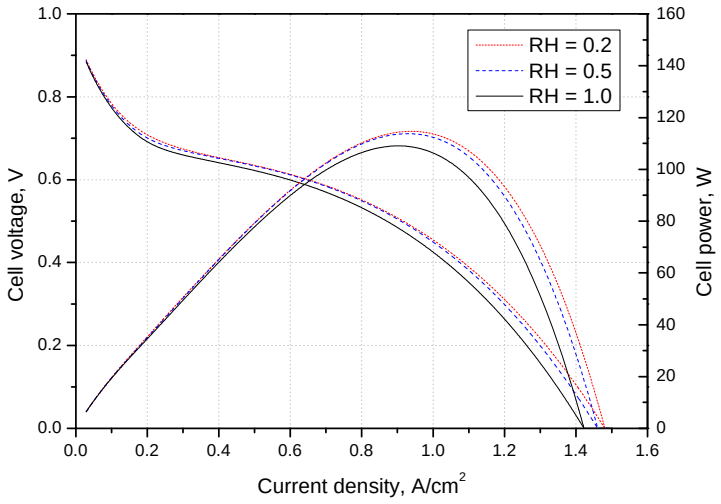


Figure 18 I-V characteristic, power and overpotential for different relative humidity

### 5.1.1.3.4 REACTANT GAS PRESSURE

PEM fuel cells can be operated at low, atmospheric or high, compressed pressure. An increase in pressure is able to improve stack performance, but increases parasitic loss as well because power from the stack is used for the compressors. Therefore, the total benefit from an increase in pressure should be further examined in terms of the total system, B.O.P.

Figure 19 shows the pressure dependent I-V, power, and overpotentials' characteristic curves from the simulation's results at different inlet pressures. When the pressure increases, the cell voltages tended to increase due to the oxygen concentration. Larger oxygen concentration cause decrease in activation overpotential and concentration overpotential. However, higher mass flow rate from the high pressure cause much easier water removal and subsequently, ohmic overpotential increases. However, increase in

ohmic overpotential is less than decrease in activation and concentration overpotential. Therefore, the cell voltage increased.

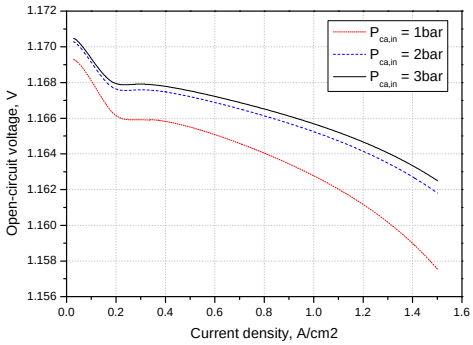


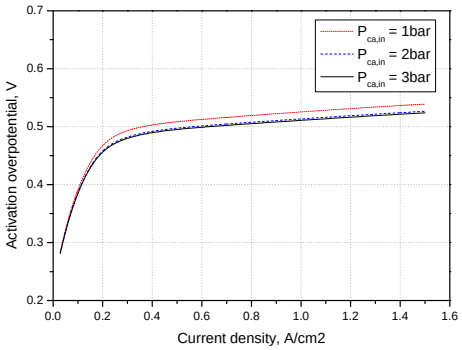


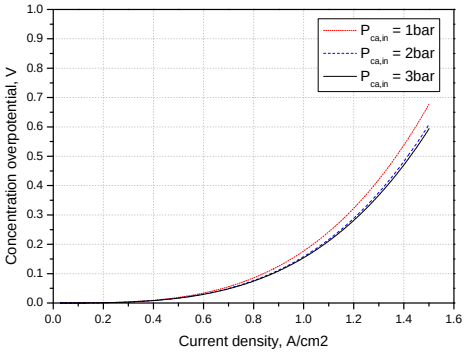


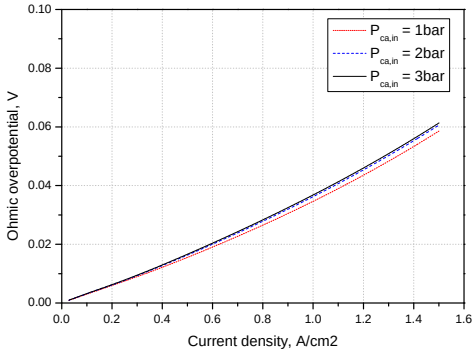


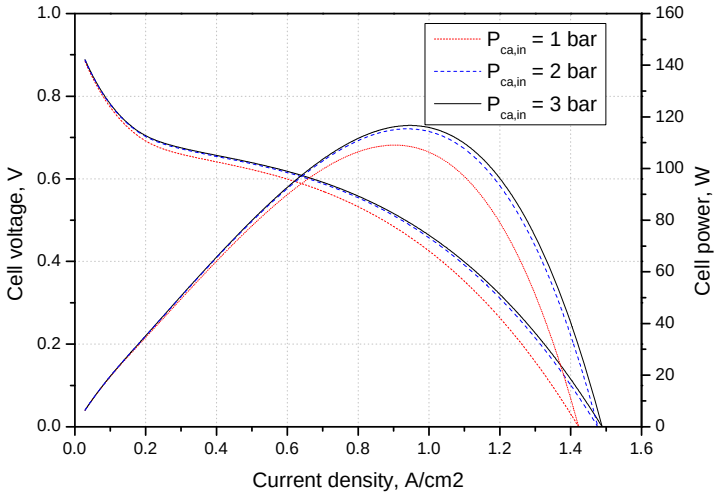

Figure 19 I-V characteristic, power and overpotential for different reactant gas pressure

#### 5.1.1.4 OPTIMIZATION OF OPERATING CONDITION

There are many ways to optimize the design. As seen below, 9 cases are suggested for optimization using the Taguchi method. Figure 20 shows different cell voltages depending upon each of the 9 cases. Using the model and simulations, the 9th case is selected as the best operating condition. The main factor for improving performance is temperature and stoichiometric ratio at the cathode. It causes less activation overpotential at the catalyst layer and ohmic overpotential at the membrane.

| Case | Temperature ($^{o}$C) | Stoichiometric ratio | Relative humidity | Pressure (bar) | Cell power (W) |
|---|---|---|---|---|---|
| 1 | 60 | 1 | 20 | 1 | 76.67 |
| 2 | 60 | 2 | 50 | 2 | 98.33 |
| 3 | 60 | 3 | 100 | 3 | 110 |
| 4 | 70 | 1 | 50 | 3 | 80 |
| 5 | 70 | 2 | 100 | 1 | 98.33 |
| 6 | 70 | 3 | 20 | 2 | 110 |
| 7 | 80 | 1 | 100 | 2 | 80.83 |
| 8 | 80 | 2 | 20 | 3 | 100 |
| 9 | 80 | 3 | 50 | 1 | 111.67 |

Table 2 Three-level orthogonal arrays for 9 different cell operating conditions

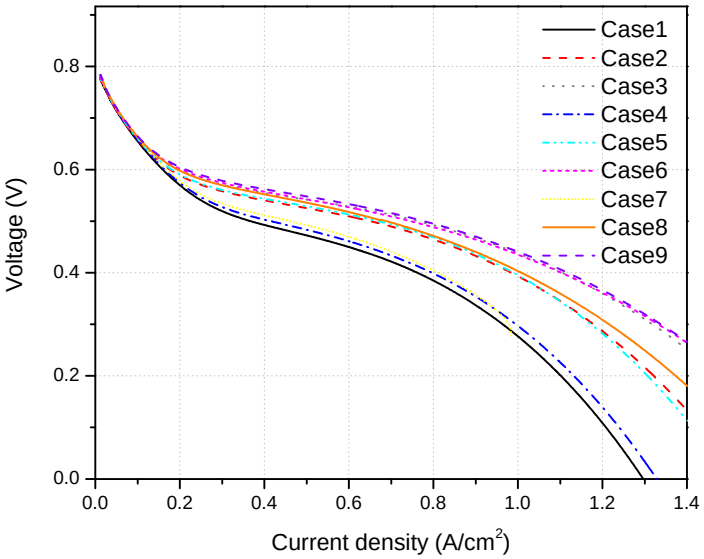


Figure 20 I-V characteristic for 9 different cell operating conditions

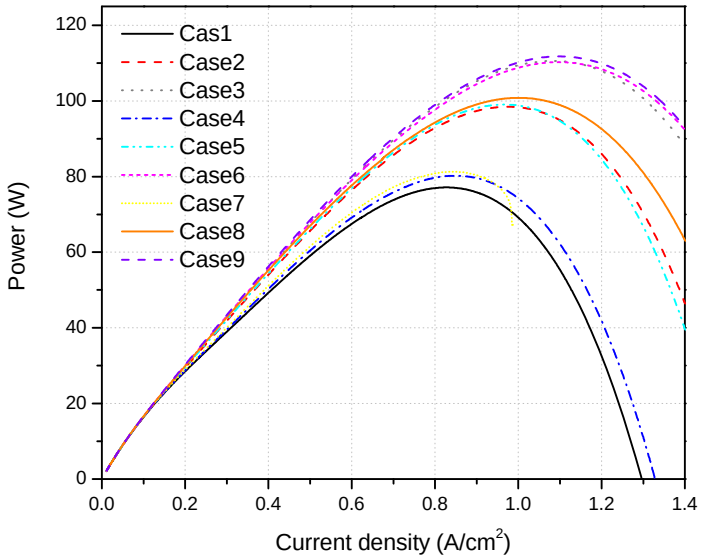


Figure 21 Cell power for 9 different cell operating conditions

#### 5.1.1.5 EFFECTS OF GEOMETRY ON THE PERFORMANCE

In this section, the effects of the porosity and thickness of the GDL, as well as membrane thickness, on the performance were analyzed with the model. Figure 22 shows the effect of thickness change of the cathode GDL during a multi-step current test of 0.4, 0.8 and 1.2 (A $cm^{-2}$).

Figure 22(a) shows effects of the GDL thickness on the cell voltages. When the GDL was thicker, the cell voltage would decrease. As current density increased, the cell voltage decreased more rapidly due to the effect of the increasing GDL thickness.

When the GDL became thicker, the liquid water saturation increased because of elevated resistivity for the water transport [19]. As a result, the water content in the membrane increased as the GDL became thicker because of the increased liquid water saturation, as shown in Figure 22(c). Therefore, the ohmic overpotential decreased. Likewise, the increasing liquid water saturation in the GDL makes the oxygen mass transport harder than before, and the oxygen concentration at the interface between the GDL and the CL decreased. Thus, the activation over-voltages increased as shown in Figure 22(b).

The voltage difference between cell 1 and cell 2 was caused by the decreased ohmic overpotential in cell 2 which was affected by the increased membrane water content. The membrane's water content was influenced by cell 2's operating temperature which in turn also affects the voltage difference.

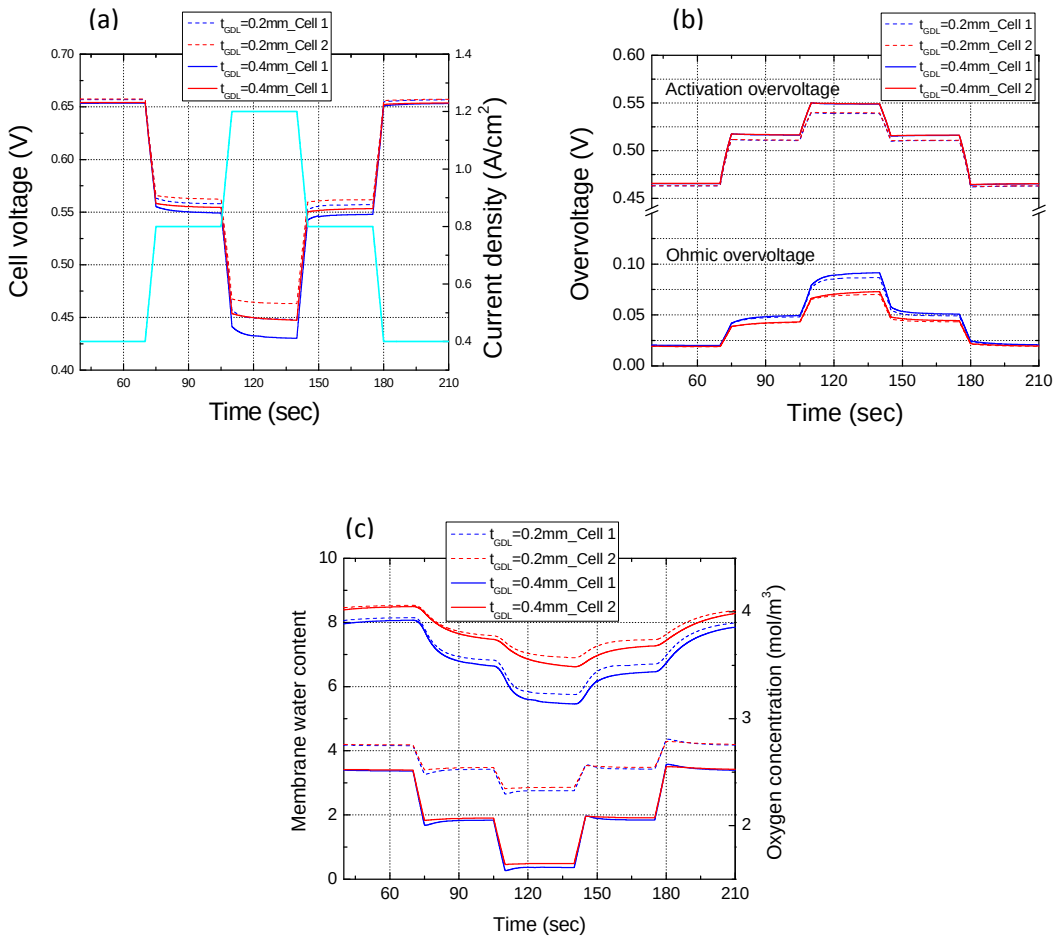


Figure 22 Response of a fuel cell to a multi-step current density at different cathode GDL thicknesses. (a) Cell voltage, (b) Activation and ohmic overpotential and (c) Membrane water content and oxygen concentration near the cathode catalyst layer.

Figure 23 shows the effects of the porosity of the GDL on the cell voltages, membrane water content, and oxygen concentration during a multi-step current test of 0.4, 0.8 and 1.2 (A cm$^{-2}$). Figure 23 (a) shows the effects on the cell voltages. When the porosity became larger, the cell voltages increased because of the smaller pressure drop and high rate of oxygen transport which implies an increase of effective diffusion

coefficient. In particular, the voltages increased at higher currents as the porosity increased because of easier oxygen mass transport when the porosity was larger. As a result, the oxygen concentration at the interface between the GDL and CL increased and the activation overpotential decreased, as shown in Figure 23 (b) and (c). Thus, the cell voltages increased.

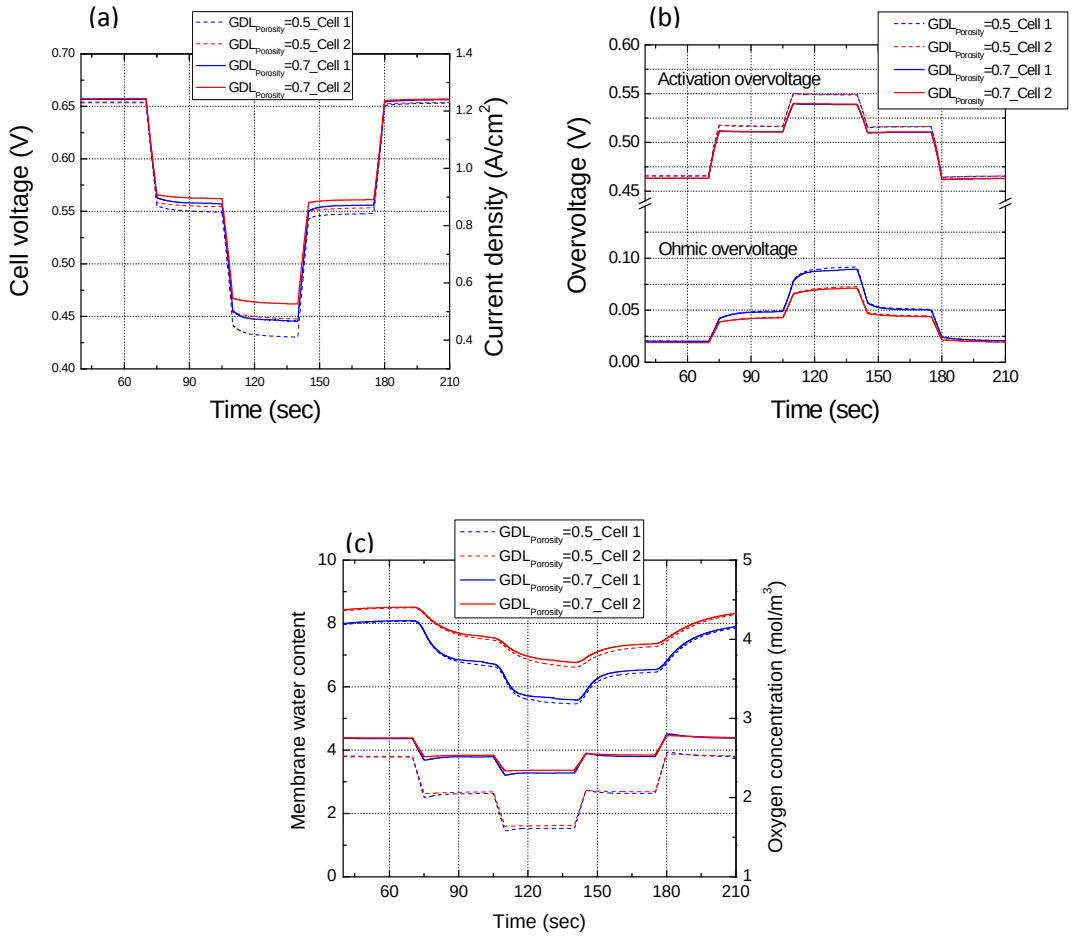


Figure 23 Dynamic responses of the fuel cells to step changes in current density at different cathode GDL porosities. (a) Cell voltage, (b) Activation and ohmic overpotential and (c) Membrane water content and oxygen concentration near by the cathode catalyst layer.

Figure 24 shows the effects of membrane thickness on the cell voltages, membrane water content, and oxygen concentration during a multi-step current of 0.4, 0.8 and 1.2 (A $cm^{-2}$). Figure 24(a) shows the effects of the membrane thickness on the cell voltages. When the membrane thickness increased, cell voltage decreased, and it caused more of an effect on cell voltage with a higher current density.

When the membrane became thicker, there was no change in oxygen concentration or activation over-voltage. However, the water content became smaller and subsequently the ohmic overpotential increased as shown in Figure 24(b) and (c). The rate of the voltage difference between cell 1 and 2 increased as current density increased.

The analysis showed that the thickness of the membrane plays an important role in the improvement of a cell's performance. As the membrane's thickness decreases, the cell's performance increases.

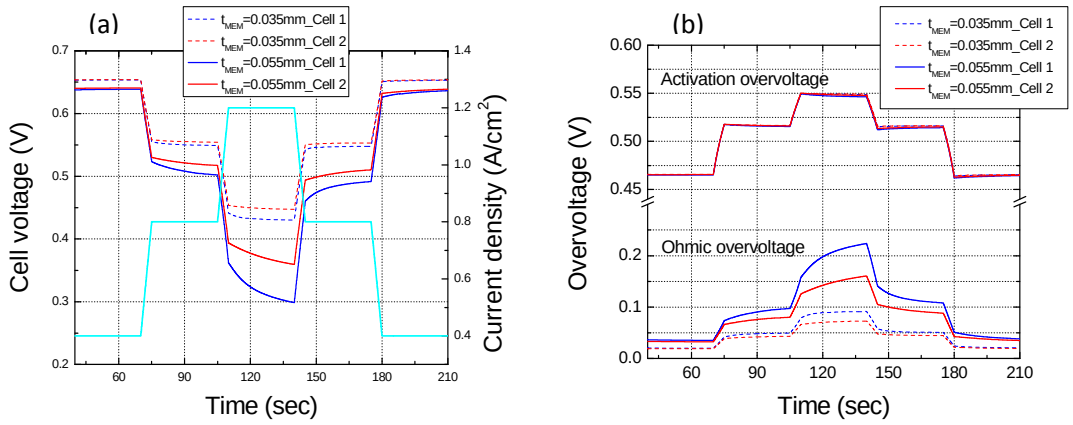

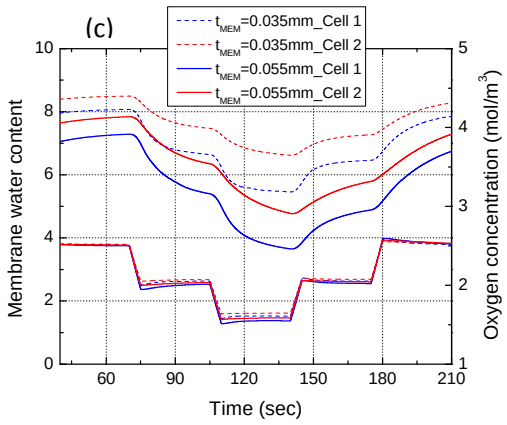


Figure 24 Dynamic responses of the fuel cells during a step change in current density at different membrane thicknesses. (a) Cell voltage, (b) Activation and ohmic overpotential and (c) Membrane water content and oxygen concentration near the cathode catalyst layer.

### 5.1.1.6 OPTIMIZATION OF GEOMETRY PARAMETER

There are many ways to optimize the design. As seen below, 4 cases are suggested for optimization using the Taguchi method. Figure 25 shows different cell voltages depending upon each of the 4 cases. Using the model and simulations, the 1st case is selected as the best geometry condition. The main factor for improving performance is less thickness of GDL which causes decrease in water transportation resistance. The easier water transportation to the membrane causes less activation overpotential at the catalyst layer and ohmic overpotential at the membrane.

| Case | GDL (mm) | GDL porosity | MEM (mm) | Power (W) |
|---|---|---|---|---|
| 1 | 0.2 | 0.5 | 0.035 | 106 |
| 2 | 0.2 | 0.7 | 0.055 | 102 |
| 3 | 0.4 | 0.5 | 0.035 | 99 |

| | | | | |
|---|---|---|---|---|
| 4 | 0.4 | 0.7 | 0.055 | 97 |

Table 3 Two-level orthogonal arrays for 4 different geometry parameters

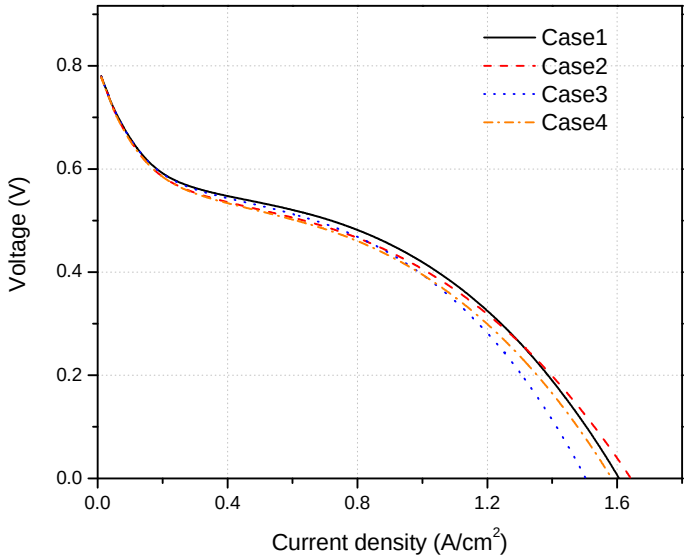


Figure 25 I-V characteristic for 4 different geometry parameters

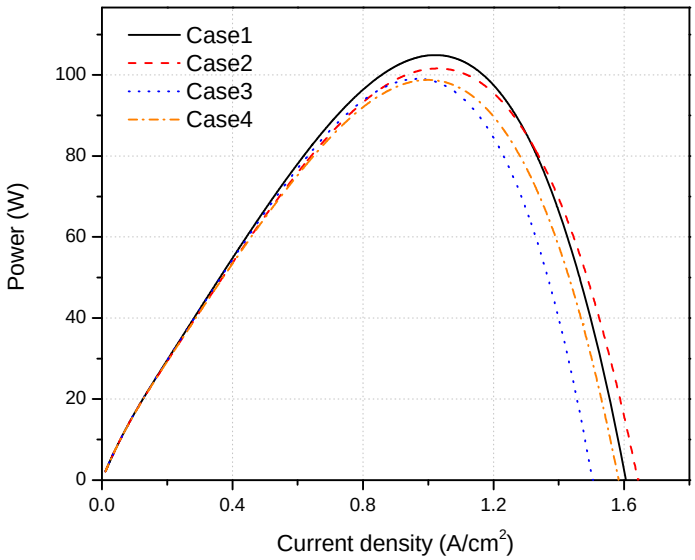


Figure 26 Cell power for 4 different geometry parameters

# 6 STACK DESIGN

Theoretically, the open circuit voltage of a polymer electrolyte membrane fuel cell is 1.23V due to the overpotential. However, real experimental voltage is below 1V. If a single cell which produces 1 kW of power is needed, it should generate slightly over 1000A of current. To do this, the active area should be large enough to generate 1000A. Also, the cables between the fuel cell and the load need to be thick enough in order carry such a high current and to have a very low ohmic resistance. However, the practical solution is to use a multi-cell stack where the cells are connected in series. The active area of single cell and cross-sectional area of cables can be reduced by increasing the number of cells.

## 6.1 QUADRUPED ROBOT SPECIFICATION

The specification for the quadruped robot is based on the walking and transporting mode. It has two modes and each mode needs same amount of power, about 6kW with operation of hydraulic device. The 19Nm maximum motor torque is required at maximum speed (1.5m/s) and 28Nm maximum torque is required during the transporting mode of the robot. Each rotational speed is about 3000 RPM and 2000 RPM.

| Condition | Robot mass | Maximum speed | Required power |
|---|---|---|---|
| Standing up | 80 kg | 0 m/s | 4.67 kW<br>44.6Nm@1000RPM |
| Walking mode I | 80 kg | 1.2 m/s | 8.2 kW<br>31.5Nm@2500RPM |
| Walking mode II | 80 kg | 1.5 m/s | 9.5 kW<br>33.5Nm@2700RPM |
| Transporting mode | 130 kg | 0.7 m/s | 9.5 kW<br>50.2Nm@1800RPM |

Table 4 Operating mode of the quadruped robot

## 6.2 STACK SIZING

The first step for the design of the stack is to determine the active area and the number of cells in the stack. Furthermore, the desired power output, stack voltage, efficiency, and volume and weight limitations are also considered as design requirements. Therefore, these variables need to be optimized while the stack constantly satisfies one major parameter, such as the desired power output. Cell stack performance is affected by the unit cell performance described well by the I-V curve. This is the most important part for multi-cell stack sizing, and it can be varied and optimized depending on the operating conditions, i.e. pressure, temperature, and humidity.

Power output of the stack is calculated by the product of voltage and current.

$$P = V_{stack} \cdot I \tag{6- 1}$$

The total stack voltage is the sum of each unit cell voltage because they are connected in series.

$$V_{stack} = \sum_{i=1}^{n} V_i \tag{6- 2}$$

Current is calculated by a product of current density and active area.

$$I = i \cdot A_{cell} \tag{6- 3}$$

There are additional variables, such as stack volume and stack size, which are determined by the number of cells in the stack and the active area of each cell. Moreover, power output, stack voltage, and stack efficiency can also determine other variables such as the number of cells or active area. If there are unknown values among power output, stack voltage and stack efficiency, then there are infinite options for the stack design.

There are factors that make different combinations of numerous cells and active areas difficult to build. For example, connecting a lot of unit cells which have small active areas are hard to arrange in a line and connect. Connecting unit cells which have larger active areas can also cause problems of uneven distribution of reactant gas concentration, temperature, and pressure on the surface of the catalyst layer's active area. One of the most important factors for design of the fuel cell stack is the even distribution of reactants, concentration, and pressure. A pressure drop which causes uneven distribution should also be fully considered and reduced. Therefore, the final design of the fuel cell stack should be checked whether it satisfies all of the desired requirements and specifications. If not, the number of cells or active area should be changed appropriately to meet the demand.

The operating voltage can be any value as long as it meets the specification of the system. However, the operating voltage should be determined under the consideration of stack size and efficiency. For instance, a fuel cell system operating at a low voltage

makes a higher power output. Thus, as the power density increases, the total stack weight and volume can decrease in size for the same power output. However, its efficiency does not increase but does decrease which means that the intake components, i.e. fuel tank and air blower, should be increased to make up for the poor efficiency in the PEM fuel cell system. Inversely, the stack efficiency can be increased with a higher operating cell voltage as it allows the PEM fuel cell system to minimize fuel consumptions and the size of fuel delivery system. Specifically, in the transportation system, optimizing efficiency plays a pivotal role in reducing the weight and size of the system.

As shown in the Figure 27, the operating cell voltage plays an important role in deciding the power density and efficiency. The Figure 28 shows the cell efficiency which is based on the relationship between lower heating value of a fuel, hydrogen, and the output power. Usually, the power density and the stack efficiency have opposite characteristics at the cell voltage larger than 0.5V. The power density increases while the stack efficiency decreases, and the power density decreases while the stack efficiency increases. The higher operating cell voltage also contributes to make high efficiency and reduce fuel consumption even though its size can be increased. Figure 27 shows that the stack with operating cell voltage at 0.7V has the 100% more size than the stack which is operated at 0.6 V. The stack with operating cell voltage at 0.8V needs also about 4 times more active area than the stack with operating cell voltage at 0.6V. Therefore, there are both of positive and negative effects about increasing the cell voltage and it should be determined based on the priority of the design such as the smallest size or the smallest cost for electric generation.

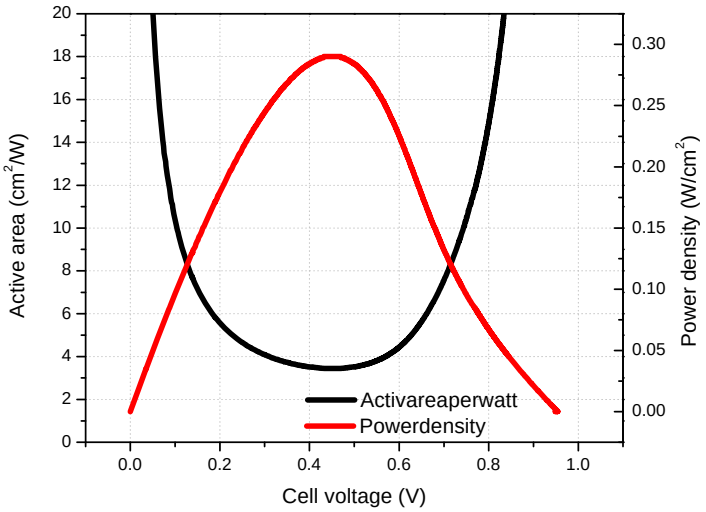


Figure 27 Stack size and operating voltage

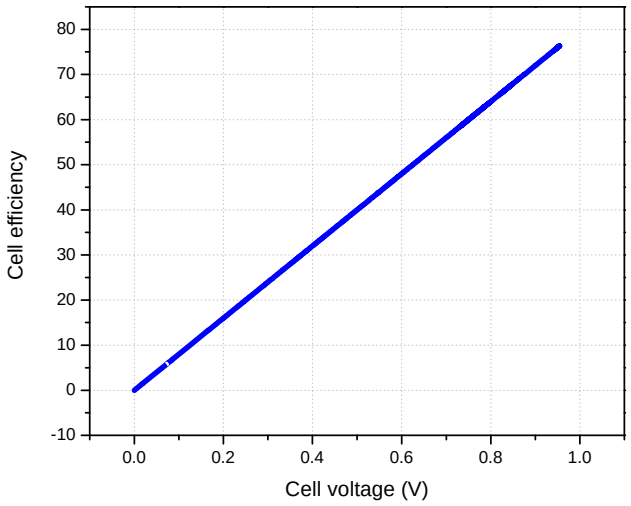


Figure 28 Cell efficiency dependent upon nominal cell potential

Figure 29 shows the cell power, efficiency and current density of the unit cell with the condition that temperature is 353K, RH is 100% and stoichiometric ratio is about 2. The unit cell with the active area, 250 $cm^2$, can make the maximum power, 117 W, at

around 0.5 V with 40% of efficiency. However, the unit cell is able to increase cell efficiency up to 55% at nominal cell potential of 0.7V while its maximum power decreases about 65%. Therefore, with the condition for the optimization that the cell efficiency should be over 45% and the stack should be as small as possible, the operating cell voltages can be determined to be 0.6 volt. It generates 98 W with 48% efficiency to meet both of performance and efficiency specification. Consequently, 100-cell PEM fuel cell system which operates at 0.6 volt to have a 10kW operating power with 50% efficiency is needed.

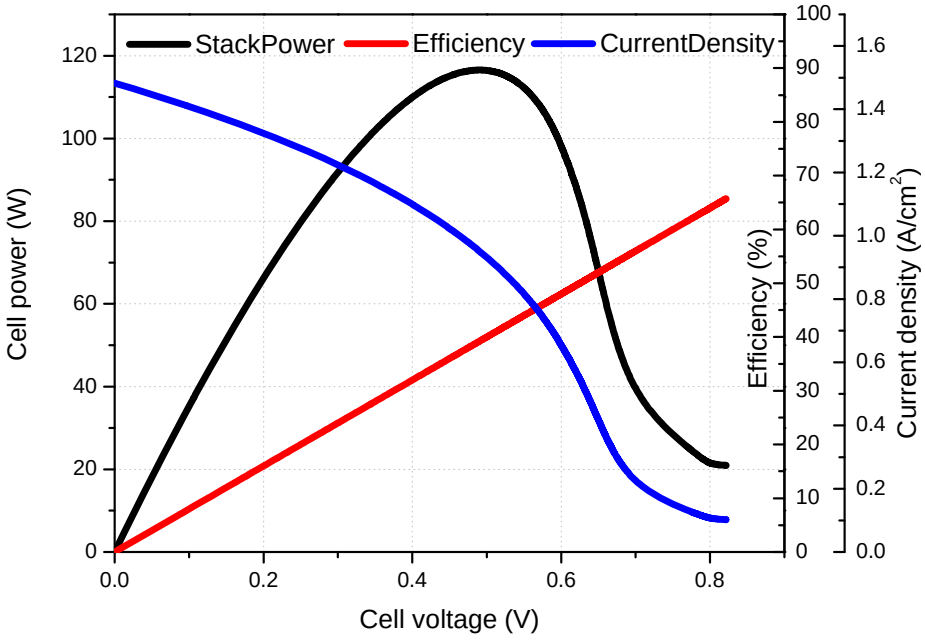


Figure 29 Single cell power, efficiency and current density with selected cell voltage

## 6.3 20-CELL STACK ANALYSIS FOR CELL EXTENSION

The characteristic of the stack should be analyzed before the single cell is expanded to multi cells-stack. Therefore, static behavior and dynamic behavior is analyzed to examine a characteristic of temperature distribution within the 20-cell stack.

### 6.3.1 STACK BEHAVIOR

First of all, the model was used to analyze the temperature difference under constant load current density. Figure 31 shows the simulated results of the voltage gradient at constant load current density. It is noted that there is small voltage gradient through the stack. It also shows that there is some voltage difference between right end cell and left end cell due to the effect of temperature difference. However, in real stack, there is much more voltage difference between individual cells [20].

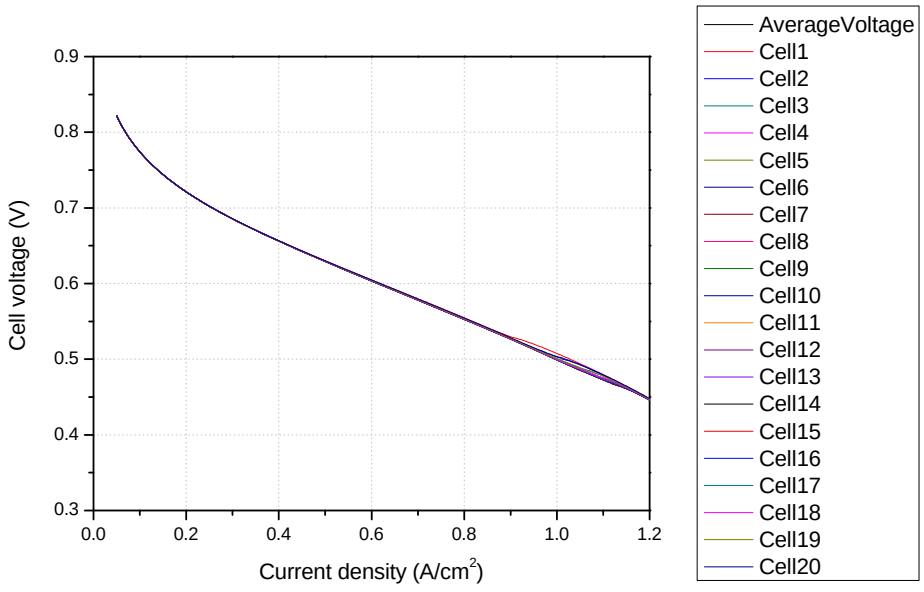


Figure 30 I-V polarization curve of the 20 cell stack

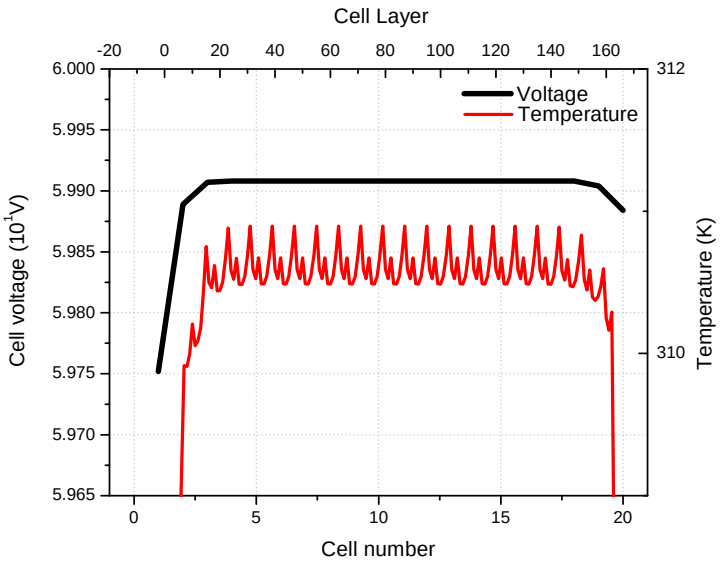


Figure 31 Voltage distribution under the constant current density, 0.6 (A $cm^{-2}$) at 2sec

Figure 32 shows the temperature gradient in the stack at the given current density. The peak temperature is observed at the catalyst layer because heat is released at the membrane due to the ohmic resistance and at the catalyst layer during chemical reaction with the entropy increase. In contrast, the energy loss from the entropy change which causes heat generation during the reaction at the anode catalyst layer is negligible. Moreover, each catalyst layer exist around membrane at the anodic side and cathode side which make temperature difference between right end and left end cell due to asymmetrical heat source distribution in the stack [6] [18][25].

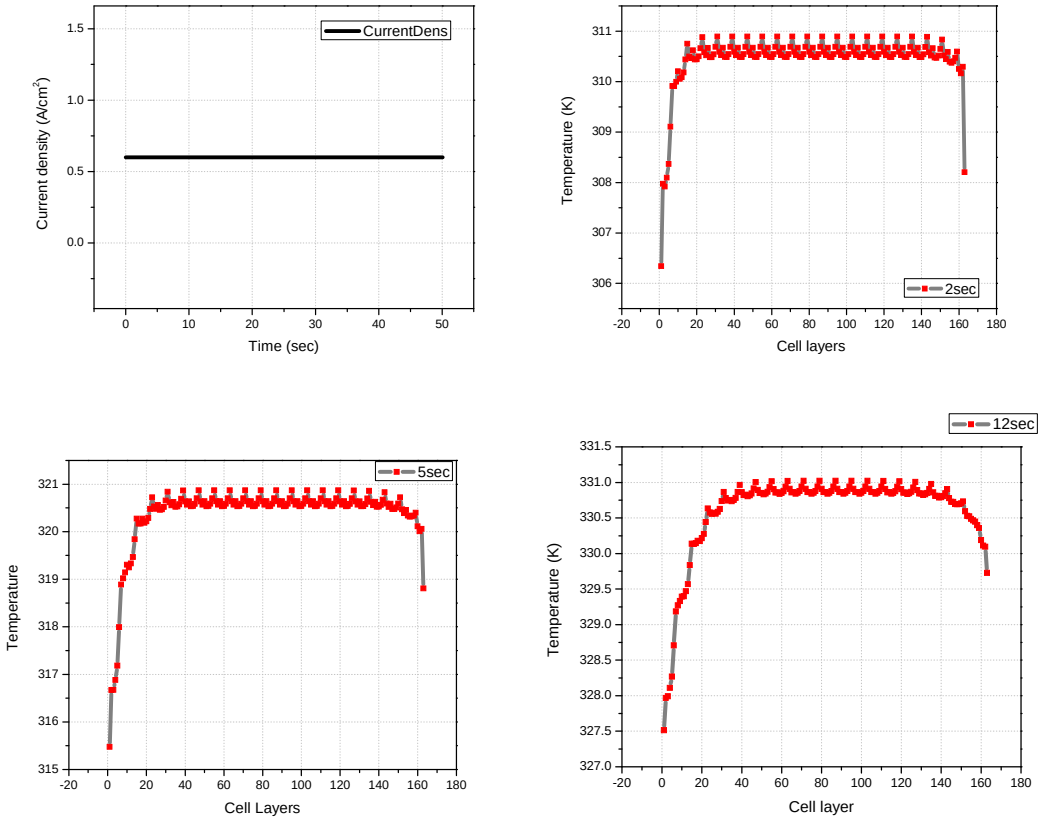


Figure 32 Temperature distribution under the constant current density 0.6 (A $cm^{-2}$)

Heat generated from the end cell is transferred to the end plate because of the temperature difference between the cell and the endplate which is contact with ambient air. Therefore, generated heat from the end cell is not stored in the cell but transferred to the end plate assembly. However, the each cathode catalyst layer is located at the right side of the membrane assembly in the model. For instance, the cathode catalyst layer of the cell 1 is located after 5 layers, coolant channel, gas channel, gas diffusion layer, anode catalyst layer and membrane, from the left end plate assembly while there are just 3 layers between the cathode catalyst layer of the cell 10 and the end plate assembly. It causes distribution of heat source to be asymmetrical. Therefore, the amount heat transfer

from the cathode catalyst layer of the cell 10 to the end plate is much larger and it causes the right end plate temperature higher than left end plate and temperature gradient in the right side relatively smaller than left side. Consequently, overall heat transfer rate at the right half side of the stack becomes smaller and it causes to keep the heat and average temperature of right half side becomes higher than left side. All in all, heat transfer rate from the effect of asymmetrical heat source distribution make asymmetrical temperature difference.

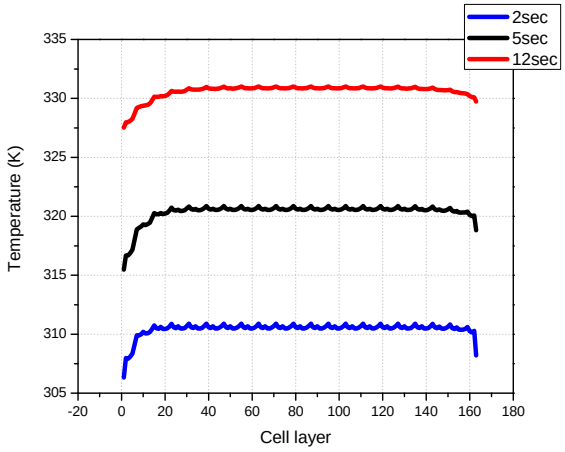


Figure 33 Temperature changes during operation with constant current density

### 6.3.2 DYNAMIC BEHAVIOR

Figure 34 shows the current load, the transient behavior of the temperature for the each cell which constitutes the stack during the start-up with increasing current load from 0.1 to 1.5 for 90 seconds. With given operating condition that cell initial temperature is 298K, relative humidity at the cathode is 70% and anode is 50%, and the stoichiometric

ratio of air is 2 and fuel is 1, it took more than one minute for the cathode catalyst layer of the cell 1 (which has lowest temperature) to reach the desired working temperature.

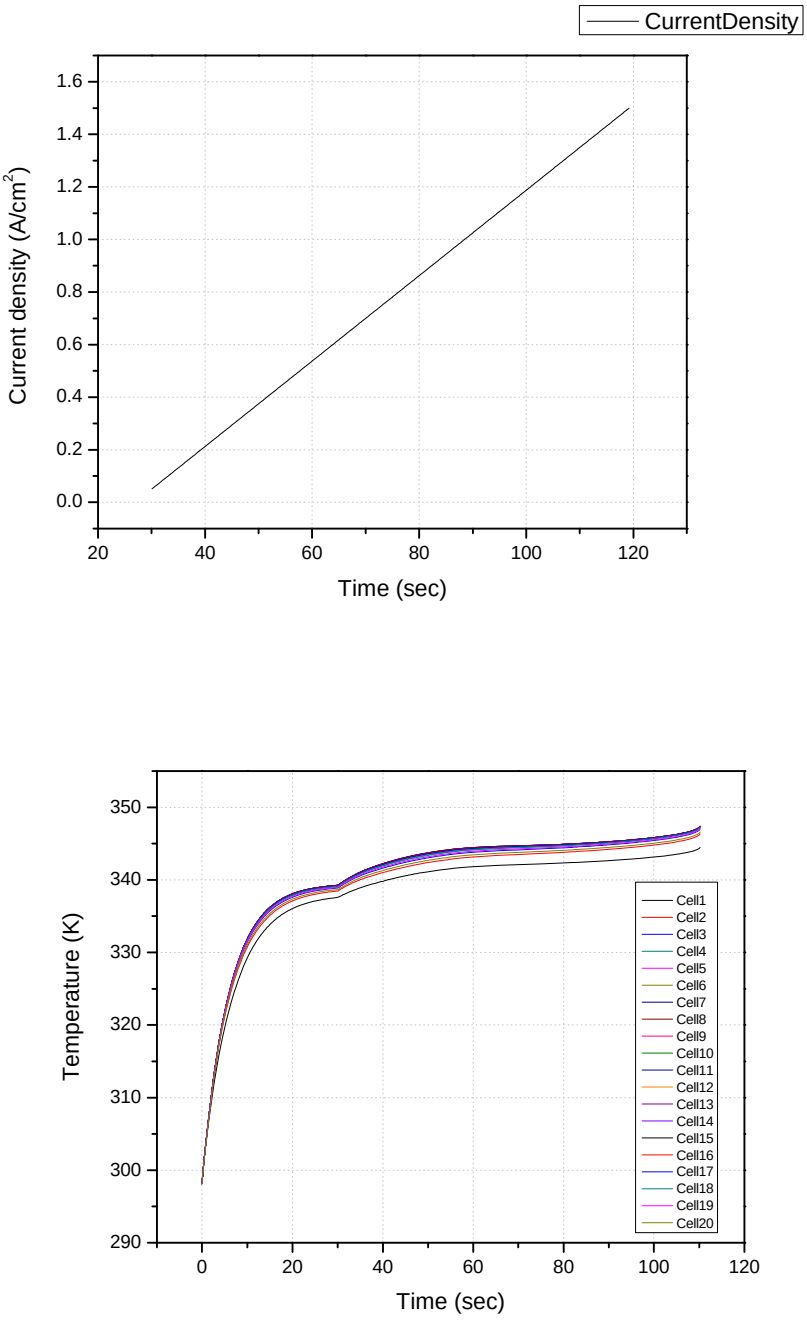


Figure 34 Temperature changes during the start-up

Figure 35 shows the temperature gradient in the stack during the start-up. As shown before, the peak temperature is observed at the catalyst layer at which chemical reaction occurs and release heat from the entropy increase, while the energy loss at the anode catalyst layer with the increase in entropy is negligible. There is also temperature difference between right end and left end cell due to asymmetrical heat source distribution in the stack which is described in the previous chapter.

At 60sec, released heat from the cathode catalyst layer increases temperature of the cathode catalyst layer and makes peak temperature. The maximum temperature difference between the coolant channel and the cathode catalyst area is about 2K at the cell 1. It is almost same as the temperature difference between the cell 1 which has lowest temperature and the cell 10 which has usually highest temperature. Furthermore, there is temperature gradient from the end plate to the 5cells at the both cathode and anode side while inner 10 cells showed relatively uniform temperature distribution.

At 120 sec, there is still peak temperature at the catalyst layer of the unit cell. As current density increases, the larger temperature difference between the catalyst layer and the coolant channel at the unit cell is observed. The peak temperature has usually more than 2K higher temperature than the coolant channel at a current density 1.45 (A $cm^{-2}$). Furthermore, temperature difference between cell 1 and cell 20 was about 2K which is 1K larger than the one at 60.

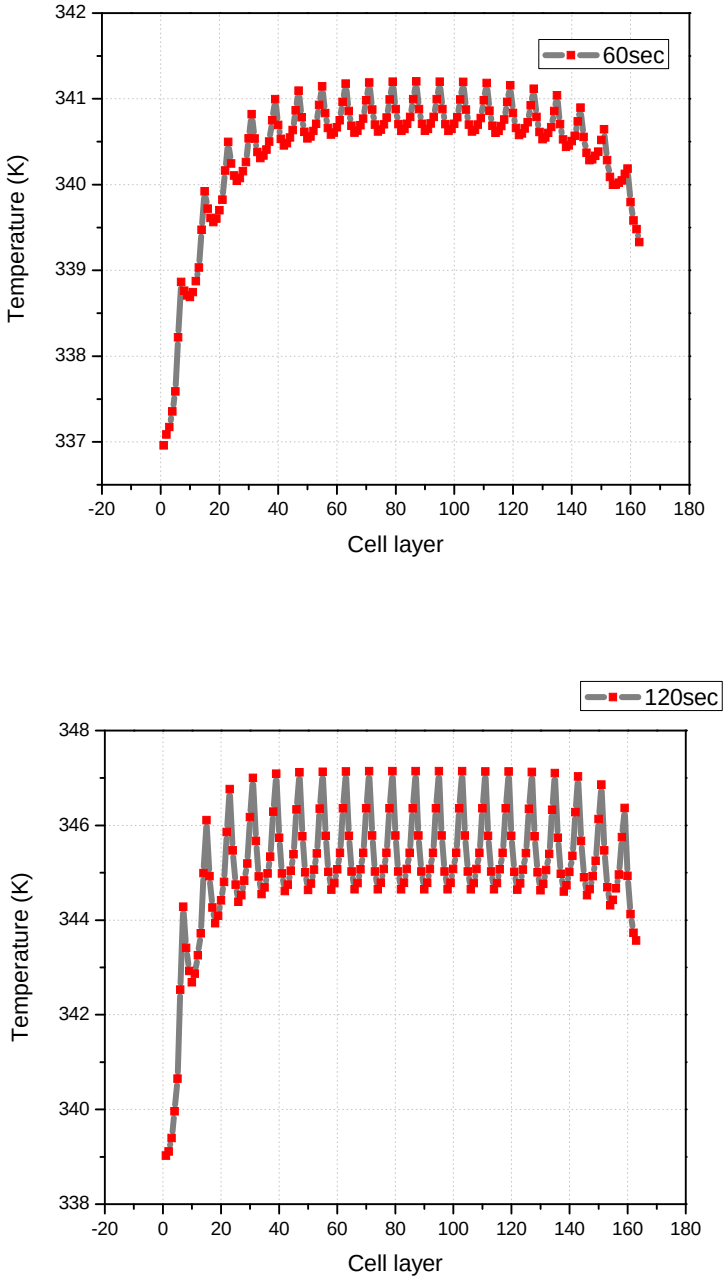


Figure 35 Temperature distribution during the start-up

However, the voltage difference from the different temperature is not significant. Figure 36 shows the change in cell voltage during the start-up at the current density 0.4, 0.8 and 1.2 (A $cm^{-2}$). From the simulation, it is shown that excessively high current loads cause large temperature gradient from the end plate to the cell 5 at the cathode and anode side of the stack and disturb uniform temperature distribution which can improve the performance of the stack. Therefore, operating cell voltage should be optimized to realize uniform temperature distribution through the stack [6]. Furthermore, asymmetrical temperature distribution also should be improved to reduce the difference in heat transfer rate at the end cell by using different coolant flow rate or end plate designed for each cell.

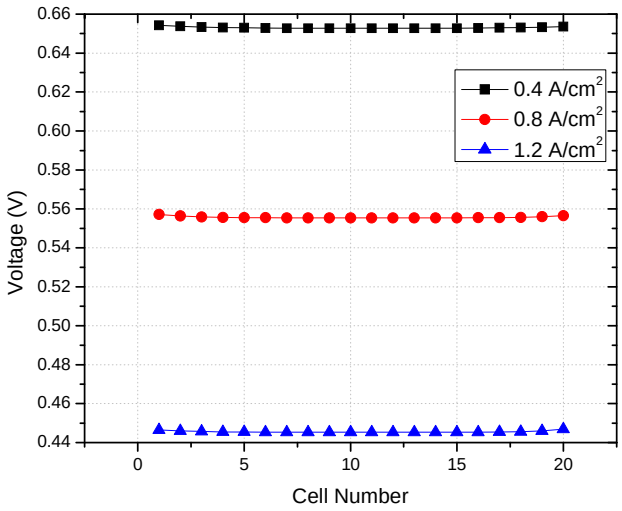


Figure 36 Voltage changes during the start-up

Figure 37 shows the average temperature difference percentage of the unit cell in the stack during the start-up. From the simulation, there is large temperature gradient at both of the end side in percentage terms. There is more than 5% temperature difference

percentage from the 1st cell to the 5th cell and from 17th cell to the 20th cell. Other than the cells, the temperature difference between cells can be neglected.

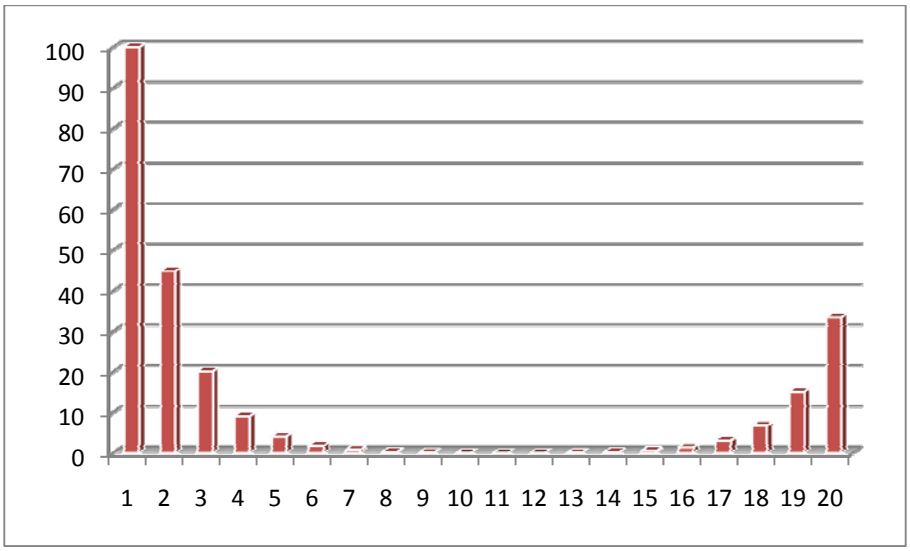


Figure 37 Temperature difference

## 6.4 100-CELL STACK

### 6.4.1 MODEL DESCRIPTION

Based on those results above, a model for the 100-cell stack was constructed and its performance was analyzed. The analysis showed that temperature distribution in the stack significantly influenced chemical reactions, phase change between water vapor and liquid water, partial pressure and water content in the membranes. However, performance of the individual cells was dependent upon the location of cells. The cells located in the middle of the stack have not shown any significant gradients of activation as well as ohmic over-potentials, partial pressure of the reactants and concentration of water vapor

and liquid water. Conversely, the outer 5 cells at the cathode and anode side are strongly affected by the temperature and showed different performance characteristics from those of the middle cells. Maximum voltage difference between the individual cell in the end cells and the middle cells was 0.02V at 0.7 (A $cm^{-2}$).

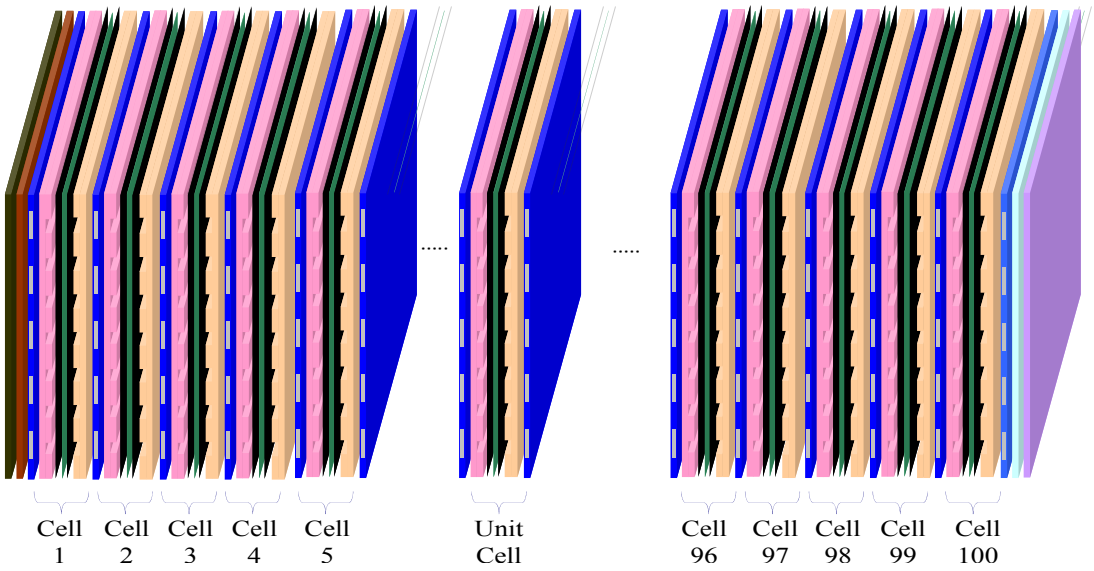


Figure 38 A schematic diagram of the 100 cell stack

| | **Materials** | **Thickness (m)** | **Thermal conductivity (W $m^{-1}$ $K^{-1}$)** | **Density (kg $m^{-3}$)** | **Specific heat (J $kg^{-1}$ $K^{-1}$)** |
|---|---|---|---|---|---|
| End plate | G-10 Garolite | 0.028575 | 0.288 | 1800 | 1416 |
| Bus plate | Stainless steels AISI316 | 0.001524 | 13.4 | 8238 | 468 |
| Coolant plate | AXF-5Q-PYC graphite | 0.001524 | 95 | 1780 | 935 |
| Gas channel plate | TM graphite | 0.001524 | 105 | 1820 | 935 |
| Diffusion media | ELAT v3.0 | 0.0002064 | 65 | 558 | 840 |
| Catalyst layer | Platinum | 0.0000035 | 0.2 | 387 | 770 |
| Membrane | 5510 MEA | 0.000028 | 0.21 | 1967 | 1100 |

Table 5 Geometric parameters and materials for the design

Consequently, a high power stack composed of a high number of cells should be constructed considering those end cells. The rest of cells can be assumed to be located in the middle of the stack, which can be simply built by a multiplication of the needed number of cells with a single cell input and outputs. For building a 100-cell stack, two five end cells at each end can be connected to a single cell multiplied with 90, called as a stack with a single and multi cells (SSMC). A schematic diagram for the 100-cell stack is shown in Figure 38 and Figure 39. Each cell is connected considering temperature interaction in series. Reactants flow and chemical reaction has their own characteristic and values without interaction with each unit cells, but temperature of the each cell is affected by the connection of the cells.

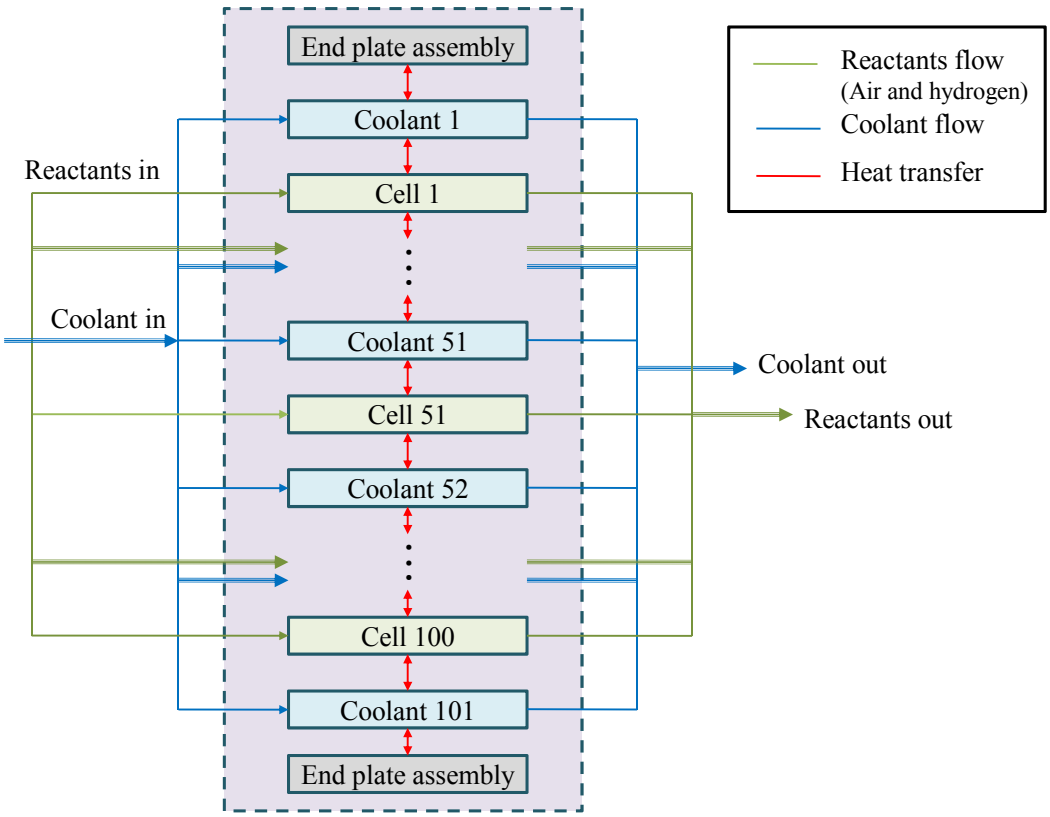


Figure 39 100-cell stack block diagram

## 6.5 DESIGN OF THE AIR PROCESSING SYSTEM

### 6.5.1 SPECIFICATION OF THE AIR PROCESSING SYSTEM

There are requirements for each subsystem in order to achieve a desired performance. For this fuel cell system, a maximum power of 10.8 kW watts at 233 A and 46.4V is needed using a 100 fuel cell stack with an active area of 250 $cm^2$. Design of the blower size and type should be performed carefully because the fuel cell stack receives the correct amount of air supply such that the stack can perform at the desired power.

First of all, it is needed to estimate how much air should supply the fuel cell stack for proper operation.

$$\begin{aligned}
\dot{N}_{oxygen} &= n_{cell}\frac{I}{4F} = 100\frac{233}{4\times 96485} = 0.0604\ (mol\,s^{-1}\,m^{-3}) \\
\dot{m}_{oxygen} &= 0.0604\times 32 = 1.93\ (g\,s^{-1}) \\
\dot{V}_{oxygen} &= 0.0604\times 22.4 = 1.35\ (l\,s^{-1})
\end{aligned} \tag{6- 4}$$

Furthermore, the air is composed of 79% oxygen and 21% nitrogen.

$$\begin{aligned}
\dot{N}_{air} &= \dot{N}_{oxygen} + \dot{N}_{nitrogen} = 0.0604 + 0.0604\times\frac{0.79}{0.21} = 0.288\ (mol\,s^{-1}\,m^{-3}) \\
\dot{V}_{air} &= 0.288\times 22.4 = 6.44\ (l\,s^{-1}) = 13.7\,(cfm) \\
\dot{m}_{air} &= 0.00644\ (m^3\,s^{-1})\times 1.184\ (kg\,m^{-3}) = 7.62\times 10^{-3}\ (kg\,s^{-1})
\end{aligned} \tag{6- 5}$$

Pressure drop occurs during operation within the gas channel is the function of the friction factor and consumption rate of the reactants.

$$\Delta p_{ca} = f(f_{friction}(\dot{m}_{ca}), \dot{m}_{consumed}) \tag{6- 6}$$

For the internal flow in the gas channel, pressure drop is defined as follows with consideration of friction factor for the developed steady laminar flow in the channel, Reynolds number which is relationship between inertial force and viscosity, velocity, hydraulic diameter and cross area of gas channel [21].

$$\begin{aligned} &\Delta p = f\frac{L}{D_h}\frac{\rho v^2}{2}, where \;\; f = \frac{56.91}{\mathrm{Re}_{D_h}} \\ &\mathrm{Re}_{D_h} = \frac{\rho V D_h}{\mu} \end{aligned} \tag{6- 7}$$

where $\rho$ is the density of the reactants (kg $m^{-3}$) and $\mu$ is the viscosity of the reactants (kg $m^{-1}$ $s^{-1}$).

Mass averaged velocity, hydraulic diameter and cross area for the gas channel is calculated as shown below [21].

$$\begin{aligned} &v = \frac{\dot{m}}{\rho A_c} \\ &D_h = \frac{4A_c}{P} \\ &A_c = ab \;\; and \;\; P = 2(a+b) \end{aligned} \tag{6- 8}$$

where $\dot{m}$ is the mass flow of the reactants (kg $s^{-1}$), $a$ and $b$ is each length of the channel side (m).

Once cross area of the gas channel is the square and hydraulic diameter is calculated, total pressure drop from the friction can be obtained.

$$\Delta p = 28.455\left(\frac{\mu \dot{m}}{\rho}\right)\left(\frac{L}{a^4}\right) \tag{6- 9}$$

The pressure drop for the reactants which is consumed at the catalyst layer during the chemical reaction is as follows

$$\begin{aligned}\Delta p_{O_2 \text{ by reaction}} &= \frac{\Delta m RT}{V} = \frac{M \Delta N RT}{V} \\ &= \frac{M \dot{N}_{O_2 \text{ consumed}} \Delta t RT}{V} = \frac{iA}{n_{O_2} F}\frac{M \Delta t RT}{V} \\ &= 1.93 \times 10^{-3} \frac{RT}{V}\frac{L}{v}\end{aligned} \tag{6- 10}$$

Therefore, total pressure drop is obtained with consideration air and nitrogen which constitute air.

$$\begin{aligned}\Delta p_{air} &= \Delta p_{O_2} + \Delta p_{N_2} = \Delta p_{O_2 \text{ by reaction}} + \Delta p_{O_2 \text{ along the channel}} + \Delta p_{N_2} \\ &= 1.93 \times 10^{-3} \frac{RT}{V}\frac{L}{v} + 28.455\left[\left(\frac{\mu_{O_2} \dot{m}_{O_2}}{\rho_{O_2}}\right) + \left(\frac{\mu_{N_2} \dot{m}_{N_2}}{\rho_{N_2}}\right)\right]\left(\frac{L}{a^4}\right)\end{aligned} \tag{6- 11}$$

## 6.5.2 DESIGN OF THE BLOWER

A selected blower is required to have a capacity which satisfies both the mass flow rate and the pressure drop for the desired maximum operating condition. However, different blowers that supply the same mass flow rate provide different pressure rises. This means that careful selection or design of a specific blower for this fuel cell system is needed.

There are many kinds of blowers. An axial flow blower and a centrifugal blower are the most common. An axial flow blower is proper when much air flow is needed with low pressure. However, a high pressure axial flow blower with good efficiency has been

developed recently. According to affinity laws, as impeller diameter increases, air volumetric flow rate increases. Also, an increase in fan speed increases static pressure. This static pressure increase is relatively greater than the increase of the air volumetric flow rate. Therefore, fan engineers usually design a centrifugal fan with a small wheel diameter and a high rpm for a pressure blower and an axial flow fan with a large wheel diameter and a low rpm for a volume blower. Fan type can be determined considering Ns, specific speed.

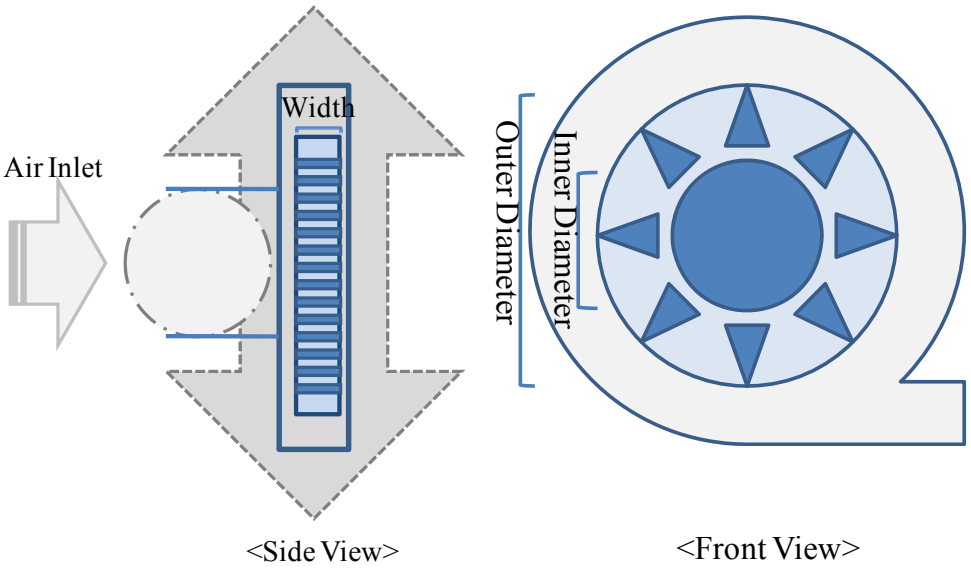


Figure 40 A schematic diagram of blower

### 6.5.2.1 SPECIFIC SPEED

The specific speed is constant as long as the fan has geometric similarity and its speed remains constant. This is useful for selecting the proper type of pump. For example, the specific speed is the speed of any impeller which might be different in size but similar

in shape as it delivers 1 cfm and 1 inWC static pressure. It is not related to the scale of the blower but by the type and structure of the blower [22].

$$N_s = N\frac{\sqrt{\dot{m}_{cfm}}}{P_{static}} \tag{6- 12}$$

The magnitude of $N_s$ varies from 1,000 to 500,000. When it is a small value, it is able to boost a large air volume, and when it is a large value, it is able to create a high pressure.

### 6.5.2.2 TOTAL PRESSURE

Static pressure is the pressure which affects the boundary parallel with fluid flow. It is usually measured at a hole of the surface which is perpendicular to the surface. Total pressure is defined as the sum of static pressure and dynamic pressure [22].

$$\begin{aligned} P_t &= P_s + P_d \\ P_d &= \frac{1}{2}\rho v^2 \end{aligned} \tag{6- 13}$$

In a fuel cell system, pressure drop occurs from friction within the gas channel, thus supplying appropriate air pressure into the gas channel is pivotal for the air supply.

### 6.5.2.3 AIR BRAKE POWER

Total air brake power is calculated by considering air flow rate, $\dot{m}$, and total pressure, $P_t$ [22].

$$L_a = \frac{\dot{m} \times P_t}{102 \times 60} = \frac{\dot{m} \times P_t}{6120}(kW) = \frac{\dot{m} \times P_t}{75 \times 60} = \frac{\dot{m} \times P_t}{4500}(PS) = 0.056(PS) \tag{6- 14}$$

### 6.5.2.4 SHAFT HORSEPOWER

When the fan rotates, the power which is applied to the shaft is shaft horsepower [22], HP.

$$L_s = \frac{\dot{m} \times P_t}{4500 \times \eta}(PS) = 0.09(PS) \tag{6- 15}$$

where $\eta$ is efficiency.

### 6.5.2.5 SHAFT DIAMETER

The moment applied to the shaft, angular speed and shaft horse power has a relationship as below [23].

$$\begin{aligned} L_s &= \frac{T}{75}\omega = \frac{T}{75}\frac{2\pi N}{60} = \frac{TN}{716.2}(PS) \\ d &= c\sqrt[3]{\frac{16T}{\pi\sigma}} = 0.73(cm) \end{aligned} \tag{6- 16}$$

where $T$ is a twisting moment(kg $m^{-1}$), $N$ is a rotation speed (rpm), $c$ is a safety factor and $\sigma$ is allowable twisting stress of the shaft.

The requirement for the air flow rate is 32 cfm of air and 19 in WC at 280 A. Therefore, fan horsepower required is 0.096 hp and shaft load will be 0.15 hp, if fan efficiency is about 65%. Therefore, the total motor load will be 0.18 hp with a 20% mechanical loss.

### 6.5.2.6 OUTSIDE DIAMETER

Outside diameter of the fan could be calculated using the equation below with specific speed [23].

$$D_o = \frac{60K_u\sqrt{\frac{2gP_t}{\gamma}}}{\pi N} = 0.15(m) \tag{6- 17}$$

where $P_t$ is total pressure ($kg_f\ m^{-2}$), $\gamma$ is specific mass of gas ($kg_f\ m^{-3}$), $g$ is gravitational acceleration ($m\ s^{-2}$) and N is speed (rpm).

### 6.5.2.7 INDISE DIAMETER

From the relationship between outside diameter and inside diameter with given specific speed [23],

$$\frac{D_i}{D_o} = 0.3 \tag{6- 18}$$

Hence, inside diameter is 0.045(m).

### 6.5.2.8 NUMBER OF BLADES, Z

The number of blades is calculated with relationship between outside and inside diameter as follows [23].

$$z = \frac{4\pi \sin\beta_2}{1.5\left(1-\frac{D_i}{D_o}\right)} \cong 8.5\frac{\sin 90°}{1-\frac{D_i}{D_o}} = 12 \tag{6- 19}$$

### 6.5.2.9 WIDTH

$$\frac{\pi}{4}D_i^2 = \pi D_i b_1$$
$$b_1 = 0.25D_i = 0.25\times 0.045 = 0.0113(m) = 11.3(mm) \tag{6- 20}$$

Generally, 0.3~0.4$D_1$ is acceptable, thus $b_1$ is14 mm [23].

### 6.5.3 PARAMETRIC STUDY

#### 6.5.3.1 INFLUENCE OF GEOMETRY PARAMETERS

Three designs of blower is compared in terms of flow rate and head loss with a condition that outside diameter is changed and the shape of blower and inside diameter are maintained. The difference in pressure, flow rate and horsepower is recognized in the following.

| **Specification** | **Design 1** | **Design 2** | **Design 3** |
|---|---|---|---|
| $N_s$(rpm) | 33.34 | 76.67 | 153.3 |
| Efficiency | 0.48 | 0.62 | 0.65 |
| Diameter of shaft (m) | 1.018 | 0.742 | 0.0580 |
| Wheel diameter (m) | 0.2865 | 0.1450 | 0.0742 |
| Inside diameter (m) | 0205 | 0.104 | 0.0532 |

Table 6 Design parameter for the blower

As wheel diameter is increased, overall power is also increased at the same RPM while its overall efficiency decreases. Larger wheel diameter is appropriate for large flow rate and head loss for air supply system. Therefore, the RPM of the blower can be changed while maintaining the same mass flow rate based on the results. Smaller wheel

diameter has less power consumption and slightly better efficiency, but increase in efficiency does not increase significantly when the wheel diameter is less than 0.14m.

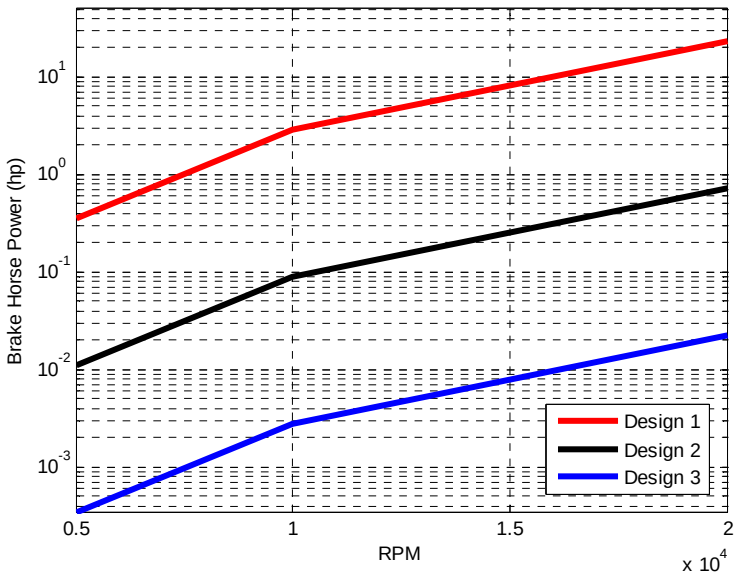


Figure 41 Brake horse power for a different wheel diameter

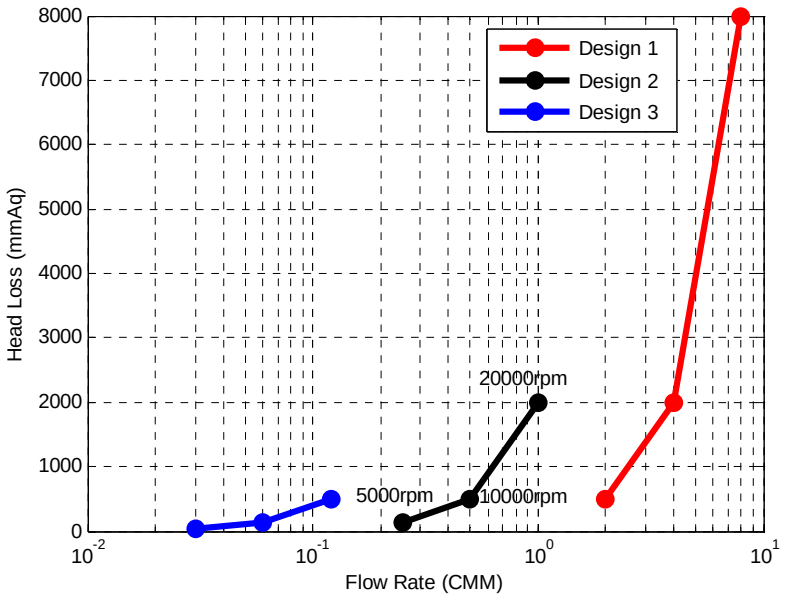


Figure 42 Head loss for a different wheel diameter

The hub-tip ratio is defined as the inner diameter divided by the outer diameter. As inner diameter increases, total pressure can increase much, while flow rate is maintained at the same amount. When inner diameter is changed and the outer diameter and structure of the blower are fixed, the difference in the head loss is as follows.

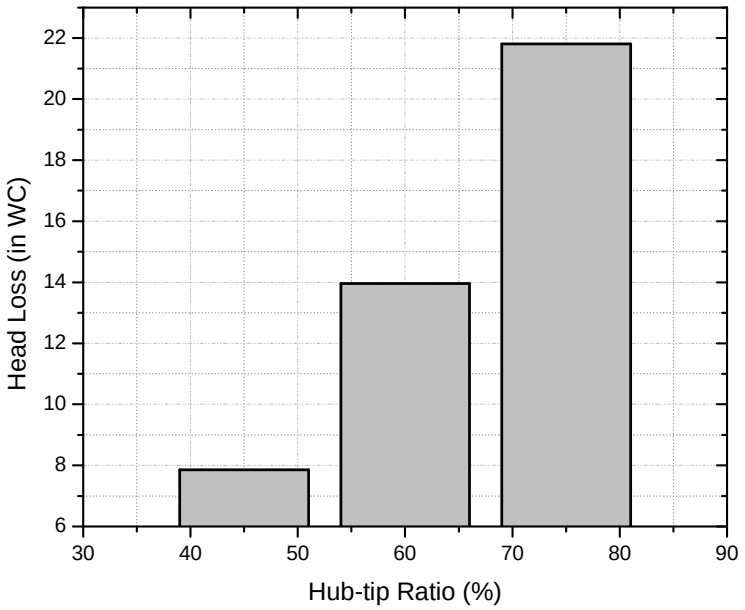


Figure 43 Head loss for a same mass flow rate with different hub-tip ratio

## 6.6 DESIGN OF HEAT EXCHANGER

| **Operating conditions** | |
|---|---|
| Max heat generated | 22.41 kW |
| Air inlet temperature | $40^{o}C$ =313.15K ≅300K |
| Water inlet temperature | $90^{o}C$ =363.15≅365K |
| Air inlet speed | 10 km $h^{-1}$ = 2.78m $s^{-1}$ |

Table 7 Operating condition for the heat exchanger

Air inlet temperature is set to be 300K because the quadruped robot system traditionally operates under this condition. Furthermore, the PEM fuel cell stack should y not be operated over 85$^{o}$C to prevent any degradations. Air flow inlet speed is assumed to be 10 (km $h^{-1}$) because the quadruped robot's speed is 10 (km $h^{-1}$) during normal operation. Other properties related to the heat exchanger are as follows [24]:

| **Type** | **CF-7.0-5/8 J (External air cooling type)** |
|---|---|
| Tube outside diameter | 16.4 mm =1.64 cm |
| Fin pitch | 275 / m =2.75 / cm |
| Fin thickness | 0.0254 cm =0.254mm |
| Free flow area / frontal area | 0.449 |
| Heat transfer area / Total volume | $\alpha$= 269 $m^{-1}$ |
| Fin area / Total area | $A_f/A$= 0.830 |
| Air passage hydraulic diameter | $D_h$=6.68 mm |

Table 8 Parameters for heat exchanger

The mass flow rate of water required is calculated using the heat balance equation. Therefore, the heat exchanger should be large enough to transfer heat of the following amount:

$$\dot{m}_c = \frac{Q}{C_{P,c} \cdot \Delta T_c} = \frac{20000}{4209 \times 10} = 0.475\, kg / \sec \qquad (6\text{-}21)$$

Likewise, the air mass flow rate provided to the heat exchanger and the air temperature rise through the heat exchanger can be calculated with the following equations:

$$\dot{m}_{air} = \rho_{air} \cdot A_{fontr} \cdot v_{air} = 1.1614 \times 0.3 \times 2.78 = 0.96(kg\,s^{-1}) \quad (6\text{- }22)$$

$$\Delta T_{air} = T_{air,out} - T_{air,in} = \frac{\dot{Q}}{\dot{m}_{air} \cdot Cp_{air}} = \frac{20000}{0.96 \times 1007} = 20.7K \quad (6\text{- }23)$$

Thus, the heat exchanger outlet air temperature (K) is equal to 320.7.

The heat exchanger has 100 cross-tubes, a 0.8 $m^2$ frontal area, and a 0.2 m thickness. It can be assumed that mass flow is laminar because the Reynolds Number is less than 2300. Therefore, the Nusselt number for a tube with constant heat flux is a constant, 4.36.

$$Nu = \frac{h_{cool} \cdot D_h}{k} = 4.36 \quad (6\text{- }24)$$

where $h_{cool}$ is convective heat coefficient of the coolant (W $m^{-2}K^{-1}$), $D_h$ is hydraulic diameter (m), and $k$ is the conduction heat coefficient (W $m^{-2}K^{-1}$). Hence,

$$h_c = \frac{k \cdot 4.36}{D_h} = \frac{0.677 \times 4.36}{0.0164} = 179.98(Wm^{-2}K^{-1}) \quad (6\text{- }25)$$

Under the assumption that the thickness of the fin is negligible, it can be written as:

$$\frac{A_{cool}}{A_{air}} \approx \frac{D_i}{D_o}\left(1 - \frac{A_{fin}}{A_{air}}\right) = \frac{13.8}{16.4}(1 - 0.83) = 0.1430 \quad (6\text{- }26)$$

where $A_{air}$ is total surface area of the heat exchanger including the fins ($m^2$), $A_{fin}$ is total surface area of just all of the fins ($m^2$), and $A_{cool}$ is total surface area of the inside of the tubes ($m^2$). Calculating wall conduction resistance by:

$$A_{air} \cdot R_w = \frac{\ln \frac{D_o}{D_i}}{\frac{2\pi \cdot L \cdot k}{A_{air}}} = \frac{D_i \cdot \ln \frac{D_o}{D_i}}{\frac{2\pi \cdot A_{cool}}{A_{air}}} = \frac{D_i}{A_{air}} \cdot \ln \frac{D_o}{D_i} \tag{6- 27}$$

$$A_{air} \cdot R_w = \frac{0.0138}{2 \times 237} \ln \frac{16.4}{13.8} = 5.025 \times 10^{-6} \, (m^2 K W^{-1})$$

The mass flux, G, is evaluated using the equation below:

$$G = \frac{\dot{m}_{air}}{A_{free}} = \frac{\rho_{air} \cdot V_{air} \cdot A_{front}}{A_{free}} = \frac{1.1614 \times 2.78 \times A_{front}}{A_{free}} = \frac{3.2287}{A_{free} / A_{front}} = 1.4544 \tag{6- 28}$$

Hence, the Reynolds number is equal to

$$\mathrm{Re} = \frac{G \cdot D_h}{\mu} = \frac{1.4544 \times 0.00668}{184.6 \times 10^{-7}} = 525.972 \tag{6- 29}$$

And from the heat exchanger characteristics [24],

$$j_H \cong 0.0145 \tag{6- 30}$$

Hence,

$$h_{air} = 0.0145 \frac{G \cdot Cp_{air}}{\mathrm{Pr}^{2/3}} = 0.0145 \frac{1.4544 \times 1007}{0.707^{2/3}} = 26.759 \, (W \ m^{-2} K^{-1}) \tag{6- 31}$$

To obtain fin efficiency from the efficiency of annular fins of rectangular profile [24],

$$r_{2c} = r_2 + \frac{t}{2} = 0.0285 + \frac{0.000254}{2} = 0.028627m$$
$$L_c = L + \frac{t}{2} = (0.0285 - 0.0164) + \frac{0.000254}{2} = 0.012227m$$
$$A_p = L_c t = 3.105 \times 10^{-6} m^2$$
$$\frac{r_{2c}}{r_1} = \frac{28.5}{16.4} = 1.74 \tag{6- 32}$$

And

$$L_c^{3/2}\left(\frac{h_h}{kA_p}\right)^{1/2} = 0.012227^{3/2}\left(\frac{51.33}{0.0263\times 3.105\times 10^{-6}}\right)^{1/2} = 0.357 \tag{6- 33}$$

From the efficiency of annular fins of rectangular profile [24], it follows that $\eta_f \approx$ 0.89. Hence, overall efficiency becomes:

$$\eta_{o,c} = 1 - \frac{A_f}{A}\left(1-\eta_f\right) = 1 - 0.83\left(1-0.89\right) = 0.91 \tag{6- 34}$$

Then, overall heat coefficient is obtatained [18]:

$$\begin{aligned}\frac{1}{U_{air}} &= \frac{1}{h_{cool}\left(\frac{A_{cool}}{A_{air}}\right)} + A_{cool}R_W + \frac{1}{\eta_O h_{air}} \\ &= \frac{1}{178.98\left(0.0978\right)^{-1}} + 1.912\times 10^{-5} + \frac{1}{0.91\times 51.33} = 0.02197\,(m^2 K W^{-1})\end{aligned} \tag{6- 35}$$

Thus,

$$U_c = 45.5\,(W m^{-2} K^{-1}) \tag{6- 36}$$

To calculate the correction factor F, the following equation is used.

$$\begin{aligned}R &= \frac{T_i - T_o}{t_o - t_i} = \frac{T_{c,i} - T_{c,o}}{T_{h,o} - T_{h,i}} = \frac{300-320.7}{355-365} = 2.07 \\ P &= \frac{t_o - t_i}{T_i - t_i} = \frac{T_{h,o} - T_{h,i}}{T_{c,i} - T_{h,i}} = \frac{355-365}{300-365} = 0.154\end{aligned} \tag{6- 37}$$

Hence, from shell and tube correction factor table [24],

$$F \approx 1 \tag{6- 38}$$

Using the Log Mean Temperature Difference (LMTD) methods,

$$\begin{aligned}\Delta T_{lm} &= \frac{(T_{h,i} - T_{c,o}) - (T_{h,o} - T_{c,i})}{\ln[(T_{h,i} - T_{c,o})/(T_{h,o} - T_{c,i})]} \\ &= \frac{(365-320.7) - (355-300)}{\ln[(365-320.7)/(355-300)]} = 49.46(K)\end{aligned} \tag{6- 39}$$

Therefore, the required length of the heat exchanger is as follows [18]:

$$L = \frac{q}{UN\pi DF\Delta T_{lm,CF}} = \frac{20000}{45.5\times 100\times \pi \times 0.0164\times 49.46} = 1.73(m) \qquad (6\text{-}40)$$

As shown before, the temperature difference is a typical design factor which is a proportional inverse to the coolant flow rate required.

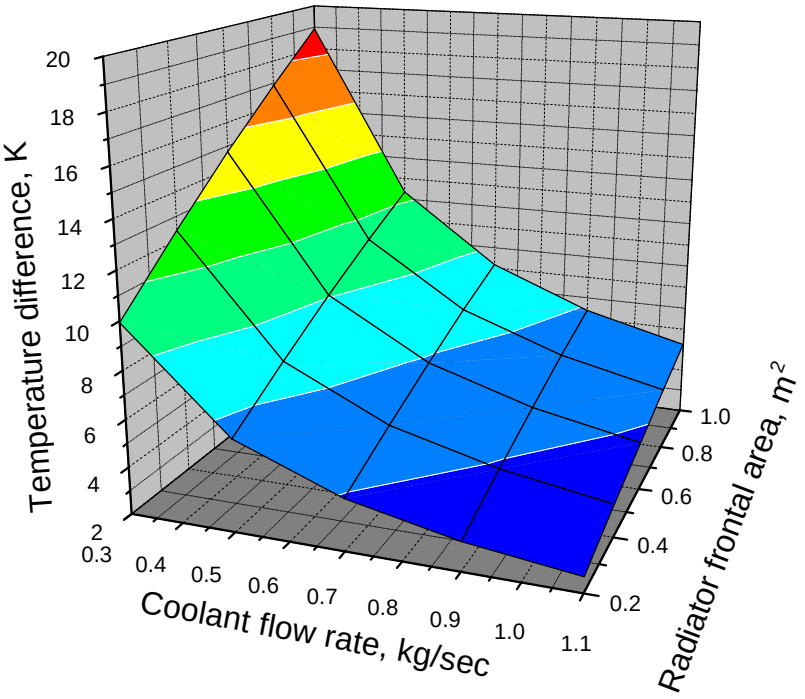


Figure 44 The relationship between coolant temperature difference, flow rate and radiator frontal area

In other words, if a small temperature difference which makes cell temperature distribution even is required, the coolant flow rate should be large enough to reject the heat generated from the stack as it causes more parasitic loss in the balance of plant. However, at the same temperature difference, the coolant flow rate can be minimized by increasing the radiator frontal area. The relationship between those parameters is shown in the figure below. Moreover, an increase in frontal area with the same coolant flow rate allows for a larger temperature difference, i.e. lower coolant outlet temperature, while it maintains the same desired operating temperature and decreases parasitic loss. Therefore, considering not only parasitic loss, but also the physical size and shape of the heat exchanger is pivotal for developing right thermal circuit.

# 7 100-CELL PEM FUEL CELL SYSTEM

PEM fuel cell system is made using the 100-cell stack, air supply system and thermal circuit system. After 100-cell stack model is developed, air supply system and thermal circuit system is connected to estimate power more accurately.

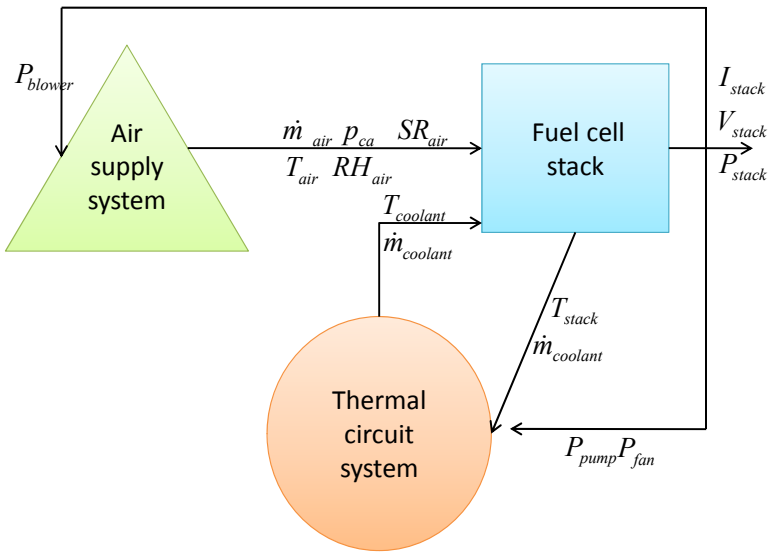


Figure 45 Schematic diagram of PEM fuel cell system

Auxiliary components consume the power from the stack for operation of a blower, coolant pump, radiator fan. The successful operation of B.O.P is important for safe and appropriate operation of the stack system.

Static and dynamic performance of the stack with a single and multi cells (SSMC) is compared with a model for a stack that is given by simply multiplying a single cell with the cell numbers, called as a stack with a single cell (SSC).

### 7.1.1 STATIC BEHAVIOR

The model for the stack proposed was used to analyze static and dynamic performance. The results of the simulation were compared with the case when the stack was simply constructed by a multiplication of the cell numbers with a single cell.

I-V characteristics of the each cell in the SSMC and SSC are shown in Figure 46. There are temperature difference and effect within the stack and they cause voltage difference between cells.

When the current density gets lower, no noticeable differences in the voltages of the stack were shown, but the differences in the voltages increased when the current density became higher because the more water removal and heat generation rate and larger temperature gradient occurs at the high current density. As a result, the maximum power of the SSMC became larger than that of the SSC. The voltage difference between each stack is about 8V at most.

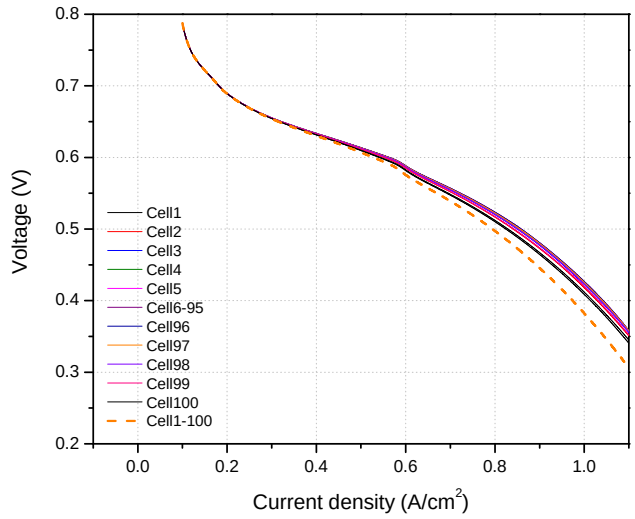


Figure 46 I-V polarization characteristic curve of each cell

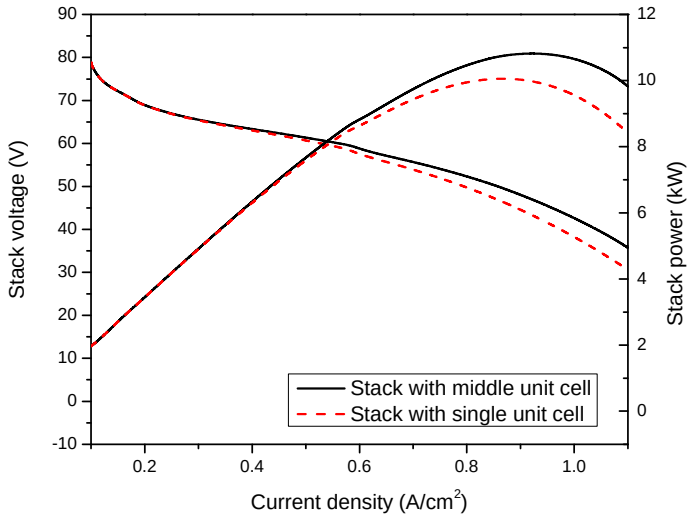


Figure 47 Stack power and voltage

### 7.1.2 DYNAMIC BEHAVIOR

#### 7.1.2.1 START-UP MODE

Temperature behavior is investigated in membranes of individual cells during a startup behavior for the 100-cell stack, as shown in Figure 48, where a ramp current density was applied. For analysis of dynamic behaviors of the 100-cell stack, the ambient temperature is assumed to be 30K and the cooling of the stack is controlled by turning the coolant pump on and off, dependent upon a value of the outlet temperature of the coolant that was set at 70K. A ramp current with a rate of 0.01 (A $cm^{-2}$ $s^{-1}$) is applied during a start-up, while a multi-step current is applied for transient analysis.

When the current is applied, then the heat inside the stack is generated and temperature of the membranes begins to increase, as shown in Figure 48. Because of high heat transfer rate of the end cells from the temperature difference with ambient air, temperature of the cells located in the middle of the stack was higher than that of the end cells. The temperature difference between the SSMC and SSC amounts to around 50K during the start-up that took 100 seconds. In addition, the temperature rise of the individual cells varies from cell to cell. However, temperature rises in the SSC relatively slower than that of the SSMC due to the higher heat transfer rate. The SSC is assumed that each cell has a same amount of heat transfer rate and actually single unit cell faces the ambient temperature which make large temperature difference which cause higher het transfer rate between unit cell and ambient.

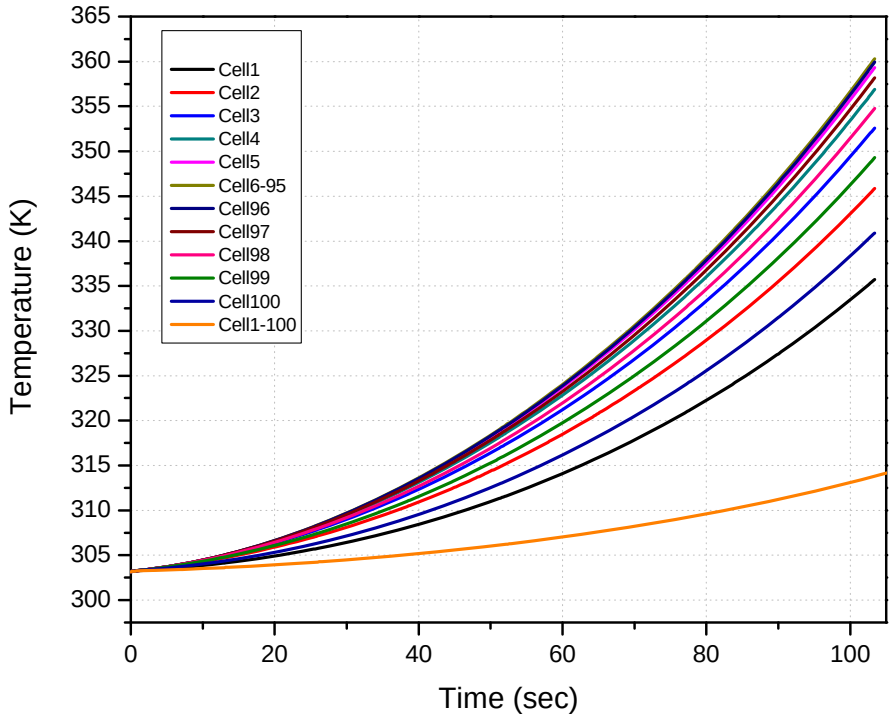


Figure 48 Temperature changes during the start-up

During the start-up, temperature gradient increase with the increase in current density which causes more heat inside the stack developed by connecting the middle unit cell. The interaction of temperature effect between each cell is considered and it makes larger temperature gradient at the end cell than the stack made by the single unit cell. The SSMC has higher temperature than the SSC because it is connected with cell which is hotter than ambient and it causes much less heat transfer and higher temperature at the each cell. The temperature difference between the stack with middle unit cell and the stack with single cell is about 8K after 40 sec during the start-up.

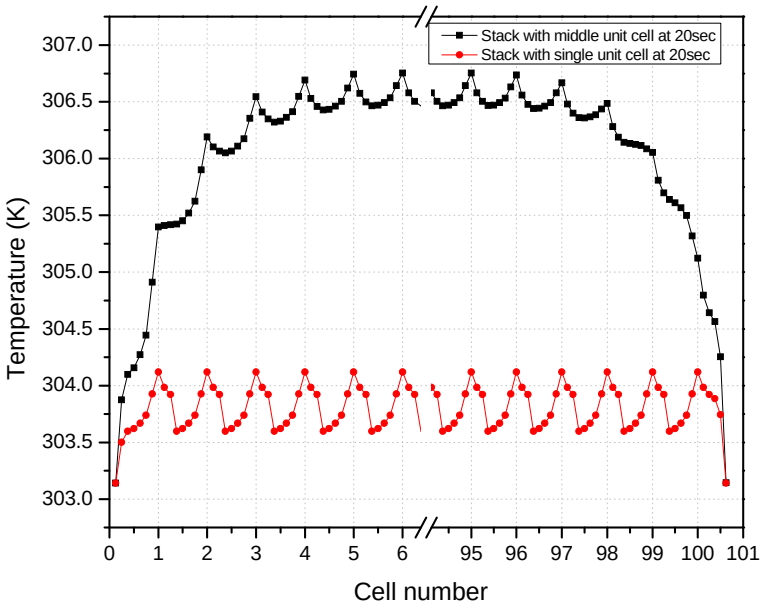


Figure 49 Comparison of temperature distribution during the start-up

As current density increases, ohmic overpotential has a much greater affect by the membrane resistance and heat from the catalyst layer during the higher rate of chemical reaction. Moreover, the deviation not only in the each cell between catalyst layer and coolant channel, but also in the stack between end cell and middle cells becomes more significant due to the larger heat generation in a short time during the start-up. The temperature difference between the end cell and middle cell is about 30K after 100sec during the start-up.

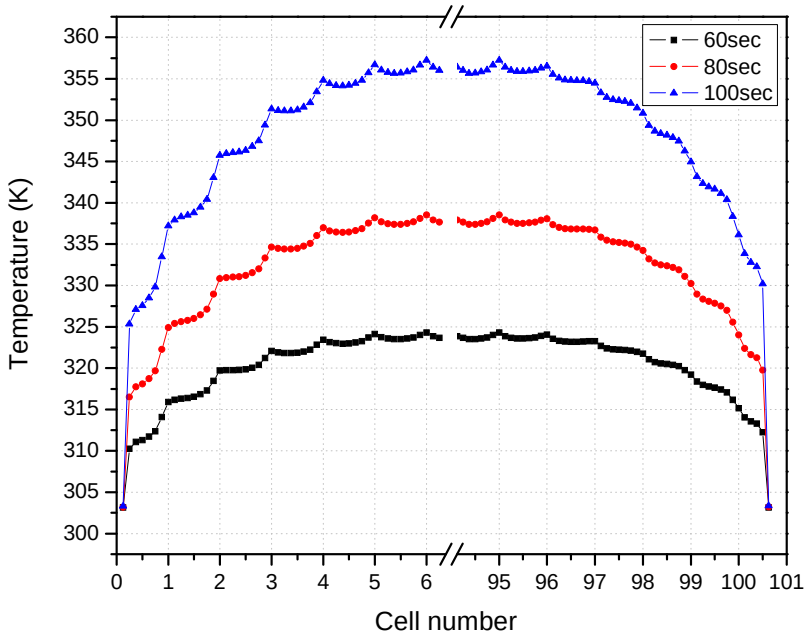


Figure 50 Temperature distribution during the start-up

Figure 51 shows a voltage distribution in the SSMC. The middle cells in SSMC have a higher voltage than end cells while each cell of the SSC has a same output voltage. When the temperature was low, the difference between the SSMC and SSC was smaller at the beginning and became larger as temperature rises. The middle cells with higher temperature can remove water easily by evaporation and accelerate chemical reaction with lower activation energy (Eq.3-6). Therefore, they have less activation over potential, ohmic overpotential, concentration overpotential and larger proton conductivity in the membrane. In the experiment, each cell has a different cell voltage [20]. In contrast, the stack with single cell has a limitation in the reflection of temperature interaction within

multi cell stack and does not explain voltage increases due to the temperature effect in the real stack.

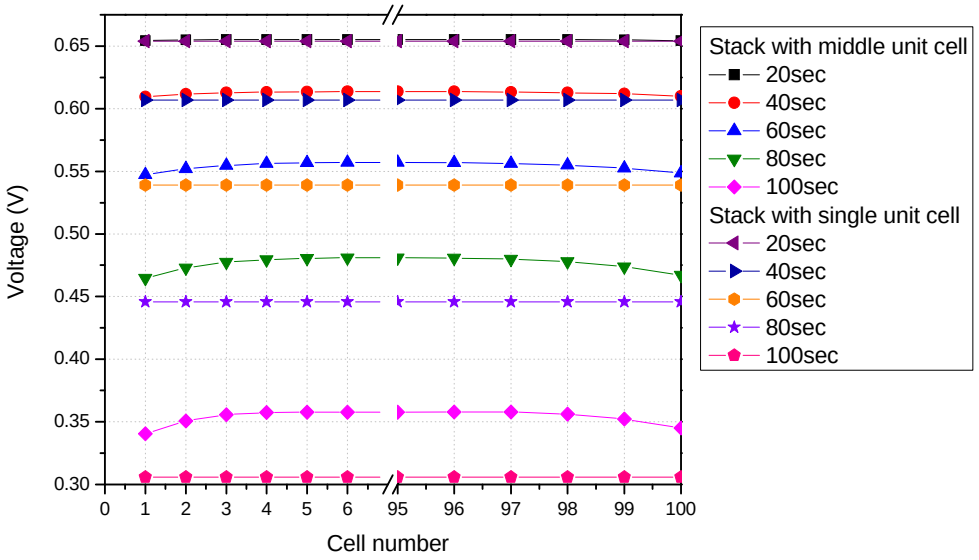


Figure 51 Voltage changes during the start-up

### 7.1.2.2 TRANSIENT BEHAVIOR

For transient analysis, responses of oxygen, vapor concentrations, water content of membranes in the middle cells and voltages are calculated as a multi-step current applied to the stack as shown in the Figure 52.

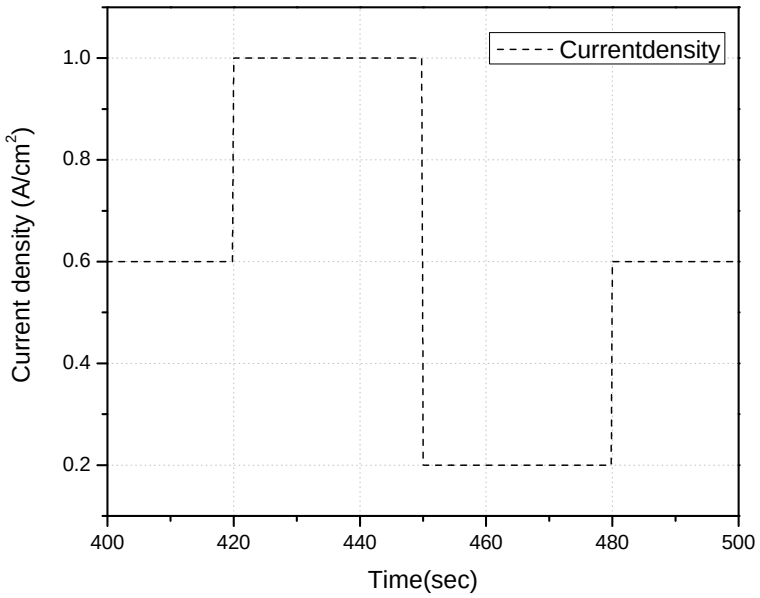


Figure 52 Current density applied

When the current density increases, temperature of the stack is increased as shown in Figure 53 due to the higher heat generation at the catalyst layer. The SSMC is connected by multi cell facing each other at the both of end side while SSC is composed of single unit cell which is in contact with ambient air and has a larger heat transfer rate to the endplate. Therefore, heat generated in SSC is transferred easily and the temperature effect causes recovery time of the temperature faster than that in the SSMC with a given coolant flow rate when the current load suddenly increases.

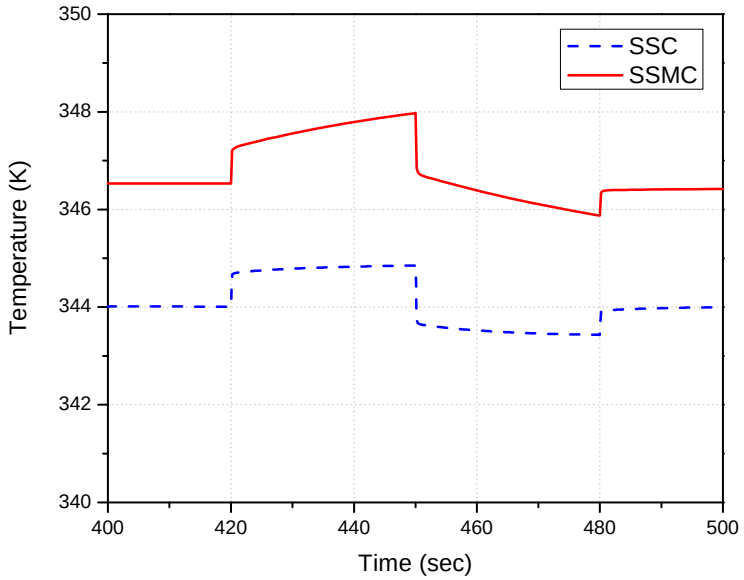


Figure 53 Transient responses of temperature in the middle cells

The results below showed different oxygen concentrations caused by the difference in the operating temperature, as shown in Figure 54. The oxygen in the multi-cell tends to be starving by the time an abrupt change of current occurs, which was recovered by a controller that helps replenish the oxygen. The stack with middle unit cell has a high temperature and it causes less oxygen concentration than the stack with single cell in a given pressure and control volume. Furthermore, it causes smaller overshoot of oxygen concentration in the SSMC than SSC.

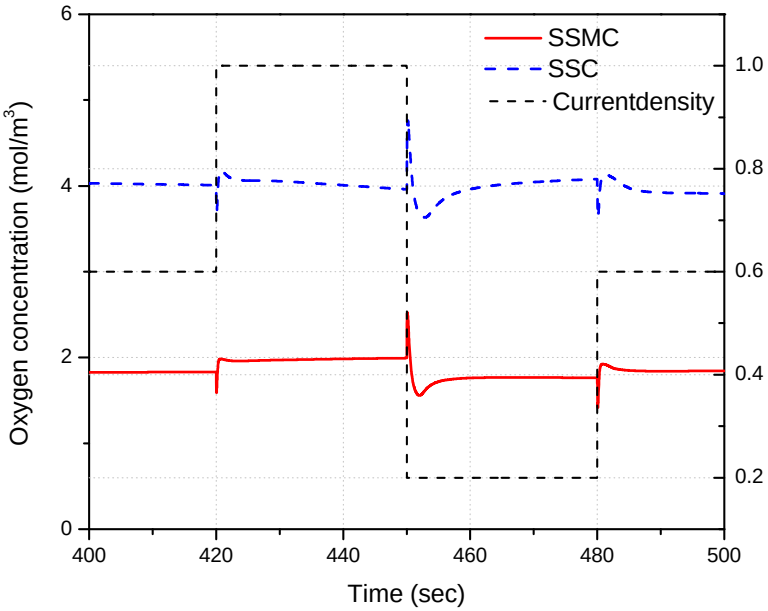


Figure 54 Dynamic response of oxygen concentration to the step input

In the stack with middle unit cell, its vapor concentration increases with temperature rise because it is assumed that air is humidified with a specific amount of ratio and its saturation pressure is increased with increase in the stack temperature. Therefore, a rise in saturation pressure makes vapor partial pressure and concentration increase.

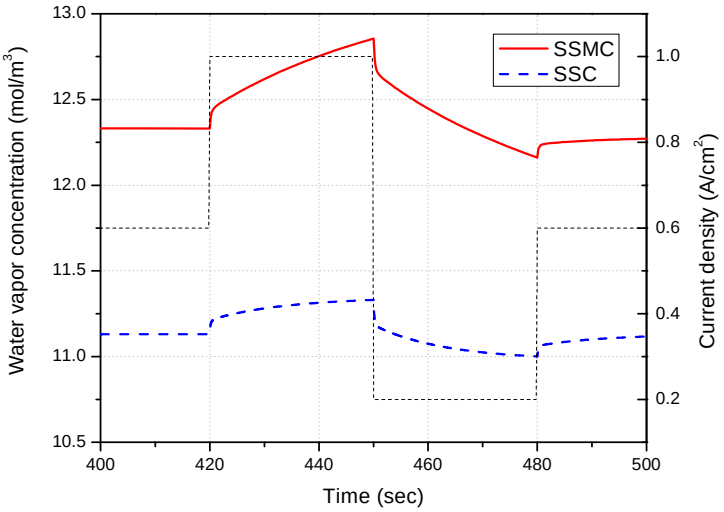


Figure 55 Dynamic response of vapor concentration to the step input

Water contents in the membranes and temperature behaviors are shown in Figure 56 . When the current density increased, the liquid water saturation is increased due to the accelerated chemical reaction. However, there is no significant difference between SSMC and SSC. When the current density is increased, the water contents of membrane suddenly decrease because of the higher rate of water uptake from the anode to the cathode side. The elevated temperature affected the recovery time of the water contents. Increasing temperature causes not only higher diffusivity (Eq.3-20) but also higher saturation pressure which makes less water activity (Eq.3-23) and water contents (Eq.3-24). It causes water transport from the membrane to the cathode much harder by electro osmotic force (Eq.3-17). Consequently, decrease in water activity makes less water transportation out of the membrane and recovery speed of the membrane water contents at the membrane in the SSMC slightly faster than that in the SSC. When the current

increases, temperature in the middle cells rises and the maximum difference of the temperature was about 2.5K, as shown in the Figure 53.

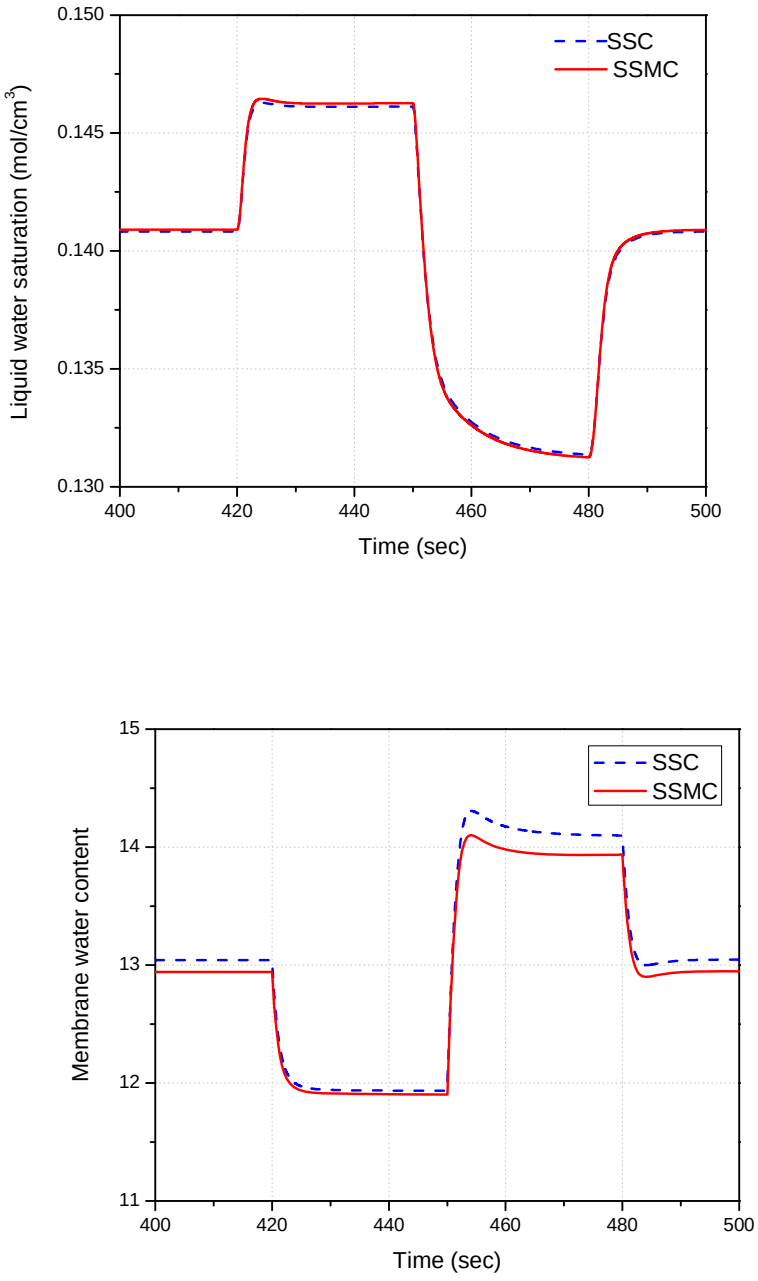


Figure 56 Transient response of liquid water saturation and water content of membranes

in the middle cells

The ohmic over-potential and the voltage of the stack are shown in Figure 57 and Figure 58. The activation overpotential and ohmic overpotential of the membranes decrease when the temperature rises (Eq. 3-6 and 8) due to the lower activation energy and ohmic resistance at the membrane. As a result, the voltage of the SSC that is composed of one single cell without temperature effect stack was smaller than that of SSMC.

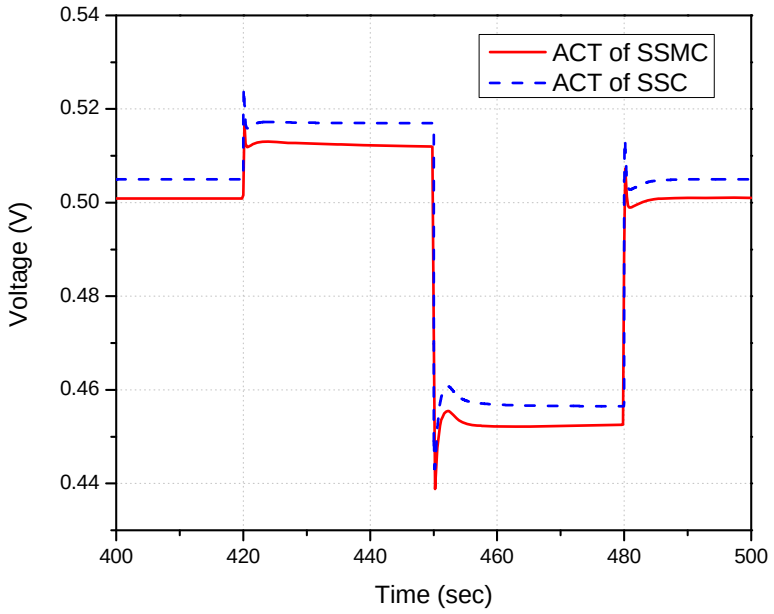


( a ) Activation over potential

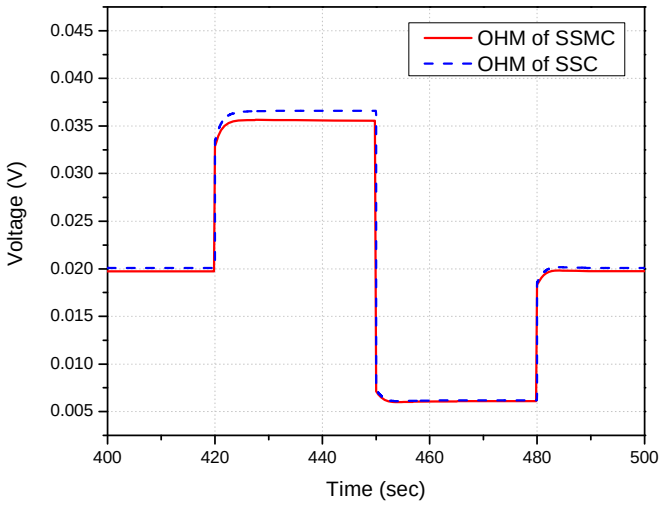


( b ) Ohmic over potential

Figure 57 Transient responses of activation and ohmic overpotential in the middle cells

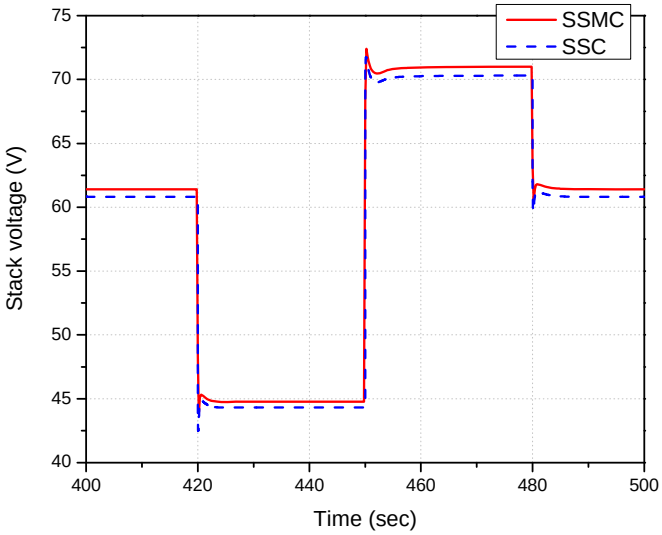


Figure 58 Transient responses of PEM fuel cell stack voltage

### 7.1.3 DYNAMIC BEHAVIOR DURING OPERATION MODE

After total PEM fuel cell test station is built, the model was simulated under the operation mode to verify that the B.O.P system meets the needs for performance. Total net power should satisfy specification which needs about 8kW during normal walking mode with hydraulic device in the robot. The load profile and corresponding stack voltage is as follows. The current load is determined considering operating voltage and current, which is around 0.6 V where efficiency is about 50% and maximum current load is limited at 1.0A where power output start decreasing and efficiency becomes less than 40%. As seen in Figure 60, the system generates power output more than 8kW and about 11kW at most.

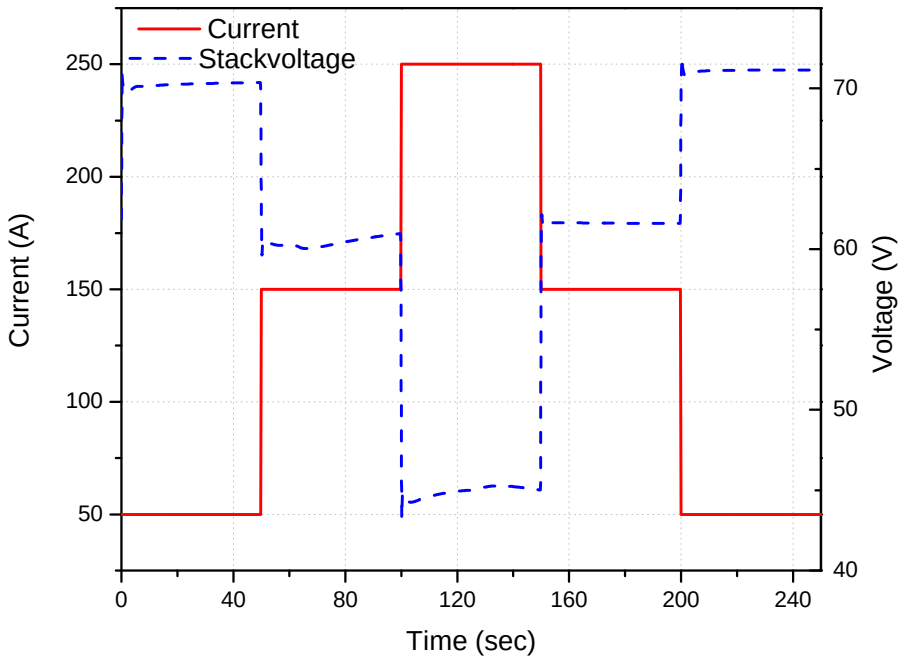


Figure 59 Current load under the operation mode

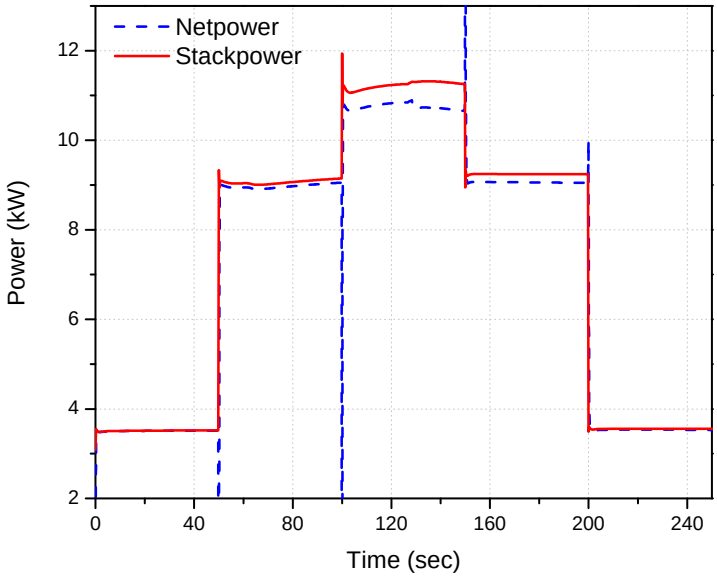


Figure 60 Net power and stack power during the operation mode

As seen in Figure 60, there is region where power decreases suddenly because increase in current load makes blower motor rotate faster to maintain desired stoichiometric air flow ratio at a steady rate. Therefore, blower consumes more power to be accelerated with rotational inertia of the blower and motor. Moreover, sudden increase in current load causes stack starvation by the time when an abrupt change of current occurs as shown in Figure 54 and the shortage causes a sudden decrease in the net power as well. Consequently, appropriate margin power and stoichiometric ratio of the oxygen should be considered for successful operation.

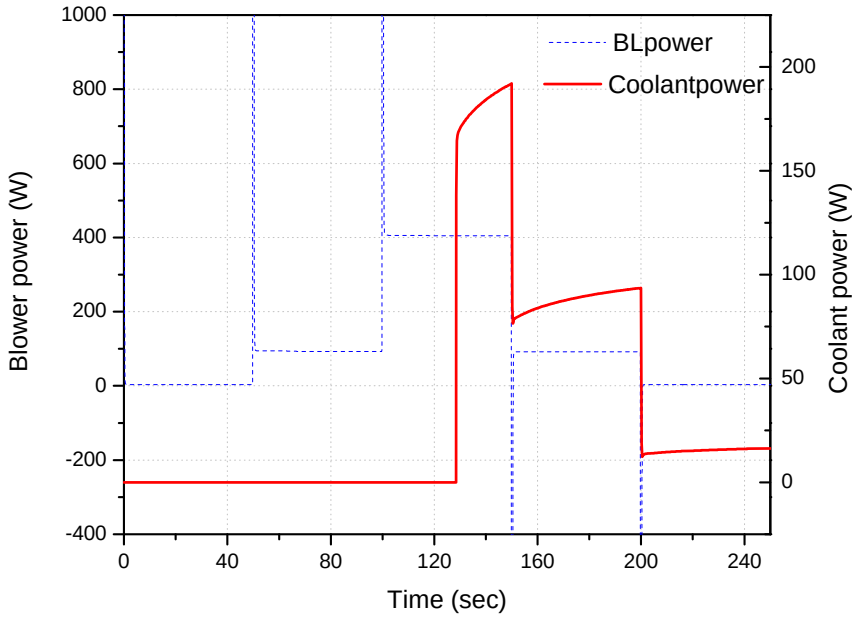


Figure 61 Parasitic power of air supply system and thermal circuit during operation

The stack temperature is controlled using coolant system including coolant pump and radiator fan which start operating when the stack temperature is over the desired temperature to minimize parasitic loss. The coolant power suddenly increases at 130 sec when the stack temperature is over the desired temperature, 343 K. However, its parasitic power gradually decreases as temperature decreases and is close to desired temperature because coolant pump is operated by the magnitude of the temperature difference between stack and desired temperature. Temperature of each cell in the stack increases with current loads until it reaches desired temperature as shown in Figure 62. Each slope for increase in temperature is dependent upon the heat generation rate determined by magnitude of the current load.

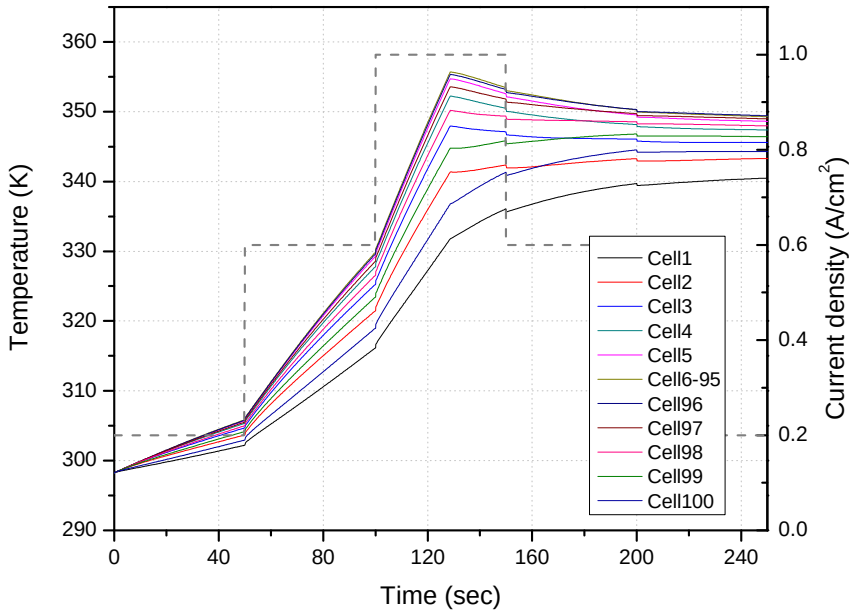


Figure 62 Temperature changes during the operation

### 7.1.4 DESIGN PROGRESS

Through using different kinds of material and considering the different operating condition and geometry, final design of the 100-cell PEM fuel cell system achieved about 0.44 (W cm$^{-2}$) power density, 32% reduction in weight and 29% reduction in volume for use in the quadruped robot as shown in the Figure 63.

| | **1st design** | **2nd design** | **3rd design** |
|---|---|---|---|
| Materials | Polymer, copper and graphite | G-10 Garolite, stainless steel and AXF-5Q-PYC graphite and Tm graphite | G-10 Garolite, stainless steel, AXF-5Q-PYC graphite, Tm graphite , another graphite and different geometry |
| Active area (cm$^2$) | 250 | 250 | 250 |

| | | | |
|---|---|---|---|
| Coolant and gas channel contact percentage (%) | Normal | Normal | Normal |
| Stack weight (kg) | 28.32 | 24.01 | 19.4 |
| Dimension (W x H x L) (cm) | 22 x 25 x 77 | 22 x 25 x 66 | 22 x 25 x 53.93 |

Table 9 Design progress of the PEM fuel cell system

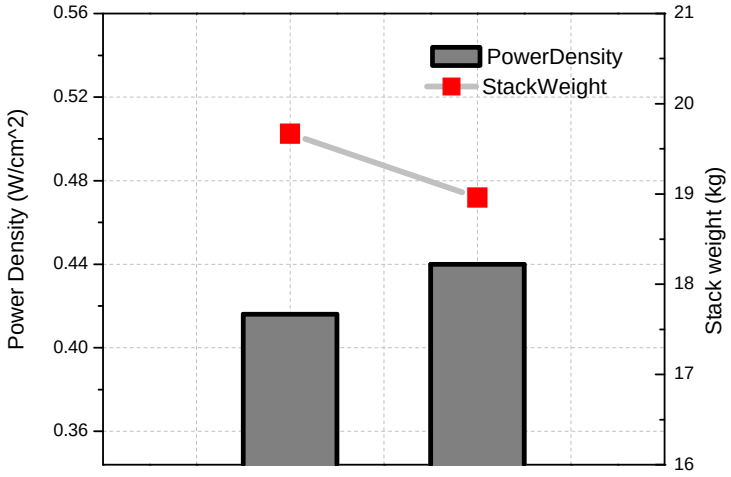


Figure 63 Schematic diagram and design progress of the PEM fuel cell system

# 8 CONCLUSIONS

The dynamic model for a 100-cell stack is developed considering temperature and two-phase effects in the GDL in which performance was compared with experimental data. Simulations were performed to analyze dynamic performance of the stack. First, I-V characteristics of the two-cell stack, as well as the individual cells, were compared under different operating conditions and geometry. The voltage differences between cell 1 and cell 2 were caused by temperature gradients in each layer and subsequently the ohmic overpotentials. However, the liquid water did not significantly affect the limit of the current density because the gradient of water concentration, the pressure and temperature drop along the flow channel have not been fully considered in the modeling.

Second, the effects of two-phase water on the performance were studied with different geometry to analyze the effects of the key design parameters and operating conditions including the cell voltages, three kinds of overpotential, water content, oxygen concentration and temperature, subsequently the stack is optimized based on the results for the two-cell stack. Voltage differences between a single-phase and two-phase model were predominantly affected by the activation overpotentials caused by changes in oxygen concentration. With a more porous GDL and a thinner GDL and membrane, the cell-voltages increased. However, the effects were not significant at a low current density. With a higher stoichiometric flow ratio, air temperature, and relative humidity, the cell-voltages also increased.

Furthermore, each B.O.P components is considered in the modeling to estimate more realistic net power from the PEM fuel cell system. Finally, the stack model which is appropriate for a high number of a cell was proposed and constructed based on the 20-cell model analysis and used to analyze static and dynamic characteristics at start-up and at varying loads. The 100-cell model takes into account three important properties of a PEM fuel cell that includes electrical behavior of the terminal, temperature in the cells and characteristics of the two-phase flow. Comparisons between a stack with a single and multi cells (SSMC) and a stack with single cell (SSC) show no significant terminal behavior, while temperature distribution, water concentrations, and oxygen concentration through the cells of SSMC, to name a few, are completely different from that of SSC. Design of a stack, components of balance-of-plant, and the associated controls should be based on the behavior of the complete stack.

Future work will include three phase effect with ice under the subfreezing temperature. Start-up time of the PEM fuel cell stack in mobile applications is of great importance for commercialization. In particular, when operation of a stack stops and the ambient temperature drops under sub-freezing temperature, water residing in the various layers of the stack forms ice. As a result, the start-up time at the following start is increased by latent hat which absorbs the heat produced, blocking the flow of the reactants in the pores and dropping proton conductivity in the membranes. Thus, the start-up time directly relates the amount of residing ice, the produced heat that causes the ice to thaw, flow characteristic in the porous media determined by ratio of the ice, liquid water and water vapor, and proton transport affected by water content in the membrane.

These complex phenomena should be explored to ensure commercialization of the fuel cell.

## REFERENCES


[1] M. R. von Spakovsky and B. Olsommer, Fuel cell systems and system modeling and analysis perspectives for fuel cell development, Energy Conversion and Management 43 (2002) 1249-1257.

[2] J. Larimie and A. Dicks, Fuel Cell Systems Explained, Wiley, 2003.

[3] J. Ahn, Design and analysis of air and coolant control, Auburn University, 2007

[4] H. Meng and C. Y. Wang, Model of two-phase flow and flooding dynamics in polymer electrolyte fuel cells, J. Electrochem. Soc. 152 (2005) 1733-1741.

[5] J. C. Amphlett, R. M. Baumert, R. F. Mann, B. A. Peppley and P. R. Roberge, Performance modeling of the Ballard Mark Ⅳ solid polymer electrolyte fuel cell. Ⅰ. Mechanistic model development, J. Electrochem. Soc. 142 (1995) 1-8.

[6] Y. Shan and S. Y. Choe, A high dynamic PEM fuel cell model with temperature effects, J. Power Sources 145, 1 (2005) 30-39.

[7] J. C. Amphlett, R. F. Mann, B. A. Peppley, P. R. Roberge and A. Rodrigues, J. Power Sources 61 (1996) 183–188.

[8] T. E. Springer, T. A. Zawodzinski and S. Gottesfeld, Polymer electrolyte fuel cell model, J. Electrochem. Soc. 138 (1991) 2334-2341.

[9] T. V. Nguyen and R. E. White, A water and heat management model for proton-exchange-membrane fuel cells, J. Electrochem. Soc. 140 (1993) 2178-2186

[10] J. M. Correa, An electrochemical-based fuel-cell model suitable for electrical engineering automation approach, IEEE 515 (2004) 1103-1113.

[11] Y. Shan and S.Y. Choe, A segmented model for studying water transport in a PEMFC, J. Power Sources 145 (2005) 30–39.

[12] M. Khandelwal, S.H. Lee and M.M. Mench, One-dimensional thermal model of cold-start in a polymer electrolyte fuel cell stack, J. Power Sources 172 (2007) 816–830.

[13] J. H. Nam and M. Kaviany, Effective diffusivity and water-saturation distribution in single- and two- layer PEMFC diffusion medium, International Journal of Heat and Mass Transfer, 46 (2003) 4595-4611.

[14] J. T. Pukrushpan, A. G. Stefanopoulou and H. Peng, Modeling and control for PEM fuel cell stack system, Proceedings of the American Control Conference, Anchorage, Alaska, May 8-10, 2002.

[15] Phoenix Design & Technologies, The PDAT Turbomix. http://www.padtinc.com/sales/fuelcell/turbomix/, July 2009

[16] P. Rodtz, G. Paganelli and L. Guzzella, Optimizing air supply control of a PEM fuel cell system, Proceeding of the American Control Conference, Denver, CO, June, pp. 2043-9, 2003.

[17] S. Gurski, Cold Start Effects on Performance and Efficiency for Vehicle Fuel Cell System, Master of Science Thesis, Virginia Polytechnic Institute and State University, 2002.

[18] A. Rowe and X. Li, Mathematical modeling of proton exchange membrane fuel cells. J. Power Sources 102, 1-2 (1993) 82-96.

[19] L. Wang, A. Husar, T. Zhou and H. Liu, A parametric study of PEM fuel cell performances, J. Hydrogen Energy 28 (2003) 1263-1272.

[20] P. Rodatz, F. Buchi, C. Onder and L. Guzzella, Operational aspects of a large PEFC stack under practical conditions, J. Power Sources 128 (2004) 208-217.

[21] F. M. White, Fluid Mechanics, second ed., McGraw Hill, New York, 1986.

[22] F. P. Bleier, Fan handbook-selection, application and design, McGraw-Hill, 1997

[23] H. J. Park, Fluid Machinery Engineering, Il-jin, 2003.

[24] F. P. Incropera and D. P. Dewitt, Heat and mass transfer, Wiley, 2003.

[25] H. Ju, H. Meng and C. Y. Wang, A single phase non isothermal model for PEM fuel cells. International Journal of Heat and Mass Transfer, 48, 7 (2005) 1303-1315.

[26] D. G. Kroger, Radiator Characterization and Optimization, SAE paper 840380, 1984.

[27] S. K. Park and S. Y. Choe, Dynamic modeling and analysis of 20-cell PEM fuel cell stack considering temperature and two-phase effects, J. Power Sources 179 (2008) 660-672.

[28] Q. Yan, H. Toghiani and H. Causey, Steady state and dynamic performance of proton exchange membrane fuel cell (PEMFCs) under various operating conditions and load changes, J. Power Sources 161 (2006) 492-502.